

On the edge of a cloud



Thijs Heus

ON THE
EDGE
OF A
CLOUD

ON THE EDGE OF A CLOUD

Proefschrift

ter verkrijging van de graad van doctor
aan de Technische Universiteit Delft,
op gezag van de Rector Magnificus prof. dr. ir. J. T. Fokkema,
voorzitter van het College voor Promoties,
in het openbaar te verdedigen op dinsdag 9 december 2008 om 15.00 uur

door

Thijs HEUS

doctorandus in de experimentele natuurkunde
en in de meteorologie en fysische oceanografie
geboren te Utrecht

Dit proefschrift is goedgekeurd door de promotor:
Prof. dr. ir. H. E. A. van den Akker

en de copromotor:
Dr. H. J. J. Jonker

Samenstelling promotiecommissie:

Rector Magnificus	Voorzitter
Prof. dr. ir. H. E. A. van den Akker	Technische Universiteit Delft, promotor
Dr. H. J. J. Jonker	Technische Universiteit Delft, copromotor
Prof. dr. P. H. Austin	University of British Columbia
Prof. dr. A. A. M. Holtslag	Wageningen Universiteit
Prof. dr. A. P. Siebesma	Technische Universiteit Delft
Prof. dr. B. Stevens	Max-Planck-Institut für Meteorologie
Prof. dr. P. P. Sullivan	National Center for Atmospheric Research



Technische Universiteit Delft



Dit werk is financieel gesteund door de Nederlandse Organisatie voor Wetenschappelijk Onderzoek (NWO). Voor het gebruik van supercomputer-faciliteiten bij dit onderzoek is subsidie verleend door de Stichting Nationale Computer Faciliteiten (NCF).

Copyright © 2008 hoofdstuk 3 en 5, en figuur 1.2 American Meteorological Society
Copyright © 2008 hoofdstuk 4 Royal Meteorological Society
Copyright © 2008 voor het overige Thijs Heus

Uitgegeven door Grafisch Bedrijf Ponsen & Looijen BV
ISBN: 978-90-6464-301-9

PROPOSITIONS

Belonging to the PhD thesis *On the edge of a cloud* by Thijs Heus

- 1 Parameterizing cumulus clouds without taking the role of the subsiding shell into account, may only be successful due to a prefactor or with luck.
- 2 The latent heat release of condensation, in combination with the dry, warm environment turns clouds into one of the clearest examples in nature of the unsteady puff convection as described by Hunt et al. (*J. Fluid Mech.*, 2003).
- 3 The only spectral gap existing in the atmospheric sciences is between textbooks and the scientific state-of-the-art.
- 4 The *h*-index would be more valuable if it were calculated over papers published in the last 10 years only.
- 5 The average scientific age of a supervisor, roughly 20 years, sets a time scale for rediscovering scientific results from earlier days.
- 6 Clouds and washing machines show that virtual potential temperature and socks are non-conserved quantities.
- 7 The beauty of scientific studies cannot be explained but must be experienced.
- 8 Both climate research and evolution theory grew up in public, resulting in a persistent belief in their teething troubles.
- 9 Universities would find more and better PhD candidates if they would advertise the creativity and the diversity of methods involved in science, rather than focus on the limited scope of a PhD project.
- 10 Referenda imply a disqualification of politicians for their job, and justify salaries in the public sector that are higher than the salary of the prime minister.
- 11 The position of head of the multi-scale physics department at TU Delft is an underpaid job.

These propositions are considered opposable and defensible and as such have been approved by the supervisor, prof. dr. ir. H. E. A. Van den Akker.

STELLINGEN

Behorende bij het proefschrift *Over de rand van een wolk* door Thijs Heus

- 1 Zonder rekening te houden met de neergaande ring kan een model van cumuluswolken alleen maar slagen dankzij een voorfactor of dankzij mazzel.
- 2 De latente warmte die vrijkomt bij condensatie, in combinatie met de warme, droge omgeving, zorgt ervoor dat wolken één van de duidelijkste voorbeelden zijn van *unstable puff convection* zoals beschreven door Hunt et al. (*J. Fluid Mech.*, 2003).
- 3 Het enige spectrale gat in de atmosferische wetenschappen ligt tussen studieboeken en het front van de wetenschap.
- 4 De *h*-index zou zinniger worden door hem slechts te berekenen over de artikelen die de afgelopen 10 jaar gepubliceerd zijn.
- 5 De gemiddelde wetenschappelijke leeftijd van een begeleider, ruwweg 20 jaar, geeft een tijdschaal waarop ouder wetenschappelijk werk herondekt wordt.
- 6 Wolken en wasmachines laten zien dat de virtuele potentiële temperatuur en sokken geen behouden grootheden zijn.
- 7 De schoonheid van wetenschappelijk onderzoek kan niet worden uitgelegd, maar moet worden ondergaan.
- 8 Het probleem van zowel de evolutieer als klimaatonderzoek is dat beide en plein public zijn opgegroeid; dit resulteert in een hardnekkig geloof in hun kinderziektes.
- 9 Universiteiten zouden meer en betere promovendi vinden als ze de creativiteit en verscheidenheid in de wetenschap zouden aanprijzen, in plaats van de beperkte breedte van een promotietraject.
- 10 Referenda impliceren een diskwalificatie van politici voor hun werk, en geven dus een rechtvaardiging voor salarissen van topbestuurders hoger dan dat van de minister-president.
- 11 De afdelingsvoorzitter van multi-scale physics aan de TU Delft wordt onderbetaald.

Deze stellingen worden opponeerbaar en verdedigbaar geacht en zijn als zodanig goedgekeurd door de promotor, prof. dr. ir. H. E. A. van den Akker.

SUMMARY IN ENGLISH

Driving home, the sky accelerates
And the clouds all form a geometric shape

THE FLAMING LIPS

Cumulus clouds have since long been one of the greatest challenges in the atmospheric sciences. For a correct representation of clouds in weather and climate models, where they are the biggest unknowns, a good understanding of the interaction between cloud and environment is of prime importance. In this thesis, this problem is attacked with a combination of detailed large-eddy simulations (LES) and air-plane observations.

While the traditional view states that air inside the cloud goes up, and all the air outside goes down in compensation, it is found here that on average, the air far away from the cloud hardly moves. There, air only moves in oscillating gravity waves or in small scale turbulence. Most of the compensating downward motion happens in the direct vicinity of the cloud, in a subsiding shell. The subsiding shell can be clearly observed in various case studies, in LES as well as in airplane observations. To appreciate the subsiding shell as more than just an area with slightly negative velocity, it is important not to look at the vertical velocity (as is intuitive in air-plane observations), but to look at the vertical mass flux. This way, the relatively large area of the shell compared to the cloud core can be taken into account.

The origin of this subsiding shell is examined by analyzing the individual terms of the vertical momentum equation. Buoyancy is found to be the driving force for this shell, and it is counteracted by the pressure gradient force. This shows that evaporative cooling at the cloud edge, induced by lateral mixing of cloudy and environmental air, is the responsible mechanism behind the descending shell. The role of the shell in cloud-environment interaction is further explored and described in a conceptual three-layer model of the cloud. In the end, the shell creates a buffer layer that interferes with the interaction between cloud and environment, although vertical shear is able to skew the cloud, hence creating a preferred location for the subsiding shell.

A related classical problem in cumulus cloud research is the determination of the source of in-cloud air. Here, this problem is studied by two distinct methods: 1) by analyzing conserved variable mixing diagrams (Paluch diagrams), and 2) by tracing back cloud-air parcels represented by massless Lagrangian particles that follow the LES flow. The obtained Paluch diagrams are found to be similar to many results found in literature, but the source of entrained air found by particle tracking deviates from the source inferred from the Paluch analysis, even more than can be explained by buoyancy sorting. Whereas the classical Paluch analysis

seems to provide some evidence for cloud-top mixing, backwards particle tracking shows that virtually all mixing occurs laterally. Particle trajectories averaged over the entire cloud ensemble also clearly indicate the absence of significant cloud-top mixing in shallow cumulus clouds.

To study the evolution of clouds in time as well as in space, a statistical life-cycle analysis has been conducted. Although trained observers have no problem in distinguishing between the various lifestages of a cloud, this process proves difficult to automate, since cloud-splitting and cloud-merging events complicate the distinction between a single system consisting of several cloudy parts and two independent systems that collided. Because human perception is well-equipped to capture and to make sense of these time-dependent three-dimensional features, a combination of automated constraints and human inspection in a 3D virtual reality environment is used to select clouds that are exemplary in their behavior throughout their entire lifespan. The considerable number of selected clouds warrant reliable statistics of cloud properties conditioned on the phase in their life cycle.

The most dominant feature in this statistical life-cycle analysis is the pulsating growth that is present throughout the entire life time of the cloud. The pulses are a self-sustained phenomenon, driven by a balance between buoyancy and horizontal convergence of dry air. The convective inhibition just above cloud base plays a crucial role as a barrier for the cloud to overcome during its infancy stage, and as a buffer region later on, ensuring a steady supply of buoyancy into the cloud.

SAMENVATTING IN HET NEDERLANDS

In de auto, van de week
zag ik een wolk die op Arafat leek

SPINVIS

Mooiweerwolken behoren sinds jaar en dag tot de grootste uitdagingen in de atmosferische wetenschappen. Voor een goede representatie van wolken weer- en klimaatmodellen, waar wolken een grote onzekerheid zijn, is een goed begrip van de interactie tussen wolk en omgeving van belang. In dit proefschrift wordt dit probleem benaderd met een combinatie van gedetailleerde "large-eddy simulaties" (LES) en van vliegtuigmetingen.

Waar een wolk gewoonlijk wordt omschreven als een entiteit waarin lucht omhoog gaat, en dat overal rond de wolk de lucht ter compensatie naar beneden gaat, wordt hier aangetoond dat de lucht ver weg van de wolk gemiddeld nauwelijks verplaatst. Alleen oscillerende zwaartekrachtsgolven en kleinschalige turbulentie komen daar voor. Het grootste gedeelte van de compenserende neerwaardse stroming vindt plaats direct om de wolk heen, in een ring van dalende lucht. De ring wordt duidelijk gezien voor verschillende casestudies, zowel in LES als in observaties. Om de ring echter voor meer aan te zien dan een gebied met ietwat negatieve verticale snelheden, is het belangrijk om niet daar de snelheid te kijken (zoals gebruikelijk voor vliegtuigobservaties) maar naar de massaflux. Op die manier kan het relatief grote oppervlakte van de wolkenrand in rekening worden gebracht. De mechanismes die ten grondslag liggen aan deze dalende ring worden hier geanalyseerd met behulp van de individuele termen van de verticale impulsvergelijking. Het dichtheidsverschil blijkt de drijvende kracht te zijn achter de ring; de drukgradientkracht werkt in tegengestelde richting. Dit betekent dat het koelend effect van verdamping aan de rand van de wolk en gedreven door horizontale menging verantwoordelijk is voor de dalende ring. De interactie tussen wolk en omgeving kan worden beschreven door een conceptueel drielagenmodel waarin de rol van de dalende ring in de mengprocessen nader bestudeerd wordt. Het uiteindelijke effect van de neergaande ring is dat interactie tussen wolk en omgeving kan alleen maar gebeuren door de bufferlaag die door de ring wordt gecreëerd. Verticale schering kan de wolk nog wel scheef trekken, en zo een voorkeurslocatie genereren voor de ring.

Een gerelateerd en klassiek probleem in onderzoek naar cumulus bewolking is de bepaling van de bron van de lucht in de wolk. Hier wordt dit probleem bestudeerd met behulp van twee verschillende methodes: Ten eerste met behulp van behoudengroothedenmengdiagrammen (zg. Paluchdiagrammen) en ten tweede door wolkenluchtpakketjes terug te volgen met behulp van lagrangiaanse deeltjes die met de stroming meegaan. De verkregen Paluchdiagrammen zijn vergelijkbaar met vele

resultaten uit de literatuur, maar de bron van meegevoerde lucht volgens de lagrangiaansedeeltjesanalyse wijkt af van de door de Paluchdiagrammen gesuggereerde bron, meer dan kan worden verklaard met behulp van selectie door dichtheidsverschillen. Hoewel de klassieke Paluchanalyse wijst op menging aan de wol Kentop laat de deeltjesanalyse zien dat vrijwel alle menging horizontaal gebeurt. Bovendien laat middeling van deeltjesbanen over het volledige wolkenensemble duidelijk zien dat er geen menging van belang is aan de top van een mooiweerwolk.

Om de evolutie van wolken als functie van de tijd, en niet alleen van de plaats, te bestuderen, wordt een statistische levensloopenalyse uitgevoerd. Hoewel geofende observationalisten gemakkelijk onderscheid maken tussen de verschillende levensfasen van een wolk, blijkt een dergelijke selectie moeilijk te automatiseren, aangezien afsplitsingen en samenvoegingen van wolken een helder onderscheid verhinderen tussen één wolkensysteem verdeeld over meerdere stukken, of twee onafhankelijke systemen die samenkomen. Het menselijk oog goed is uitgerust om dit soort tijdsafhankelijke, driedimensionale gebeurtenissen te herkennen, en daarom worden hier, door middel van een combinatie van geautomatiseerde criteria en menselijke observaties in a 3D-virtualrealityomgeving, wolken geselecteerd die door hun volledige levensloop gaan. Dankzij de aanzienlijke hoeveelheid wolken die zo op een snelle manier geselecteerd kunnen worden, kan een betrouwbare statistiek van iedere levensfase opgebouwd worden. De meest in het oog springende eigenschap in deze levensloopenalyse is de pulserende groei van de wolken gedurende de gehele levensloop. Deze pulsen houden zichzelf in stand en worden gedreven door een evenwicht tussen dichtheidsverschillen en horizontale convergentie van droge lucht. De “convective inhibition (CIN)” net boven de wolkenbasis is cruciaal als een barrière die de wolk moet overwinnen aan het begin van zijn leven, en later speelt de CIN een rol als bufferlaag, die de wolk verzekerd van een gestage aanvoer van buoyancy.

CONTENTS

1	Introduction	1
1.1	Clouds and climate	1
1.2	Historical summary	3
1.3	This thesis	5
1.4	Outline	6
2	Large-Eddy Simulations of the Atmospheric Boundary Layer	7
2.1	Thermodynamical definitions	7
2.2	The governing equations	9
2.3	Subfilter-scale model	10
2.4	Discretization and numerical scheme	12
2.5	Condensation scheme	14
2.6	Boundary conditions	15
2.7	Sensitivity to numerical issues	15
2.8	Lagrangian particle advection	18
3	Subsiding Shells around Shallow Cumulus Clouds	19
3.1	Introduction	19
3.2	Description of the large-eddy simulations	21
3.3	Comparison with observations	23
3.4	Investigation of the terms of the vertical momentum equation	25
3.5	Analysis of BOMEX	26
3.6	Three-layer model	34
3.7	Conclusions	40
3.A	Advection scheme	43
4	Observational Validation of the Compensating Mass Flux through the Shell around Cumulus Clouds	45
4.1	Introduction	45
4.2	Data description and methodology	47
4.3	Validation of the refined mass-flux model	53
4.4	A closer look at the up- and downdrafts	57
4.5	The velocity distributions in cloud, shell, and environment	63
4.6	Conclusions	65
5	Mixing in Shallow Cumulus Clouds Studied by Lagrangian Particle Tracking	67
5.1	Introduction	67
5.2	Case Setup	70

5.3	Detailed cloud investigation	71
5.4	Ensemble averaging over the cloud field	77
5.5	Net vertical transport due to clouds	83
5.6	Conclusions	85
5.A	Validation of tracer particles in cumulus flow	89
6	A Statistical Approach to the Life-cycle Analysis of Cumulus Clouds Selected in a Virtual Reality Environment	93
6.1	Introduction	93
6.2	Methodology	95
6.3	Inspection of individual clouds	99
6.4	Statistical representation	106
6.5	How sharp are the edges?	114
6.6	Conclusions	116
7	Concluding Remarks	119
7.1	Overview	119
7.2	Outlook	121
	References	125
	Acknowledgments	135
	About the Author	139

CHAPTER 1: INTRODUCTION

Hurry up, come figure out
What's behind a million clouds

CAESAR

Throughout the ages, cumulus clouds have always been able to captivate us. Aristophanes named a play after them back in 419 BC, some of Jacob van Ruysdaels paintings were dominated by cumuli, and a poet like Martinus Nijhoff also described what the clouds of his youth (and of his son's) looked like. But despite millennia of interest, the behavior of clouds is one of the most difficult processes in the atmosphere.

1.1 CLOUDS AND CLIMATE

Cumulus clouds play a complicated role in the climate system, and they are associated with mechanisms that cause positive feedbacks (i.e., additional warming in a warming climate) as well as with mechanisms that cause negative feedbacks. From any satellite picture, the reflection of visible light (the albedo) by clouds can be appreciated; an increase in cloud cover would immediately cool the Earth surface. The detailed microphysical structure of clouds is also important for the planetary albedo; a cloud that consists of many small droplets will reflect more sunlight than a cloud that consists of the same amount of water, divided over a few large droplets.

The dynamics of cumulus clouds also forms an important link in the climate system in other ways. Cumuli enhance the transport of heat and moisture between the clear convective boundary layer (the first few hundred metres below cloud base) and higher regions of the troposphere. Due to such transport, shallow cumuli are able to wetten the higher troposphere, which paves the way for deeper convection and cumulonimbus clouds. This mechanism is especially important within the Hadley circulation, where the deep convection is fueling the large-scale atmospheric circulation from the equator to the sub-tropics that is crucial for the distribution of heat over the earth. The transporting property of clouds is not only important in the distribution of heat and moisture. Boundary layer clouds also play a complicated role in the transport of chemical reactive species (e.g., ozone), or in dispersion of pollution in general.

Since the typical horizontal size of shallow cumulus clouds is much smaller than the grid size of large-scale weather and climate models, their behavior cannot be resolved by the mesh of those models. Thus, the role these clouds play in the atmosphere and in the Earth radiation budget needs to be parameterized, i.e., represented in the model in some statistical sense. Naturally, this can only be done properly if the relevant processes are well understood.

A textbook view of cumulus clouds in the Atmospheric Boundary Layer (ABL) is depicted schematically in figure 1.1. Induced by solar heating, parcels of air rise in thermals from the earth surface through the (well mixed) subcloud layer. When the parcel is dry, it cannot overcome the relatively more buoyant layer that is capping the subcloud layer. When the parcel contains some moisture however, the situation can be different. The momentum gained in the subcloud layer may then bring the air up to the level where some water vapor starts to condensate, the so-called Lifting Condensation Level (LCL). The heat released during this condensation makes the parcel more buoyant, and the air becomes positively buoyant if the parcel is able to reach the Level of Free Convection (LFC). The cloud has now turned from a forced cloud into an active one, and as there is water vapor to condensate, the air in the cloud will gain buoyancy and accelerate.

At some point, however, this process stops. This is either because the cloud has reached the inversion layer, where the surrounding air becomes much warmer, or because the cloud top is so much diluted by mixing with the environment that the water content within the cloud gets below saturation level. Due to the vertical velocity gained before, the cloud may continue to rise a while, but it will decelerate and swiftly evaporate due to mixing with the environment. At various places and times, chunks of cloud may break from the main cloud, or the subcloud thermal may vanish altogether. These passive clouds are deprived from their source and are bound to mix with the environment and disappear.

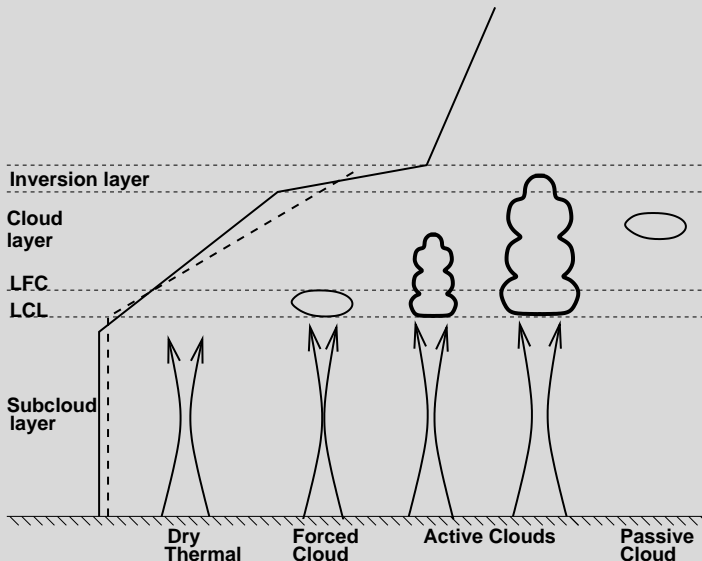


Figure 1.1: A schematic overview of an atmospheric boundary layer containing cumulus clouds. The full line depicts the virtual potential temperature of the environment; the dashed line is the virtual potential temperature of an (active) cloud and the thermal beneath the cloud.

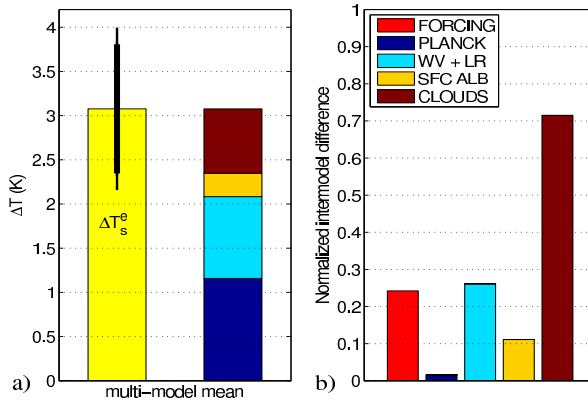


Figure 1.2: For a CO₂ doubling, (a) multi-model mean ± 1 standard deviation (thick line) and 5%-95% interval (thin line) of the equilibrium temperature change (ΔT_s^e), and contributions to this temperature change associated with the Planck response, combined water vapor and lapse rate (WV+LR) feedback, surface albedo feedback and cloud feedback. (b) inter-model standard deviation of the temperature change estimates associated with the radiative forcing, the Planck response and the various feedbacks normalized by the inter-model standard deviation of the equilibrium temperature change ΔT_s^e reported in (a). Taken from Dufresne and Bony (2008).

The precise behavior of clouds in a changing climate is the biggest uncertainty in climate modeling (Bony et al., 2006; IPCC, 2007). This is illustrated in Dufresne and Bony (2008) by the differences between various climate models. These models are all different in the details of modeling the atmospheric processes, and so is their prediction of the change of temperature after doubling the amount of atmospheric CO₂. The biggest part of the temperature increase is caused by the Planck response, i.e, the direct impact of the greenhouse effect. However, this effect is well understood; the standard deviation between the models is only in the order of 1%. The secondary effects (i.e., the mechanisms that are triggered by the temperature change due to the Planck effect) are much more unclear. The biggest inter-model standard deviation is seen in the cloud-climate feedback. The uncertainty in this effect is as large as the the standard deviation in the total temperature change, see figure 1.2. A better understanding and parameterization of clouds should improve this.

1.2 HISTORICAL SUMMARY

Many parameterizations in current numerical weather predictions (NWP) and climate models are based on a mass-flux scheme (e.g., Betts, 1975; Arakawa and Schubert, 1974; Tiedtke, 1989; Bretherton et al., 2004). In such parameterizations, only the effect of the entire field of clouds onto the large-scale mean state is considered. Often, the concept of these parameterizations is conceptualized as a single

bulk cloud that represents the behavior of all clouds combined. The behavior of this bulk cloud is not necessarily similar to the physics of the individual clouds, especially since clouds of different types, sizes and lifestages are represented by this single bulk cloud. Air moves upward within this bulk cloud, this upward flow is compensated by down flow of environmental air. Transport between cloud and environment is often modeled using prescribed entrainment and detrainment relations (Siebesma and Cuijpers, 1995; Siebesma and Holtslag, 1996). A good understanding of the interaction between the real clouds and their environment can help in describing these entrainment and detrainment relations for the bulk cloud, and thereby improving the quality of the parameterizations in large-scale models.

It may not come as a surprise that cloud-environment interaction has been studied frequently over the years. The first pioneering studies (e.g., Bjerkness, 1938; Stommel, 1947; Malkus, 1952; Scorer and Ludlam, 1953; Malkus et al., 1953; Malkus and Scorer, 1955; Squires, 1958a,b,c; Warner and Squires, 1958; Asai and Kasahara, 1967) were mainly qualitative and/or analytical by necessity, since research tools like radar, satellite imagery, high resolution air-plane measurements, or computer simulations were barely developed in the midst of the twentieth century. Nevertheless, many of their findings turned out to be highly accurate, and even if their hypotheses were falsified, they did often yield great insight.

Over the years, many measurement campaigns have been set up to learn more about the dynamics, microphysics and chemistry of clouds. These measurement campaigns include, for instance, the Barbados Oceanographic and Meteorological EXperiment (BOMEX, Holland and Rasmusson, 1973), the Atlantic Trade Wind EXperiment (ATEX, Augstein et al., 1973), in Kansas and Oklahoma during the Southern Great Plains/Atmospheric Radiation Measurement (SGP-ARM), the Small Cumulus Microphysics Study (SCMS, Knight and Miller, 1998) in Florida and the Rain in Cumulus over the Ocean (RICO, Rauber et al., 2007a) campaign near Barbuda. These campaigns utilized an ever increasing variety of measurement equipment, such as measurement air planes and ships, ground-based radar stations, satellite measurements, and radio sondes.

While the campaigns all yielded an enormous amount of data resulting in countless interesting analyses, still a rather sparse fraction of the 3-dimensional, time dependent field of the relevant variables (like velocity, pressure, temperature and moisture) could be measured. This means that rather indirect techniques and involved interpretations were necessary to answer many of the open questions. As an example, a recurring debate has been the role of cloud-top mixing compared with lateral mixing between cloud and environment. Clearly, either mechanism would, in the limit, suggest completely different cloud dynamics, and might result in different parameterizations. Since the origin of in-cloud air cannot easily be tagged, Paluch (1979) resorted to the elegant yet indirect method of conserved variables mixing diagrams that were named after her. Paluch concluded a large role for cloud-top mixing, and the Paluch diagrams were extensively used in discussions of this topic in subsequent studies (Raymond and Wilkening, 1982; Lamontagne and Telford, 1983; Jensen et al., 1985; Austin et al., 1985; Reuter and Yau, 1987b; Blyth

et al., 1988). Taylor and Baker (1991), however, offered an alternative interpretation for the Paluch diagrams that favored lateral mixing instead. Since then, other, more and more direct studies on the topic have been conducted, although none yielded sufficiently decisive evidence in favor of either lateral mixing or cloud-top mixing.

Since the late sixties, Large-Eddy Simulations (LES) have more and more aided observational studies (e.g., Lilly, 1967; Deardorff, 1972); cumulus-topped boundary layers were first simulated by Sommeria (1976). The principle of LES is to resolve only the larger turbulent scales and model the scales below a certain filter width. This filter width is usually related to the grid size of the LES, and ranges typically between 10 and 100 meter for current state-of-the-art simulations of the cloud-topped ABL.

Although LES can be considered to be the most detailed numerical tool available to study the ABL, care should always be taken to evaluate results from simulations with observations. This has been done, in varying detail, in a series of LES-intercomparison studies by the GEWEX (Global Energy and Water Cycle Experiment) Cloud System Study (GCSS) Boundary Layer Cloud Working Group. Cumulus clouds were studied in intercomparisons based on BOMEX (Siebesma et al., 2003), ATEX (Stevens et al., 2001), ARM (Brown et al., 2002) and RICO (van Zanten et al., 2008). In general, the large-scale properties of cloud fields seemed to be well simulated in most cases, although for very critical cases or for detailed physics of individual clouds careful comparison with observation remains necessary.

1.3 THIS THESIS

The present research stands in the tradition of more than half a century research on cloudy boundary layers. With the use of LES all the relevant quantities are available in 3 spatial dimensions and evolving in time, and in combination with the vast amount of observational data, cloud-environment interaction can be studied in more detail than ever before. In fact, one of the challenges of current atmospheric research is the availability of *too much* data; with LES, terabytes of data can easily be produced, but processing everything is so cumbersome that traditional methods rarely take advantage of all available data. Therefore, part of the aim of this research is to look at the data in ways that are better optimized for the research questions we are addressing.

A high (spatial) resolution is essential, since the typical size of the region where mixing between cloud and environment occurs is about 100 meters. Much of the focus in this thesis will lie on the role of the subsiding shell around the cumulus clouds, and on the mechanisms that drive it. Although the shell can be easily hidden behind the turbulent fluctuations (see figure 1.3), it has often been observed before, especially if we look, with the knowledge of today, at observations all the way back to Malkus et al. (1953). It is so far unclear what the role of this shell in the dynamics of cumulus clouds, and what kind of mechanisms drive the shell. Potentially, the shell could play a significant role in cloud-environment interaction. Furthermore,

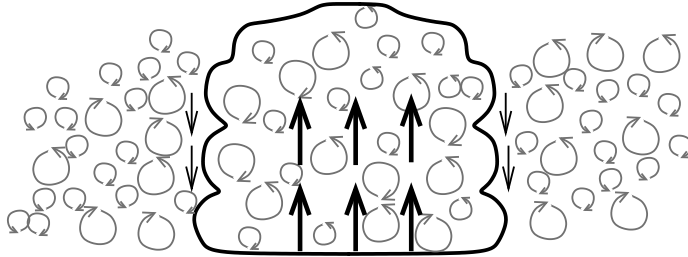


Figure 1.3: A narrow subsiding shell can often be observed directly around cumulus clouds. However, this shell can easily be interpreted as a turbulent fluctuation.

since the air in the shell descends, it could alter the mass flux balance of the cloud system that is so important in many parameterizations of cumulus clouds.

While the life time of a cumulus cloud (typically half an hour) is not that long, the residence time of an air parcel within a cloud (a few minutes) is even much shorter. However, the evolution of such an air parcel while it moves between the cloud and the environment is exactly the topic of interest here. With a careful choice of methodology and visualization, this time dependency can be properly addressed.

1.4 OUTLINE

The outline of the thesis is as follows. Chapter 2 consists of an overview of the Dutch Atmospheric LES (DALES) code that was used; although it has been described several times before, the ongoing evolution of DALES calls for an up-to-date description. Chapters 3 and 4 treat the mechanics behind the layer of subsiding air that is observed around clouds. Comparisons between observations and numerical results are made here, and the notable role this shell appears to play in the mass-flux distribution of the cloud layer is extensively explored. Also treated in these chapters are the effects of vertical shear on the shell, and the distribution of downdrafts in the cloud, the shell and the environment. Chapter 5 addresses once again the relevance of cloud-top and lateral mixing. It does so by allowing Lagrangian tracer particles to follow the flow, thus resolving entrainment and detrainment issues in a very direct manner. Discrepancies with traditional (more indirect) methods are also discussed. Chapter 6 is a study of the life cycle of individual clouds. Using a 3D virtual reality environment (VE), clouds evolving in time can be picked out of the ensemble and their entire lifetime from young ascending cloud until passive dying cloud can be studied. Due to the fast cloud selection with help of the VE, a statistical approach to the life-cycle analysis becomes feasible, beyond just looking at a few individual clouds. In chapter 7, general conclusions beyond the scope of each individual chapter are given. This results in a discussion of the mechanisms of mixing between cloud and environment, and a discussion of what further needs to be done to explore the consequences of this study.

CHAPTER 2: LARGE-EDDY SIMULATIONS OF THE ATMOSPHERIC BOUNDARY LAYER

Futures made of virtual insanity
now always seem to be governed by this love we have
For useless, twisting, our new technology

JAMIROQUAI

The Dutch Atmospheric Large-Eddy Simulation (DALES) code has a long history. Rooted in the LES of Nieuwstadt and Brost (1986), Cuijpers and Duynkerke (1993) provides a general description of DALES, but large parts of the code have been changed ever since. Over the years, contributions of many people resulted in the current version 3 of DALES, amongst many others, Hans Cuijpers (1994), Pier Siebesma, Mathieu Pourquie, Jordi Vilà-Guerau de Arellano, Harm Jonker, Margreet van Zanten (2000), Stephan de Roode, Roel Neggers, Alessandro Dosio (2005), and Chiel van Heerwaarden. As a part of this PhD project, the LES has been revised, the numerical schemes have been changed, and the Lagrangian particle dispersion model has been implemented. The chapter below gives a general description of the current state of the code.

2.1 THERMODYNAMICAL DEFINITIONS

In DALES, the thermodynamical state of the ABL is described in quantities conserved for moist adiabatic processes, i.e., including phase changes between liquid water and vapor. Therefore, we need to define 1) the total water mixing ration q_t , and 2) the liquid water potential temperature θ_l .

The total water mixing ratio is defined as the ratio between the mass of water (vapor plus liquid) in an air parcel and the mass of the dry air in that same air parcel. In the warm ABL, where no ice is present, it is defined as

$$q_t = q_l + q_v; \quad (2.1)$$

q_t is a conserved variable. q_l denotes the mass ratio between liquid water and dry air; q_v is the similarly defined water vapor mixing ratio. Effects of supersaturation are neglected, so if the total water mixing ratio is smaller than the saturation mixing ratio q_s , q_t equals q_v and the liquid water mixing ratio is zero. If q_t is larger than q_s , the liquid water mixing ratio is equal to the difference between q_t and q_s , and the water vapor mixing ratio is equal to the saturation mixing ratio.

In contrast to the total water content, temperature is not conserved for adiabatic processes, since it is altered under variation of the mean pressure or under phase

changes. A few quantities can be derived from the temperature that take these effects into account. The liquid and equivalent potential temperature (θ_l and θ_e), that are conserved, as well as the virtual potential temperature (θ_v), that can serve as a marker for the density, are addressed below.

For adiabatic processes, the density ρ , temperature T , pressure p , the heat capacity c_p and the specific gas constant R of a parcel of air are related to each other by

$$c_p dT = \frac{1}{\rho} dp, \quad (2.2)$$

$$p = \rho RT, \quad (2.3)$$

which combines to

$$d \ln T = \frac{R}{c_p} d \ln p. \quad (2.4)$$

The potential temperature θ is defined as the temperature a parcel of air would have if it was brought adiabatically to the reference pressure $p_0 = 1 \times 10^5$ Pa. Integrating equation 2.4 now yields for dry air:

$$\theta = \frac{T}{\Pi}, \quad (2.5)$$

where we defined the following quantities:

$$\Pi = \left(\frac{p}{p_0} \right)^\chi, \quad (2.6)$$

$$\chi \approx \frac{R_d}{c_{pd}}, \quad (2.7)$$

with $R_d = 287.0 \text{ J kg}^{-1} \text{ K}^{-1}$, and $c_{pd} = 1004 \text{ J kg}^{-1} \text{ K}^{-1}$ the gas constant and heat capacity of dry air.

The liquid potential temperature (θ_l) is the potential temperature a parcel would have if all its liquid water were evaporated, thus cooling the parcel; it is a conserved quantity under reversible transformations of fluid parcels. As explained in Emanuel (1994), θ_l is approximately equal to:

$$\theta_l \approx \theta - \frac{L}{c_{pd}\Pi} q_l, \quad (2.8)$$

with $L = 2.5 \times 10^6 \text{ J kg}^{-1}$ the latent heat release of vaporization. The wet equivalent potential temperature (θ_e or sometimes θ_q) is the potential temperature a parcel would have if all its moisture were condensed and the resultant latent heat release was used to warm the parcel. It is defined by Paluch (1979), and can be approximated as:

$$\theta_e \approx \theta + \frac{L}{c_{pd}\Pi} q_v = \theta_l + \frac{L}{c_{pd}\Pi} q_t. \quad (2.9)$$

The virtual potential temperature (θ_v) of a parcel is the potential temperature of a dry air parcel with the same density, which means that it can be used in a modified form of the gas law:

$$\frac{p}{\rho} = R_d \theta_v \Pi. \quad (2.10)$$

In good approximation, θ_v is equal to:

$$\theta_v \approx \left(\theta_l + \frac{L}{c_{pd} \Pi} q_l \right) \left(1 - \left(1 - \frac{R_v}{R_d} \right) q_t - \frac{R_v}{R_d} q_l \right). \quad (2.11)$$

In an ABL without ice, q_t , θ_l and θ_e (and combinations of these variables) are conserved variables for adiabatic processes and for phase changes. If two are known, in combination with the pressure, the third can be calculated. In DALES, we have chosen to use q_t and θ_l as prognostic variables, and to diagnose all other quantities where needed. For processes that include precipitation, these variables are not conserved anymore, and a microphysics model is necessary to account for the influence of these processes on the dynamics in the LES flow. While DALES incorporates such a microphysics scheme, this thesis only treats non-precipitating cumuli, and the effects of precipitation are ignored in the remainder of this chapter.

2.2 THE GOVERNING EQUATIONS

Under the Boussinesq approximation and after application of the LES filter, the equations of motion are:

$$\frac{\partial \tilde{u}_i}{\partial x_i} = 0, \quad (2.12)$$

$$\frac{\partial \tilde{u}_i}{\partial t} = -\frac{\partial \tilde{u}_i \tilde{u}_j}{\partial x_j} - \frac{\partial \pi}{\partial x_i} + \frac{g}{\theta_0} (\tilde{\theta}_v - \theta_0) \delta_{i3} - 2\epsilon_{ijk} \Omega_j \tilde{u}_k + F_i - \frac{\partial \tau_{ij}}{\partial x_j}, \quad (2.13)$$

$$\frac{\partial \tilde{\theta}_l}{\partial t} = -\frac{\partial \tilde{u}_j \tilde{\theta}_l}{\partial x_j} + S_{\theta_l} - \frac{\partial R_{u_j, \theta_l}}{\partial x_j}, \quad (2.14)$$

$$\frac{\partial \tilde{q}_t}{\partial t} = -\frac{\partial \tilde{u}_j \tilde{q}_t}{\partial x_j} + S_{q_t} - \frac{\partial R_{u_j, q_t}}{\partial x_j}, \quad (2.15)$$

as basic equations, where the tildes denotes the filtered mean variables. The \hat{z} direction is taken to be vertical. θ_0 is the reference state potential temperature and $\vec{\Omega}$ is the earth's angular velocity. Viscous transport terms are neglected. F_i represents large scale forcings. The large-scale source terms for scalar φ are given by S_φ . The subfilter-scale (SFS), or residual, scalar fluxes are denoted by $R_{u_j, \varphi} \equiv \widetilde{u_j \varphi} - \tilde{u}_j \tilde{\varphi}$, i.e., the contribution to the resolved motion from all scales below the LES filter width. The anisotropic SFS-stress tensor is defined by

$$\tau_{ij} \equiv \widetilde{u_i u_j} - \tilde{u}_i \tilde{u}_j - \frac{2}{3} \delta_{ij} \tilde{\epsilon}, \quad (2.16)$$

where $\tilde{e} = \frac{1}{2}(\widetilde{u_i u_i} - \widetilde{u_i} \widetilde{u_i})$ is the subfilter-scale turbulent kinetic energy (SFS-TKE). The isotropic part of the subfilter-scale flux is included in the modified pressure

$$\pi = \frac{1}{\rho_0}(\tilde{p} - p_0) + \frac{2}{3}e, \quad (2.17)$$

which is determined by solving a Poisson equation for π

$$\frac{\partial^2 \pi}{\partial x_i^2} = \frac{\partial}{\partial x_i} \left(-\frac{\partial \widetilde{u_i} \widetilde{u_j}}{\partial x_j} + \frac{g}{\theta_0}(\tilde{\theta}_v - \theta_0)\delta_{i3} - 2\varepsilon_{ijk}\Omega_j \widetilde{u_k} + F_i - \frac{\partial \tau_{ij}}{\partial x_j} \right). \quad (2.18)$$

Since computations are performed in a double periodic domain, the Poisson equation is solved with a Fast Fourier Transform in the homogenous directions, while for the \hat{z} direction a tridiagonal system is solved.

2.3 SUBFILTER-SCALE MODEL

The SFS stress tensor and scalar fluxes are modeled using one-and-a-half order closure (Deardorff, 1973):

$$\tau_{ij} = -K_m \left(\frac{\partial \widetilde{u_i}}{\partial x_j} + \frac{\partial \widetilde{u_j}}{\partial x_i} \right), \quad (2.19)$$

$$R_{u_j, \varphi} = -K_h \frac{\partial \tilde{\varphi}}{\partial x_j}, \quad (2.20)$$

with the eddy diffusivity coefficients K_m and K_h being a function of \tilde{e} . The prognostic equation for \tilde{e} :

$$\frac{\partial \tilde{e}}{\partial t} = -\widetilde{u_j} \frac{\partial \tilde{e}}{\partial x_j} - \tau_{ij} \frac{\partial \widetilde{u_i}}{\partial x_j} + \frac{g}{\theta_0} R_{w, \theta_v} - \frac{\partial R_{u_j, e}}{\partial x_j} - \frac{1}{\rho_0} \frac{\partial R_{u_j, p}}{\partial x_j} - \varepsilon, \quad (2.21)$$

with ε the dissipation rate. To close equation 2.21, we need to parameterize all the right-hand-side terms but the first one. The SFS-TKE production by shear (the second term) is closed with equation 2.19. Following Deardorff (1980), we use for the third term, the production due to buoyancy:

$$\frac{g}{\theta_0} R_{w, \theta_v} = \frac{g}{\theta_0} (AR_{w, \theta_t} + BR_{w, q_t}), \quad (2.22)$$

with coefficients A and B depending on the local thermodynamic state:

$$\begin{cases} A = 1 & B = \left(1 - \frac{R_v}{R_d}\right) \theta_0 & \text{for } \tilde{q}_t < \tilde{q}_s \\ A = \frac{1 + \frac{R_v}{R_d} \left(\theta_0 \frac{d\tilde{q}_s}{dT}\right)}{1 + \frac{L}{c_{pd}} \frac{d\tilde{q}_s}{dT}} & B = \frac{L}{c_{pd}} A - \theta_0 & \text{for } \tilde{q}_t > \tilde{q}_s \end{cases} \quad (2.23)$$

The fourth and fifth term in equation 2.21 are together parameterized as

$$-\frac{\partial}{\partial x_j} \left(R_{u_j, e} + \frac{1}{\rho_0} R_{u_j, p} \right) = 2K_m \frac{\partial \tilde{e}}{\partial x_j}, \quad (2.24)$$

Under the assumption of 3D homogenous isotropic turbulence, and for a sharp spectral cutoff filter, the dissipation rate ε can be found by integration of the energy spectrum $E(k) = \alpha \varepsilon^{2/3} k^{-5/3}$ from a filter wavenumber k_f , that lies within the inertial subrange, to infinity

$$\varepsilon = \tilde{e}^{-3/2} k_f \left(\frac{3}{2} \alpha \right)^{-3/2}, \quad (2.25)$$

with $\alpha = 1.5$ denoting the Kolmogorov constant. The production of SFS-TKE is equal to:

$$\begin{aligned} \mathcal{P} &= 2K_m \int_0^{k_f} k^2 E(k) dk \\ &= \frac{3}{2} K_m \alpha \varepsilon^{2/3} k_f^{4/3}. \end{aligned} \quad (2.26)$$

The eddy diffusivity for momentum can be found by equating locally the production of SFS-TKE to the dissipation:

$$\begin{aligned} \mathcal{P} &= \varepsilon \\ \frac{3}{2} K_m \alpha \varepsilon^{2/3} k_f^{4/3} &= \tilde{e}^{-3/2} k_f \left(\frac{3}{2} \alpha \right)^{-3/2} \\ K_m \tilde{e} k_f^2 &= \tilde{e}^{-3/2} k_f \left(\frac{3}{2} \alpha \right)^{-3/2}. \end{aligned} \quad (2.27)$$

This yields, for K_m ,

$$K_m = \frac{\tilde{e}^{-1/2}}{k_f} \left(\frac{3}{2} \alpha \right)^{-3/2} = c_m \lambda \tilde{e}^{-1/2}, \quad \text{with} \quad c_m = \frac{c_f}{2\pi} \left(\frac{3}{2} \alpha \right)^{-3/2} \quad (2.28)$$

where we defined the filter width $c_f \lambda = \frac{2\pi}{k_f}$. The eddy diffusivity for heat is modeled similarly as $K_h = c_h \lambda \tilde{e}^{-1/2}$, and for the dissipation ε we can write:

$$\varepsilon = \frac{c_\varepsilon}{\lambda} \tilde{e}^{-3/2}, \quad \text{with} \quad c_\varepsilon = \frac{2\pi}{c_f} \left(\frac{3}{2} \alpha \right)^{-3/2} \quad (2.29)$$

In unstable flow, $c_f \lambda$ can be taken proportional to the grid size:

$$\lambda = \Delta = (\Delta x \Delta y \Delta z)^{1/3}, \quad (2.30)$$

$$c_f = 2.5, \quad (2.31)$$

α	c_f	$c_{\varepsilon,1}$	$c_{\varepsilon,2}$	c_m	$c_{h,1}$	$c_{h,2}$	c_N
1.5	2.5	0.19	0.51	0.12	1	2	0.76

Table 2.1: An overview of the parameters used in the SFS scheme of DALES model. Not all parameters are independent.

see Cuijpers (1990). However, this no longer holds for stable flow, i.e., where $\frac{\partial \tilde{\theta}_v}{\partial z} > 0$. In that case, λ is taken to be

$$\lambda = \min \left(\Delta, c_N \frac{\tilde{e}^{-1/2}}{N} \right), \quad (2.32)$$

with $N^2 = \frac{g}{\theta_0} \frac{\partial \theta_v}{\partial z}$ denoting the Brunt-Väisälä frequency, and $c_N = 0.76$. A stability correction is also applied on c_h and c_ε :

$$c_h = \left(c_{h,1} + c_{h,2} \frac{\lambda}{\Delta} \right) c_m, \quad (2.33)$$

$$c_\varepsilon = c_{\varepsilon,1} + c_{\varepsilon,2} \frac{\lambda}{\Delta}. \quad (2.34)$$

Now all parameters of the subfilter-scale parameterization of DALES are defined; they are summarized in table 2.1.

Filling the closure relations and parameters into equation 2.21, we get, after division by $2\tilde{e}^{-1/2}$:

$$\begin{aligned} \frac{\partial \tilde{e}^{-1/2}}{\partial t} &= -\tilde{u}_j \frac{\partial \tilde{e}^{-1/2}}{\partial x_j} + \frac{1}{2\tilde{e}^{-1/2}} \left[K_m \left(\frac{\partial \tilde{u}_j}{\partial x_i} + \frac{\partial \tilde{u}_i}{\partial x_j} \right) \frac{\partial \tilde{u}_i}{\partial x_j} \right. \\ &\quad \left. + -K_h \frac{g}{\theta_0} \frac{\partial A \tilde{\theta}_l + B \tilde{q}_t}{\partial z} \right] + \frac{\partial}{\partial x_j} \left(2K_m \frac{\partial \tilde{e}^{-1/2}}{\partial x_j} \right) - \frac{c_\varepsilon \tilde{e}}{2\lambda}, \end{aligned} \quad (2.35)$$

which closes the system.

2.4 DISCRETIZATION AND NUMERICAL SCHEME

A Cartesian grid is used, with optional grid stretching in the \hat{z} direction. For clarity, an equidistant grid is assumed in the discussion of the advection scheme. The grid is staggered in space, on an Arakawa C-grid; the pressure, the SFS-TKE and the scalars are defined at $\vec{x} + \frac{1}{2}(\Delta x, \Delta y, \Delta z)$, the \tilde{u} is defined at $\vec{x} + \frac{1}{2}(0, \Delta y, \Delta z)$, and similar for \tilde{v} and \tilde{w} .

Time integration is done by a third order Runge-Kutta scheme following Wicker and Skamarock (2002). With $f^n(\phi^n)$ the right-hand side of the appropriate equation

of equations 2.13-2.15 for variable $\phi = \{\tilde{u}, \tilde{v}, \tilde{w}, \tilde{\theta}_i, \tilde{q}_i\}$, ϕ^{n+1} at $t + \Delta t$ is calculated in three steps:

$$\begin{aligned}\phi^* &= \phi^n + \frac{\Delta t}{3} f^n(\phi^n) \\ \phi^{**} &= \phi^n + \frac{\Delta t}{2} f^*(\phi^*) \\ \phi^{n+1} &= \phi^n + \Delta t f^{**}(\phi^{**}),\end{aligned}\tag{2.36}$$

with the asterisks denoting intermediate time steps.

Depending on the desired properties (like high accuracy or monotonicity), several advection schemes are available. With advection in the \hat{x} direction discretized as

$$\frac{\partial \tilde{u}_i \phi_i}{\partial x} = \frac{F_{i+\frac{1}{2}} - F_{i-\frac{1}{2}}}{\Delta x},\tag{2.37}$$

with $F_{i-\frac{1}{2}}$ is the convective flux of variable ϕ through the $i - \frac{1}{2}$ plane. Since we are using a staggered grid, the velocity is available at $i - \frac{1}{2}$ without interpolation. Second order central differencing can be used for variables where neither very high accuracy nor strict monotonicity is necessary:

$$F_{i-\frac{1}{2}}^{2nd} = \tilde{u}_{i-\frac{1}{2}} \frac{\phi_i + \phi_{i-1}}{2},\tag{2.38}$$

A higher-order accuracy in the calculation of the advection is reached with a sixth order central differencing scheme (see Wicker and Skamarock, 2002):

$$\begin{aligned}F_{i-\frac{1}{2}}^{6th} &= \frac{\tilde{u}_{i-\frac{1}{2}}}{60} [37(\phi_i + \phi_{i-1}) \\ &\quad - 8(\phi_{i+1} + \phi_{i-2}) + (\phi_{i+2} + \phi_{i-3})].\end{aligned}\tag{2.39}$$

By adding a small dissipative term to $F_{i-\frac{1}{2}}^{6th}$, a fifth order scheme is created that is nearly monotone:

$$\begin{aligned}F_{i-\frac{1}{2}}^{5th} &= F_{i-\frac{1}{2}}^{6th} - \left| \frac{\tilde{u}_{i-\frac{1}{2}}}{60} \right| [10(\phi_i + \phi_{i-1}) \\ &\quad - 5(\phi_{i+1} + \phi_{i-2}) + (\phi_{i+2} + \phi_{i-3})].\end{aligned}\tag{2.40}$$

For advection of scalars that need to be strictly monotone (for example chemically reacting scalars) the κ scheme (Hundsdoerfer et al., 1995) has been implemented:

$$F_{i-\frac{1}{2}}^\kappa = \tilde{u}_{i-\frac{1}{2}} \left[\phi_{i-1} + \frac{1}{2} \kappa_{i-\frac{1}{2}} (\phi_{i-1} - \phi_{i-2}) \right],\tag{2.41}$$

in case $\tilde{u} > 0$. $\kappa_{i-1/2}$ serves as a switch between higher order advection and first order upwind in case of strong upwind gradients of ϕ . This makes the scheme monotone, but also rather dissipative.

2.5 CONDENSATION SCHEME

The condensation scheme is used to calculate the liquid water content \tilde{q}_l from pressure, temperature and total water content. In the model, it is assumed that there is no liquid water present in an unsaturated grid box, while all moisture above saturation value \tilde{q}_s is liquid water:

$$\tilde{q}_l = \begin{cases} \tilde{q}_t - \tilde{q}_s & \text{if } \tilde{q}_t > \tilde{q}_s \\ 0 & \text{otherwise.} \end{cases} \quad (2.42)$$

To calculate $\tilde{q}_s \equiv \tilde{q}_s(\tilde{T}, p)$, an implicit equation needs to be solved, because \tilde{T} is not directly available. However, \tilde{T} can be approximated with help of the liquid water temperature \tilde{T}_l , which is equal to:

$$\tilde{T}_l = \Pi\theta_l, \quad (2.43)$$

Following Sommeria and Deardorff (1977), $\tilde{q}_s(\tilde{T}, p)$ can be found through a Taylor expansion around $\tilde{q}_{sl} \equiv \tilde{q}_s(\tilde{T}_l, p)$:

$$\tilde{q}_s(\tilde{T}, p) = \tilde{q}_s(\tilde{T}_l, p) + \left. \frac{\partial \tilde{q}_s}{\partial T} \right|_{\tilde{T}=\tilde{T}_l} (\Delta\tilde{T}^2), \quad (2.44)$$

and the higher order terms can be neglected. For ideal gases, the saturation specific humidity can be expressed in the saturation vapor pressure as:

$$\tilde{q}_{sl} = \frac{R_d}{R_v} \frac{e_s}{p - (1 - \frac{R_d}{R_v})e_s}. \quad (2.45)$$

By convention, e_s is used to denote the saturation vapor pressure; note however, that e_s is not related to the SFS-TKE \tilde{e} as defined in sections 2.3. The Clausius-Clapeyron relation relates e_s to the temperature:

$$\frac{de_s}{dT} = \frac{Le_s}{R_v T^2}, \quad (2.46)$$

with $R_v = 461.53 \text{ J kg}^{-1} \text{ K}^{-1}$ denoting the gas constant for water vapor. It can be solved in very good approximation as:

$$e_s(\tilde{T}_l) = e_{s0} \exp \left[a \frac{\tilde{T}_l - T_{trip}}{\tilde{T}_l - b} \right], \quad (2.47)$$

with constants $e_{s0} = 610.78 \text{ Pa}$, $T_{trip} = 273.16 \text{ K}$, $a = 17.27$ and $b = 35.86$. After having substituted in equations 2.45-2.47 into the truncated Taylor expansion equation 2.44 we obtain for the saturated specific humidity:

$$\tilde{q}_s = \tilde{q}_{sl} \left(1 + \frac{L^2}{R_v c_{p,d} \tilde{T}_l^2} \tilde{q}_t \right) \left(1 + \frac{L^2}{R_v c_{p,d} \tilde{T}_l^2} \tilde{q}_{sl} \right), \quad (2.48)$$

and finally the liquid water content can be calculated with equation 2.42. If necessary, the procedure can be applied iteratively to obtain increased accuracy.

2.6 BOUNDARY CONDITIONS

The computational domain has periodic boundary conditions in the horizontal directions. At the top of the domain, we take:

$$\frac{\partial \tilde{u}}{\partial z} = \frac{\partial \tilde{v}}{\partial z} = 0; \quad \tilde{w} = 0; \quad \frac{\partial \tilde{\theta}_l}{\partial z} = \text{constant}; \quad \frac{\partial \tilde{q}_t}{\partial z} = \text{constant}. \quad (2.49)$$

Horizontal fluctuations at the top of the domain (for instance gravity waves) are damped out by a sponge layer through an additional forcing/source term:

$$F_{\text{sp}} = -\frac{1}{\tau_r} (\bar{\phi}(z) - \phi), \quad (2.50)$$

with $\bar{\phi}$ the slab average value of quantity ϕ , and τ_r a relaxation time scale that goes from $\tau_0 = 2.75 \times 10^{-3}$ s at the top of the domain to infinity at the bottom of the sponge layer.

At the surface, velocities are equal to zero, and either the surface values of $\tilde{\theta}_l$ and \tilde{q}_t are prescribed or their subfilter-scale fluxes. Monin-Obukhov similarity theory is used to calculate the remainder of the surface conditions (see for example Garratt, 1992). For the simulations discussed in this thesis, only flux boundary conditions are used, unless the case description specifically prescribes the boundary conditions.

2.7 SENSITIVITY TO NUMERICAL ISSUES

To illustrate the significance of a careful choice of numerical grid, of SFS parameterization and of numerical scheme, a short comparison can be performed. As has already been suggested by the shape of the SFS length-scale correction in equation 2.32, a large sensitivity of the results to the details of the formulation can be expected near sharp gradients.

Therefore, we used the DYCOMS2 (Ackerman et al., 2008, Dynamics and Chemistry Of Marine Stratocumulus experiment) RFO2 intercomparison of a stratocumulus-topped boundary layer with a strong inversion (10 K across a grid cell) was simulated. In stratocumulus cases like DYCOMS2, the cloud top is cooled due to radiation. This sharpens the inversion jump, and drives the convection through the ABL. Such sharp inversions cannot be resolved by the LES mesh anymore, meaning that they must be modeled by the SFS scheme; the production scales are then unresolved. This is in contradiction with the LES philosophy in the strict sense, and the details of the SFS scheme do matter in such cases at the inversion. Therefore, most LES models have difficulties to handle such steep inversions. This can be illustrated by, for instance, the time-dependent liquid water path (LWP, the vertically integrated liquid water content) as depicted in figure 2.1. In observations, the LWP is constant (the dash-dotted lines denote the measurement range), but the median LWP calculated over 11 LES models (white line) decreases steadily. The black line

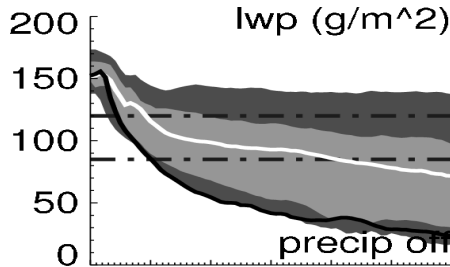


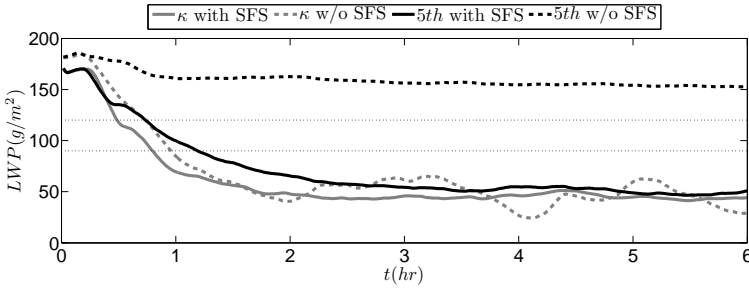
Figure 2.1: The liquid water path in DYCOMS2 with the leap-frog time integration and the κ advection scheme (black line). The dashed-dotted lines signify the range of observed values; the white line is the median over an ensemble of 11 different LES models. Light areas denote central half of the ensemble as delimited by inner and outer quartiles, and dark areas denote ensemble range. From Ackerman et al. (2008).

depicts DALES with the second order leap-frog time integration scheme, and the monotonous third order κ advection scheme (Hundsdoerfer et al., 1995). This advection scheme is designed to correct for erroneous overshoots in the calculation of sharp gradients, by switching to a, diffusive, first order upwind scheme near such gradients. However, for these settings, the cloud layer is completely dissolved.

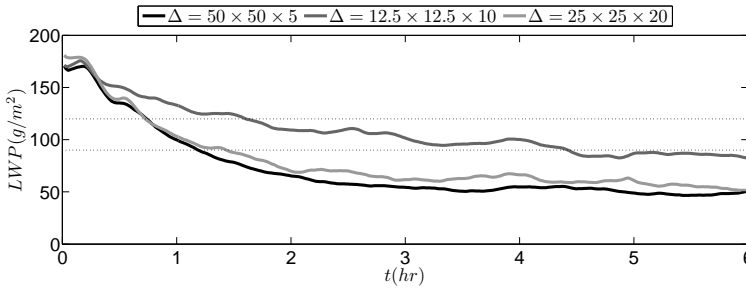
The decrease in liquid water path and the eventual break up of the cloud layer was caused by too much (subfilter-scale) entrainment at the cloud top. A layer of stratocumulus is very sensitive to this, since dry, warm air from above the cloud top is then mixed into the cloud. The entrainment of dry air causes evaporative cooling, which in its turn increases the mixing between the cloud top and the entire layer below. Since entrainment over the cloud-top inversion is a small-scale process, this should be controlled in LES by setting of the SFS parameters as shown in table 2.1. In this case, however, no sensitivity to variations in the SFS parameters could be found. Apparently, it was not necessarily the SFS scheme itself that caused a too strong entrainment.

The solid gray line in figure 2.2(a) shows the liquid water path again, still using the κ advection scheme, but now using third order Runge-Kutta for time integration. The LWP shows enough improvement to lie within the inner quartile of the intercomparison, but is still much lower than observational results. Switching off the SFS diffusion does not yield better results; apparently, the advection scheme is diffusive enough to take over the role of the SFS scheme. When doing the same simulation with 5th order advection (black lines), the picture is somewhat different; although the improvement in a simulation with the default SFS scheme is clearly insufficient, at least the entrainment appears to be depending on the SFS scheme now, and improvements of the scheme can become effective.

Departure from the standard resolution as prescribed by the intercomparison



(a) The liquid water path for DYCOMS2 with $\Delta = 50 \times 50 \times 5\text{m}$, using the κ (gray lines) and the 5th order advection scheme (black lines); with (full lines) and without (dashed lines) SFS diffusion.



(b) The liquid water path for DYCOMS2 using the 5th order advection scheme for various resolutions.

Figure 2.2: The behavior of the liquid water path of DYCOMS2 for various parameters in DALES. Dotted lines delimit the observed values.

also yields improvements. The original aspect ratio of a grid cell was much smaller than 1 ($\Delta z/\Delta x = 5\text{m}/50\text{m} = 0.1$, and the length-scale formulation of the SFS scheme gives more mixing in such situations. As can be seen in figure 2.2(b), a coarser grid with better aspect ratio (dark gray line; $\Delta x = 12.5\text{m}, \Delta z = 10\text{m}$) can give results that are close to the observed values for similar computational cost. At a resolution of $\Delta x = 25\text{m}, \Delta z = 20\text{m}$, the length scale $\lambda = (\Delta x \Delta y \Delta z)^{1/3}$ equals to λ of the intercomparison set up, and the liquid water path is comparable or slightly better, but at much less computational cost, which is similar to the results of van Zanten (2000).

Further research has to reveal how different combinations of resolution, numerical schemes and parameter settings affect the dynamics of the stratocumulus field, not only in the LWP, but also, for instance, in the coupling of the cloud layer and the sub-cloud layer.

2.8 LAGRANGIAN PARTICLE ADVECTION

While the Eulerian formulation of the LES encourages a Eulerian frame of reference for statistics, many problems would be more easily solved from a Lagrangian point of view. This holds in particular for studies of entrainment and detrainment, since these problems can often be stated as a study on the past and the future of a parcel of in-cloud air. To that end, van Dijk (2007) has implemented the Lagrangian Particle Dispersion Model (LPDM) into DALES that has been used extensively in chapter 5. Within this module, massless particles move along with the flow. Since each of the particles is uniquely identifiable, the origins and headings of the particles (and of the air) can be captured.

The position of a particle \vec{x}_p is determined using:

$$\frac{dx_{i,p}}{dt} = \tilde{u}_i(\vec{x}_p; t) + u'_i(\vec{x}_p; t), \quad (2.51)$$

where \tilde{u} is the LES-resolved velocity linearly interpolated to the particle position, and \vec{u}' is an additional random term that represents the SFS-velocity contribution. This term is especially important in regions where the SFS-TKE is relatively large, such as near the surface or in the inversion zone. The calculation of \vec{u}' follows Weil et al. (2004), and was tailored for use in LES with TKE-closure. It was implemented in DALES as follows:

$$du'_i = -\frac{3f_s C_0 \epsilon u'_i}{4\tilde{\epsilon}} dt + \frac{1}{2} \left(\frac{u'_i}{\tilde{\epsilon}} \frac{d\tilde{\epsilon}}{dt} + \frac{2}{3} \frac{\partial \tilde{\epsilon}}{\partial x_i} \right) dt + (f_s C_0 \epsilon)^{1/2} d\zeta_i. \quad (2.52)$$

C_0 is the Langevin-model constant (Thomson, 1987) and has been set to 6; f_s is the slab-averaged ratio between SFS-TKE and total TKE. $d\zeta$ is a Gaussian noise to mimic the velocity field associated with the subfilter turbulence.

Boundary conditions are periodic in the horizontal directions, and emulate the LES boundary conditions at the top and bottom of the domain. Particles are reflected (w_p changes sign) after having hit the top or bottom. Due to historical reasons, second order Adams-Bashforth is currently used for time integration. Tests in the previous version of DALES (that was based on a leap-frog time integration scheme) did not show a significant dependency on the choice of the time integration scheme. The LPDM has already been validated by Weil et al. (2004) for the dry CBL; accuracy in the cumulus topped boundary layer is discussed in section 5.A. There it is shown that in the bulk of the CBL (which is the region of interest here) the particles follow the flow very well.

CHAPTER 3: SUBSIDING SHELLS AROUND SHALLOW CUMULUS CLOUDS

In this study large-eddy simulations are used to gain more knowledge on the shell of subsiding air that is frequently observed around cumulus clouds. First, a detailed comparison between observational and numerical results is presented to better validate LES as a tool for studies of microscale phenomena. It is found that horizontal cloud profiles of vertical velocity, humidity and temperature are in good agreement with observations. They show features similar to the observations, including the presence of the shell of descending air around the cloud. Second, the availability of the complete 3D dataset in LES has been exploited to examine the role of lateral mixing in the exchange of cloud and environmental air. The origin of the subsiding shell is examined by analyzing the individual terms of the vertical momentum equation. Buoyancy is found to be the driving force for this shell, and it is counteracted by the pressure gradient force. This shows that evaporative cooling at the cloud edge, induced by lateral mixing of cloudy and environmental air, is the responsible mechanism behind the descending shell. For all clouds, and especially the smaller ones, the negative mass flux generated by the subsiding shell is significant. This suggests an important role for lateral mixing throughout the entire cloud layer. The role of the shell in these processes is further explored and described in a conceptual three-layer model of the cloud.

Look at those clouds
What's about to come down

HOSPITAL BOMBERS

3.1 INTRODUCTION

The properties of shallow cumulus clouds have long been a much-studied topic in the research of atmospheric boundary layers. One important ongoing issue is the interaction between cloud and environment, despite the fact that it has been an open topic for more than half a century. Stommel (1947) based his cloud model on the concept of a lateral entraining plume, but Squires (1958b) argued that cloud-top mixing and resulting penetrative downdrafts were better able to predict the behavior of cumulus clouds. Asai and Kasahara (1967) emphasized the role of environmental subsidence in compensation of the in-cloud updrafts. Paluch (1979), and after her, for example, Betts (1982), Jensen et al. (1985), Reuter and Yau (1987b) and Jonas (1990) showed conserved variable diagrams of observations indicating that in-cloud air originates from either the subcloud layer or regions at or above

cloud top. On the other hand, Blyth et al. (1988) and Taylor and Baker (1991) for instance saw lateral mixing as dominating mechanism, modeling the cloud using a buoyancy sorting mechanism. Blyth (1993) pressed the significance of a recirculating crown topping the cloud to be the cause of an increase in source level in the highest part of the cloud. Currently, many operational parameterizations are based on a mass-flux approach which is based on a laterally mixing cloud field (see, e.g., Siebesma and Cuijpers, 1995; Siebesma and Holtslag, 1996).

Apart from observational data, large-eddy simulations (LES) are very useful for research in this field, as they provide sufficient statistics and full information on the three-dimensional flow. However, detailed comparisons between LES and observations remain desirable. Usually (e.g., Siebesma et al., 2003; Stevens et al., 2001; Neggers et al., 2003a) only slab-averaged fields and derived quantities are compared with observations. This paper attempts to take the validation of LES a step further by comparing the simulations with the observation by Rodts et al. (2003, hereafter RDJ03). In that study, detailed lateral profiles of the main (thermo-)dynamic variables, conditionally averaged over clouds and surroundings are taken. To obtain optimal comparison, the numerical results are processed in the same way as the observational data, enabling a direct and fair comparison.

The main focus of this paper lies at the shell of subsiding air found at the edge of the cloud as reported by, for example, Jonas (1990, hereafter J90) and RDJ03. This shell is also visible in results of, for example, Austin et al. (1985) and Zhao and Austin (2005a), although the possible role of the shell in cloud physics is not explicitly discussed in these papers. Recently Siebert et al. (2006) observed that in the subsiding shell turbulence is much stronger than in either the cloud core or in the environment. This effect is due to enhanced shear in the shell and might cause a more homogeneous mixing at cloud edge, thus altering droplet spectra.

From the point of view of cloud dynamics the significance of the shell lies in the fact that it is a part of the cloud cell transporting air downwards (like penetrative downdrafts do), but is located at the edge of the cloud, thus closely related to lateral mixing. The mechanism behind the shell can be explained by both cloud-top mixing and by lateral mixing. If the influence of lateral mixing is negligible within this shell, as Reuter and Yau (1987a) and J90 suggested, the shell has to be driven by mechanical forcing through the pressure-gradient force. RDJ03, on the other hand, advocated that lateral mixing over the cloud edge causes evaporative cooling. This in its turn results in negatively buoyant air and descending motion alongside the cloud. Unfortunately, because of the lack of sufficient observational data neither study could be conclusive on this subject. Not only did obtaining statistically reliable results prove to be difficult, moreover some necessary information on the possible forces behind the shell, and in particular the pressure gradient, was unavailable. As demonstrated by, for example, Siebesma and Jonker (2000) on subjects similar to this problem, the controllable environment of LES can provide a well-suited tool to study this subsiding shell. It enables the possibility to extract complete three-dimensional fields of all variables and ensemble averaging over many statistically independent simulations can ensure reliable statistics.

Thus, this paper aims to find conclusive evidence for the governing mechanisms behind the descending shell. To this end, in section 3.3 observations and LES are compared to validate the use of LES on detailed cloud dynamics. Next, the individual terms of the vertical momentum equation are analyzed to find the mechanism driving the shell in section 3.4. Hereafter, the occurrence of the shell in other numerical cases is discussed, along with various properties of the shell (section 3.5), including the relevance of the shell to the dynamics of the cloud and the cloud layer. A connection will be made here with the off-center position of the cloud core as seen by Heymsfield et al. (1978) and the ‘humidity halos’ that are found by, for example, Perry and Hobbs (1996), Lu et al. (2003) and Laird (2005) and adjoin clouds. These halos are shown to be caused by lateral mixing and yield an increase in humidity of the environmental air especially at the downshear side of the cloud. Since halos are placed in the conditionally stable environmental air, they tend to remain for a relatively long time. This may result in more favorable conditions for growth of subsequent clouds, as suggested by Telford and Wagner (1980) or Kuang and Bretherton (2006).

The discussion finally leads to the development of a simple conceptual model of the cloud, the cloud edge and the environment in section 3.6. Within this model, the role of the shell in the interaction between cloud and surroundings can be isolated from other processes and can be explored in detail.

3.2 DESCRIPTION OF THE LARGE-EDDY SIMULATIONS

3.2.1 Case description

All simulations were performed with a parallelized version of the Dutch Atmospheric LES (DALES) model of which the details are described by Cuijpers and Duynkerke (1993). For reasons discussed below, two idealized cases are studied here. First is the case designed by Neggers et al. (2003a) based on the Small Cumulus Microphysics Study (SCMS) observations. Second is the case by Siebesma et al. (2003) of the Barbados Oceanographic and Meteorological EXperiment (BOMEX, Holland and Rasmusson, 1973).

Neggers et al. (2003a) modeled their numerical case on measurements done on August 5th 1995 above Florida (see Knight and Miller (1998) or French et al. (1999) for details), This day was part of a period where non-precipitating shallow cumuli developed every day, and large scale forcings were constant and small compared with the surface fluxes. The case is designed to run from sunrise (1200 UTC) till sunset at 2400 UTC. Sensible and latent surface heat fluxes are sinusoidally shaped with a maximum of 100 W m^{-2} and 300 W m^{-2} , respectively at 1800 UTC. This results in a Bowen ratio r_B of 0.3. Cloud base is located around 700 m and cloud top at 2200 m. The system is subject to a mean wind of $(-4, 4) \text{ m s}^{-1}$ related to a sea-breeze and a mean shear of approximately $(0, 0.7) \text{ m s}^{-1} \text{ km}^{-1}$. To follow the cloud field being advected by this wind, a Galilean-transform of $\vec{U}_T = (-4, 4) \text{ m s}^{-1}$ was imposed. Simulations were carried out on a domain of $6.4 \text{ km} \times 6.4 \text{ km} \times 5.12 \text{ km}$

with each grid box of a size of $\Delta x = \Delta y = 50$ m, $\Delta z = 40$ m and a timestep of $\Delta t = 0.5$ s. For this study, data between 1800 UTC and 2200 UTC were used, coinciding with the times of measurement flight RF12 during the SCMS campaign. To enhance statistics five simulations were carried out. All simulations are identical save for a random perturbation of the initial temperature and humidity field. This creates statistically identical but independent runs (see Chlond and Wolkau, 2000).

The BOMEX case is describe by Siebesma et al. (2003). Sensible and latent surface heat fluxes amount to 8 W m^{-2} and 150 W m^{-2} , respectively (yielding $r_B = 0.05$). Cloud base is located around 600 m and cloud top at 1700 m, meaning that clouds are also somewhat smaller than in SCMS. The mean geostrophic wind is set to $(-10 + z/555, 0) \text{ m s}^{-1}$, resulting in a shear of approximately $1.8 \text{ m s}^{-1} \text{ km}^{-1}$. Again, a Galilean-transform is performed (this time, $\vec{U}_T = (-8, 0) \text{ m s}^{-1}$) to follow the cloud field. Ten simulations with different random initialization are carried out on a domain of $6.4 \text{ km} \times 6.4 \text{ km} \times 3.2 \text{ km}$, a grid box of $\Delta x = \Delta y = 25$ m, $\Delta z = 20$ m and a timestep of $\Delta t = 1$ s. From each simulation the first 3 h hours are discarded as spin-up.

While the work by RDJ03 on the SCMS case allows for a detailed comparison with those observations, it is interesting to see how dynamics of SCMS clouds compare with simulations of marine boundary layer of BOMEX. Especially for processes driven by phase changes like evaporative cooling, the more humid environment and lower Bowen ratio of BOMEX could very well result in different dynamics.

Moreover, according to Heymsfield et al. (1978) and Perry and Hobbs (1996) the enhanced vertical shear in BOMEX is important for processes associated with lateral mixing, and may be so here as well. BOMEX has also the practical advantage of a lack of diurnal cycle. This makes longer runs possible and ensures a statistically identical cloud field over the entire run. This results in enhanced statistics and enables exploration of for example the shell as a function of cloud size.

3.2.2 Method of postprocessing

The study of RDJ03 was based on flights RF12, RF13, RF16 and RF17 of the SCMS database, held on 5, 6, 10 and 11 August 1995. Their analysis consisted of a conditional sampling of all transects through clouds larger than $L_c = 500$ m, normalized to unit length. After a correction for observation height, averages were taken of observational quantities (the vertical velocity w , the liquid potential temperature θ_l and the total water content q_t) over all transects. In averaging, the average value of the environment before entering the cloud has been subtracted from the sample.

For comparison between LES and observations, the sampling procedure in LES is modeled closely to the method of RDJ03. Virtual flights are taken through the LES domain and points are sampled within a cloud or within one cloud length distance from both sides of the cloud. These flights are usually taken at fixed height, typically 1000 m above the surface. The average value of the region before the cloud was subtracted from all the values, and the results are averaged over all clouds.

A slight alteration of RDJ03 was needed to fit the method on the LES grid. Firstly, flights through clouds were only taken along LES grid lines in west-east and north-south direction and vice versa. Secondly, only transects of exactly 400 m were taken into account to avoid the need of rebinning, since that could smooth out much of the signal. The slight reduction in size to $L_c = 400$ m (compared to the 500 m in RDJ03) ensured that enough clouds exist for reliable statistics. While in observations the pilot attempted to fly through the center of active clouds, the trajectories were rather wide, resulting in inclusion of other transects through clouds. This allows for good comparison with the simulations where transects could be either through the center of a 400 m sized cloud or through the size of a much bigger cloud.

If on a certain line of measurement one of the environmental points happens to fall inside another cloud, this entire line is discarded from the analysis, to avoid pollution of the statistics. Data within one grid point distance of the cloud top or bottom are discarded, to avoid biases due to averaging over the vertical border of the cloud.

3.3 COMPARISON WITH OBSERVATIONS

For the validation of the numerical work, the fly-through profiles of w , q_t and θ_l are compared with RDJ03. In figure 3.1, these results are plotted. The left column are LES simulations, the middle column are the RDJ03 results of averaging over all flights, and the results of individual flight days in RDJ03 are shown in the right column. On top of the average profiles the rms deviations are plotted for the LES and the average RDJ03 results. These deviations do not represent the error in the means, but rather a measure for the variability between different clouds. The corresponding graphs in figure 3.1 appear to match as well as can be expected; the average numerical result lies well within the natural variation of the observations.

However, it should be noted that both the values of q_t and θ_l as well as the variation around the mean profiles is slightly smaller in LES than in the averaged observations. Several explanations can be given for this; first, the simulations are based on the measurements on August 5th, the day of flight RF12, represented in figure 3.1(right) by the dotted line. This flight resulted in below-average differences in liquid water potential temperature and total humidity. The fact that LES did not sample over the varying conditions of the various flight days, also explains the smaller fluctuations. Secondly, since in LES only clouds of one fixed size are taken into account, it can be expected that the variation between different transects is also less.

The size of the subsiding shell, while still visible in the w profile in LES, is less pronounced than in observations. This can be attributed to the filtering procedure that underpins the LES methodology. An LES grid box value represents an average over the size of the grid box (25 m), while observations were done with a spatial sampling rate of $(10 \text{ m})^{-1}$. It is therefore likely that LES smoothes out more of the shell than observations do. Finally, in observations an asymmetry can be seen that is

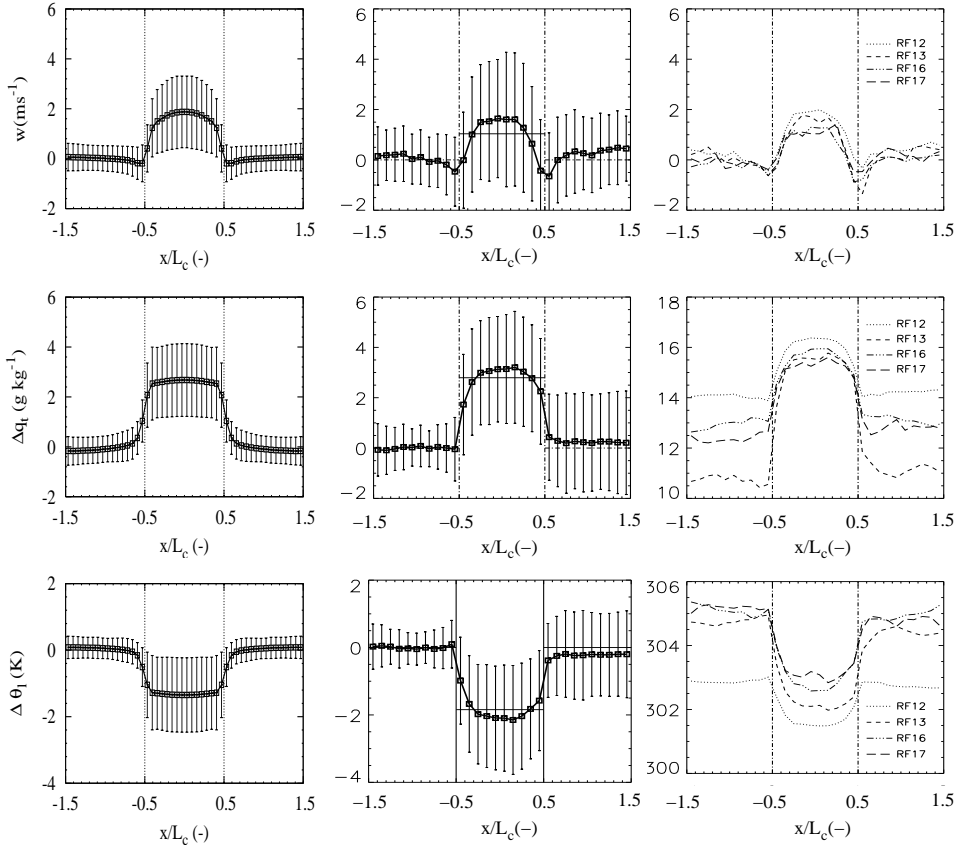


Figure 3.1: Averaged in-cloud profiles of vertical velocity, total water content, and liquid water potential temperature of (left) the LES, (middle) the average over all flights by RDJ03 and (right) the individual flights by RDJ03. For the left and middle columns, the mean value left of the cloud is subtracted. The cloud is centered at zero and scaled with cloud size L_c . The bars denote the root mean square values of the individual measurements; these bars thus do not denote an error, but are a measure of variance between the various clouds. Horizontal lines in the middle column denote the environmental and in-cloud averages. For the observations, clouds of at least $500m$ are taken into account; in the simulations, transects are taken at $1000m$ height and only $400m$ sized clouds are presented.

not visible in LES, due to the fact that in LES transects are taken from all sides. The origin of such asymmetries is discussed in section 3.5.3. Overall, the most striking features of the observations, such as the cloud edge minimum in the w profile, are clearly present and similarly sized in the simulations. LES thus seems to be a valid tool to study the origin of the subsiding shell.

3.4 INVESTIGATION OF THE TERMS OF THE VERTICAL MOMENTUM EQUATION

In figure 3.1 the shell of descending air was clearly visible in both the observational data and in the LES results. To investigate the cause of this shell, we can benefit from the additional information gained from the simulations, such as the individual terms of the vertical momentum equation. Neglecting the Coriolis forcing, the vertical momentum equation used in LES can be split into the resolved advection terms (denoted as A), the buoyancy force (B), the vertical pressure gradient (P), and the parameterized unresolved subgrid diffusion (S):

$$\frac{\partial w}{\partial t} = \underbrace{-u_j \frac{\partial w}{\partial x_j}}_A + \underbrace{g \frac{\theta_v - \bar{\theta}_v}{\Theta_0}}_B - \underbrace{\frac{1}{\rho_0} \frac{\partial p'}{\partial z}}_P + \underbrace{\frac{\partial}{\partial x_j} \left[K_m \left(\frac{\partial u_j}{\partial z} + \frac{\partial w}{\partial x_j} \right) \right]}_S. \quad (3.1)$$

Here θ_v denotes the virtual potential temperature, $\bar{\theta}_v$ the slab average virtual potential temperature, Θ_0 a reference temperature, ρ_0 a reference density, p' the modified pressure and $K_m(x, y, z)$ the subgrid-scale eddy viscosity.

One or more of these forcings should be responsible for the minimum in the w profile around the cloud edge. If mechanical forcing is the main process behind the subsiding shell, the pressure gradient should be negative at the edge of the cloud. Evaporative cooling induced by horizontal mixing over the cloud edge, on the other hand, would result in a negative buoyancy force in the shell. The four terms are plotted in figure 3.2 as a function of the normalized distance to the center of the cloud x/L_c .

In these figures a strong minimum in buoyancy (upper-left graph) that appears just around the cloud is counteracted by the other terms. This means that buoyancy (and thus evaporative cooling) seems to drive the descending shell. This is in agreement with the findings of RDJ03, although they could not be conclusive with regard to the role of the other terms, in particular the pressure gradient term. Indeed, looking at the upper right graph in figure 3.2, the simulations clearly indicate that the pressure gradient is not causing the shell, but, like the advection and the subgrid diffusion term, counteracts the downward acceleration. This shows unambiguously that the descending shell is driven by negative buoyancy, resulting from evaporative cooling following lateral mixing of environmental air with cloudy air.

It should be noted here that the terms A , B , P and S as shown in of figure 3.2, do not balance. This unbalance is caused by the conditional sampling over clouds

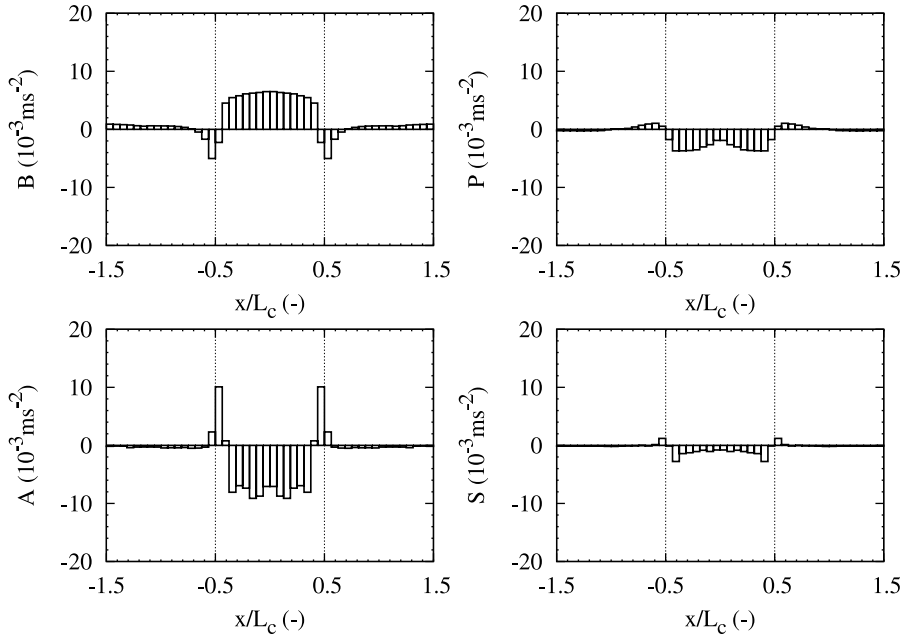


Figure 3.2: The individual terms of the vertical momentum equation 3.1: (top left) buoyancy B , (top right) vertical pressure gradient P , (bottom left) advection A and (bottom right) subgrid diffusion S , plotted against the distance to cloud center x (normalized with cloudsize L_c).

with a fixed size. This follows from the fact that a growing cloud is associated with a positive acceleration. As the cloud keeps growing, however, it does not meet the size criterion of $L_c = 400$ m anymore and leaves the ensemble, thus causing an apparent unbalance in the vertical momentum budget.

3.5 ANALYSIS OF BOMEX

3.5.1 Occurrence of the descending shell in BOMEX

To investigate whether the descending shell is a specific feature of the SCMS case, or rather a more generic feature of shallow cumulus clouds, we analyse the BOMEX numerical case of marine shallow cumulus clouds in the same way as was done for SCMS. Since BOMEX is a steady-state case, a much larger time window for observations could be taken. Ten simulations of 12 h each have been done, of which each first 3 h were disregarded as spin-up. Data of 1021 flights through clouds of $L_c = 400$ m at a measurement height of 1000 m have been collected; the results for w , θ_l , q_t and the vertical momentum terms are presented in figure 3.3. The shapes of the profiles in figure 3.3 resemble the SCMS results, including the existence of

a descending shell in the w profile. Also similar to the SCMS results, the shell is associated with an area of negative buoyancy (with a lateral size of 50 – 100 m), while the pressure gradient is again positive at cloud edge. Overall, this suggests that the descending shell due to evaporative cooling by lateral mixing is a generic feature of shallow cumulus clouds.

It might be noted that the shell looks similar to artifacts due to the advection scheme of the LES. This is discussed in the appendix; the shell appears to be independent of the used advection scheme.

Looking at the location of the velocity minimum in both figure 3.1 and in figure 3.3, the subsiding shell seems to lie at the edge or just outside the cloud (signified by the vertical dashed line in the figures). Indeed, the buoyancy decreases within the cloud from cloud core value to its minimum virtually at the edge, which makes sense since the shell is associated with recently evaporated air.

The existence of these downdrafts and the associated shear also generate additional turbulence at the edge of the cloud. For the BOMEX simulations, the turbulence dissipation rate ϵ is plotted in figure 3.4. Similar to the observational results of Siebert et al. (2006), the shell is much more turbulent than the outer environment, and shows a maximum outside the cloud core. This can be expected, since this is the region of the largest gradients. The increased turbulence should result in a better (more homogeneous) mixing even before air is entrained into the cloud core.

3.5.2 Mass flux through the shell

Looking again at the relatively modest size of the subsiding shell in the w profile in figure 3.3, we may wonder what the importance of the subsiding shell is on the interaction between the cloud and its environment. To illustrate the significance of the shell an instantaneous cross section of a cloud is shown in figure 3.5. Here, vectors denote the in-plane velocity, and the buoyancy excess is depicted in gray tones. Quite consistently, a minimum in buoyancy (the light area in figure 3.5) can be observed not only at cloud top but almost everywhere around cloud edge. Especially around the right side of the cloud the area with negative velocities is large. There, environmental air mixed into the cloud seems to be carried down before entering the cloud.

Moreover, it has to be kept in mind that these ‘fly-through’ profiles are one-dimensional representations. The significance of that becomes clear when looking at the vertical mass flux M for 400-m-sized clouds. On the assumption of a circular-shaped cloud, M would be

$$M(x)dx = \rho w(x)2\pi x dx. \quad (3.2)$$

The contribution to M of the slowly moving air further away from cloud center cannot be neglected compared to the fast moving cloud core, because of the significant area of the outer region. This is shown in figure 3.6: 10% (the black area) of the air flowing upward through the cloud comes down directly through

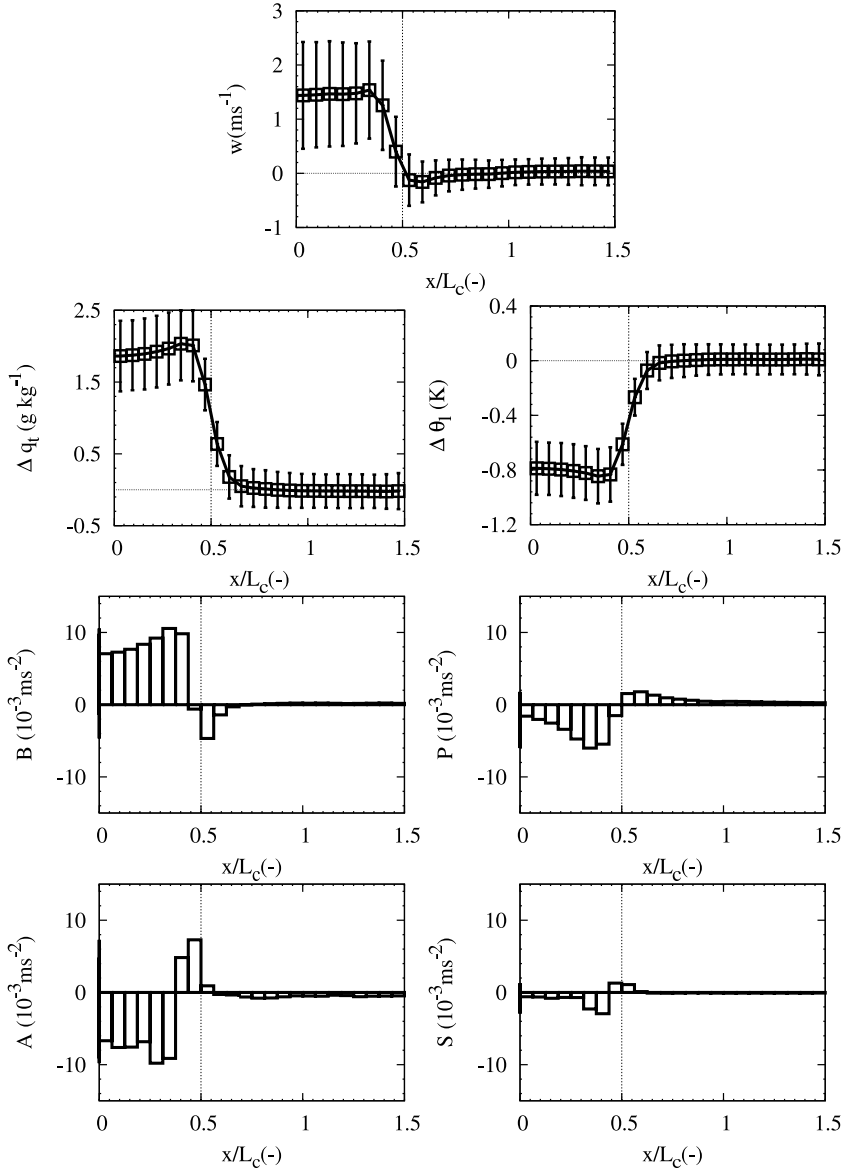


Figure 3.3: BOMEX results: Profiles of vertical velocity, total moisture, and liquid potential temperature and the vertical momentum budget terms (buoyancy, pressure gradient, advection and subgrid diffusion) are plotted, here for 1021 cloud transects of 400m appearing in an ensemble average of 10 BOMEX runs of 12h each. Fly-through level is 1000 m.

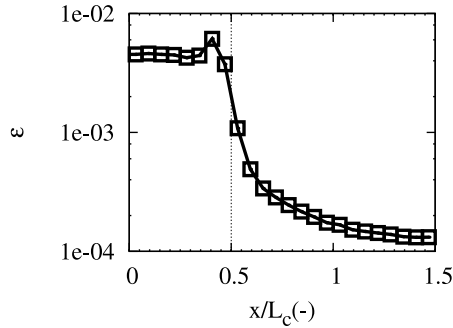


Figure 3.4: The dissipation rate (on a log scale) profiles for BOMEX. For further explanation of the graph, see figure 3.3.

the region where $B < 0$, while another 13% (the dark gray area) is dragged along downwards with the shell, in total balancing almost a quarter of the in-cloud up-flow. In figure 3.7 these effects are shown for various cloud sizes. In the left panel of figure 3.7 the total upward mass flux through the cloud and the total downward mass flux through the shell (defined here as the region of negative velocity directly adjacent to the cloud) is shown. For $L_c = 400$ m the relative mass flux through the shell amounts to about a quarter, a value decreasing with cloud size. In figure 3.7(right) the integrated amount of buoyancy in the cloud and in the shell is shown; here the negative in-shell buoyancy is even dominating the positive in-cloud buoyancy for smaller clouds. The picture that arises here is the following: since the environment has no direct interaction with the warm cloud core, but is fenced off by the shell, the environment actually 'sees' the cloud as a negatively buoyant, often downward moving entity. The significant amount of air dragged downwards might also explain the results of J90. He observed significant amounts of air with properties equal to that of higher environmental levels. Since environmental air is first dragged downwards by the subsiding shell before being mixed into the cloud, we can now see that this downward motion would cause a bias towards mixing at heights above actual mixing height.

The downward mass flux through the shell also has implications for the necessary compensating subsidence of the environment; these issues are addressed in section 3.6.

3.5.3 Influence of mean wind and shear

Exploration of the in-cloud values of the (thermo-) dynamical quantities as well as the vertical momentum budget terms should yield their optimum values in the cloud core. However, when looking in detail at figure 3.3, the profiles appear to be flat within the clouds, with even slightly decreasing values when approaching cloud center. In the SCMS results (figures 3.1 and 3.2) this effect appears to be

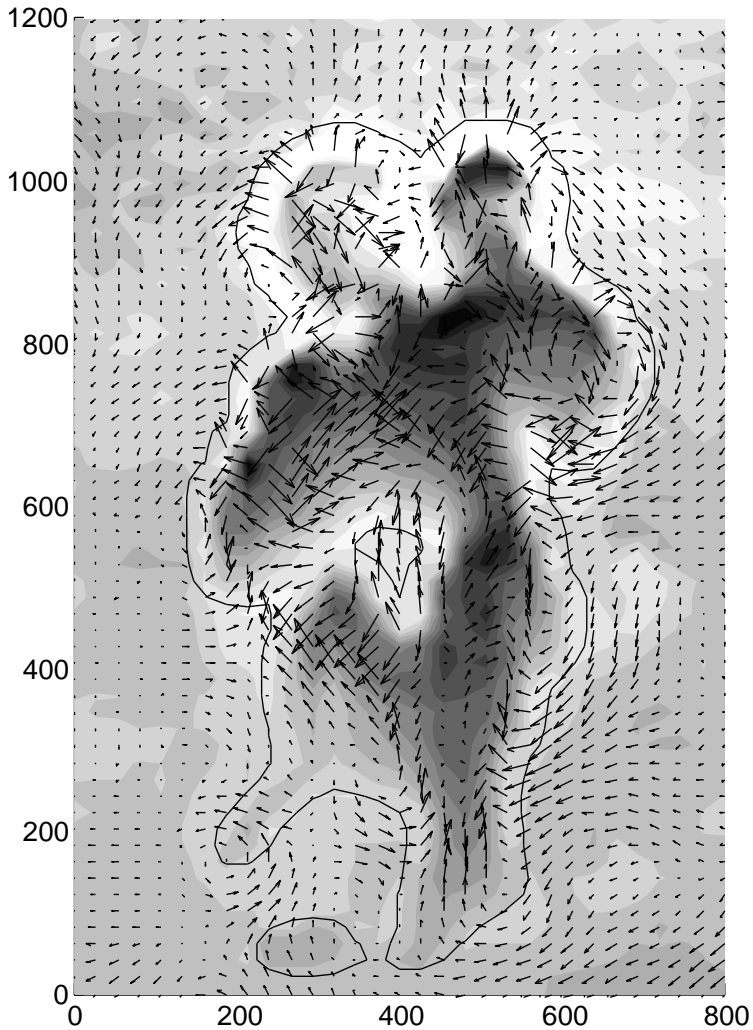


Figure 3.5: An $y - z$ -plane cross-section (with distances in meters) through the center of mass of a cloud. Cloud edge is denoted by the black line, the vectors signify the in-plane velocity and the virtual potential temperature excess is displayed in gray tones, with the lighter areas more negatively buoyant.

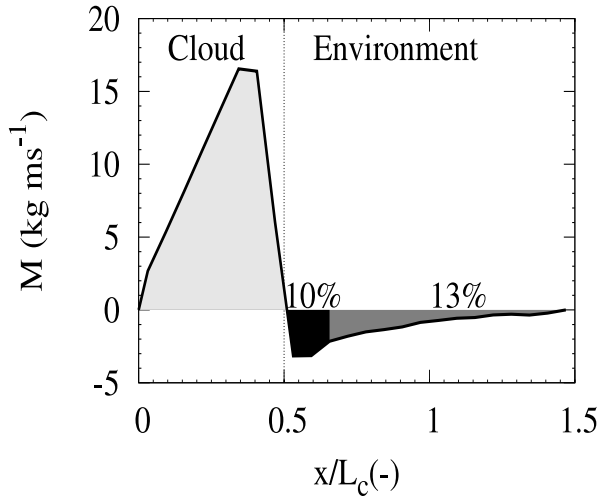


Figure 3.6: The vertical mass flux M through 400–m-sized clouds as a function of the distance to cloud center x for BOMEX at 1000 m height. For small distances, M goes to zero due to small size of the area. The black colored area signifies the mass flux through the negatively buoyant shell (around 10% of the total cloud mass flux). The dark gray area is dragged downwards induced by the shell, resulting in a total of 25% of the in-cloud upflow.

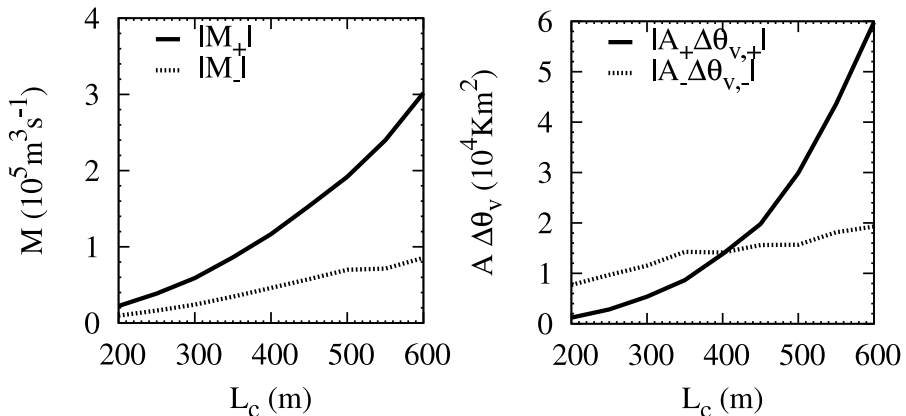


Figure 3.7: The absolute values of the mass flux M (left) and the integrated virtual potential temperature difference $A\Delta\theta_v$ through the cloud core and the shell. The + and – subscripts denote sampling over regions with positive and negative vertical velocity, respectively, and A the area of that region.

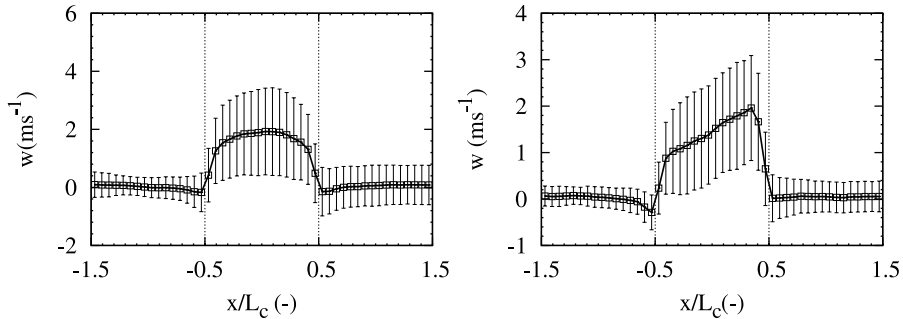


Figure 3.8: The vertical velocity profile for SCMS (left) and BOMEX (right), with all transects taken from west to east.

much less pronounced. Indeed, if only transects through the BOMEX simulations are taken into account when taken from west to east (i.e. against the mean wind), the vertical velocity profile appears to be asymmetrical (see figure 3.8). Of course, adding all east-west transects to figure 3.8, would result in a symmetrical profile again, but for heavily skewed distributions the maximum would be out of cloud center. The other variables (not shown here) show a very similar skewness.

The only component in the system that breaks the lateral symmetry is the mean horizontal wind. For BOMEX this mean wind has a value of approximately $\vec{U} \approx [-10 + (z/555), 0] \text{ m s}^{-1}$ in the cloud layer, which is much stronger than the mean horizontal wind in SCMS [where the geostrophic wind is equal to $(-4, 4) \text{ m s}^{-1}$]. Since measurements are done in the reference frame of the cloud, which advects with the mean wind, this value should have no influence on the cloud vertical velocity profile. However, the vertical mean wind shear [$\partial\vec{u}/\partial z \approx (1.8, 0) \text{ m s}^{-1} \text{ km}^{-1}$ in BOMEX] might: In a strongly sheared environment the cloud core is displaced from the center of the cloud (see Heymsfield et al., 1978). Later studies (for instance by Perry and Hobbs, 1996) found that vertical shear is also often responsible for a halo of humid air up to several cloud radii away from the cloud edge on the downshear side (i.e. the right side of the cloud for positive values of the shear and vice versa). Laird (2005) found a similar increase in clear-air humidity, in a study on the SCMS cloud database, only in a smaller area around the cloud and without much preference for either the up- or downshear side of the cloud. This was blamed on the low amount of shear in the SCMS [being around $\partial\vec{u}/\partial z \approx (0, 0.7) \text{ m s}^{-1} \text{ km}^{-1}$].

Besides a physical explanation of the asymmetry, an argument of numerical nature should also be considered. In nature clouds would be advected by the mean wind with the same horizontal velocity as their environment. Since the statistics are taken in the reference frame of the cloud, mean wind advection in itself should not influence the results. In simulations, however, the discrete representation and all-or-nothing condensation scheme result in an environment moving with the mean wind while the cloud is effectively standing still, except for the instants when con-

Table 3.1: Simulations done to investigate the role of the mean horizontal wind. Based on BOMEX, Galilean transformation U^T and the mean velocity $U(z)$ were varied. $|\partial u/\partial z|$ was kept on the BOMEX-value of $1/555 \text{ s}^{-1}$, and a mean surface velocity was added to ensure $U(z) = \pm 1 \text{ m s}^{-1}$ at the observational level of 1000 m, yielding $U_s = z/555 - 0.836 \text{ m s}^{-1}$.

Name	$U^T (\text{m s}^{-1})$	$U(z) (\text{m s}^{-1})$
GA-2UM-1	-2	$-U_s$
GA-1UM-1	-1	$-U_s$
GAoUM-1	0	$-U_s$
GA-2UMo	-2	0
GAo-1Mo	-1	0
GAoUMo	0	0
GA1UMo	1	0
GA2UMo	2	0
GAoUM1	0	U_s
GA1UM1	1	U_s
GA2UM1	2	U_s

denensation level is reached adjacent to the cloud, moving the cloud into another grid box.

To investigate the effect of this artifact, it is useful to split the advection term A of the vertical momentum equation 3.1 into a large-scale transport by mean-wind (L) and by fluctuations (F) term:

$$A = -u_j \frac{\partial w}{\partial x_j} = \underbrace{-\left(u_j - U_j^T\right) \frac{\partial w}{\partial x_j}}_L \underbrace{-u_j' \frac{\partial w}{\partial x_j}}_F \quad (3.3)$$

The influence of L on the profiles - which should be zero - can be studied by variation of the Galilean transformation velocity U_j^T , thus affecting the effective mean wind $U_j - U_j^T$. To investigate the combined effects of these two (both shear and mean wind advection) mechanisms, a set of cases is designed and described in table 3.1. Based on the strongly sheared BOMEX case, the Coriolis force ignored in these simulations to eliminate the influence of the Ekman spiral. The mean wind is varied in such a way that at the level of measurement (1 km) $U_j - U_j^T$ is either -1 , 0 or $+1 \text{ m s}^{-1}$ and the amount of shear is equal to the BOMEX value of $1.8 \text{ m s}^{-1} \text{ km}^{-1}$. To study the numerical effects, U^T is varied around $U(z = 1000 \text{ m})$ to see the effect of the mean wind advection.

The results of these simulations are plotted in figure 3.9. First of all, looking at the solid lines in the center column (i.e., neither mean wind or shear), it can be seen

that all profiles are symmetrical, indicating that the mean horizontal wind is indeed the cause of the asymmetry seen in figure 3.8. Focussing then on the variation in U^T depicted in the center column of this figure, the effect of the mean wind advection is clearly visible. L peaks sharply at cloud edge, and this is where the buoyancy and velocity profiles are mainly affected. In extreme cases, the subsiding shell is completely filled in on the downwind side of the cloud and the location of the in-cloud velocity maximum is also shifted to the downwind side. The total water content appears less skewed, since the scalar profiles are only indirectly affected by the vertical advection term $w (\partial\phi/\partial z)$.

By comparing the different columns in figure 3.9 the effect of vertical shear can be seen. On the downshear side (the left-hand side in the left column), there is a clear increase in humidity upto a cloud radius away from the edge, while steep gradients are observed at the upshear side of the cloud. Aside from yielding skewed profiles, this also greatly affects the existence of the shell, as is schematically shown in figure 3.10. On the downshear side the region with just evaporated air is increased, causing a wider shell; the lack of mixing and increased upward drag on the upshear side prevents the occurrence of a shell there. The cloud core (signified by maximum velocity, buoyancy and humidity) remains located above cloud base, and its position is thus skewed towards the upshear side.

Looking at the combined effect of both the vertical shear and the mean wind advection, the shear is clearly dominant, since the sheared profiles do not change much when varying U^T . One notable exception should however be made: The mean wind advection is capable of creating a small artificial shell of its own at the upwind, upshear side of the w profile, helped by the sharp gradient of this profile, which originally was created by the shear.

3.6 THREE-LAYER MODEL

To get a better understanding on the role and behavior of the shell, below we develop a simple analytical model within the framework of Asai and Kasahara (1967, hereafter AK67). The AK67 model uses a cylindrical geometry and employs a 'top hat' approach, dividing the cloud layer into two regions, a cloudy region with positive mass flux and around it a much larger environmental region with a small downward velocity, in total exactly compensating the cloud mass flux. We extend this model by adding a third region between cloud and environment, that is, a region for the shell with its own velocity (see figure 3.11). The present model is also a significant simplification of the model by AK67, since we discard the vertical dimension, and assume a steady state. As such the three-layer model is most representative of the middle of the cloud layer. In any case, it is not to be expected that this approach yields a solid quantitative model for the entire cloud layer, yet it may yield a qualitative description of the shell, giving understanding of the consequences of a system driven by buoyancy which experiences significant shear at the edges and therefore lateral mixing of mass and momentum. Specifically, it is of

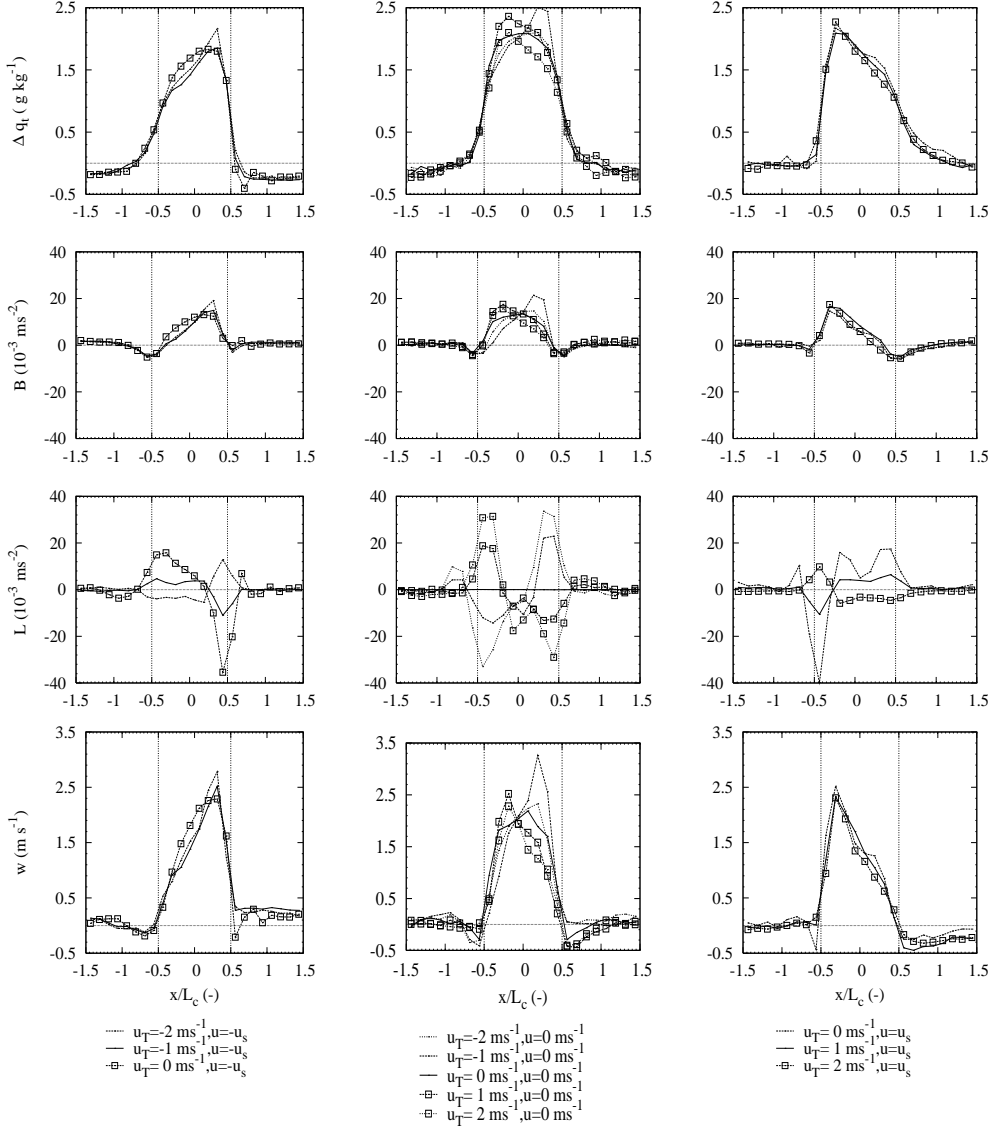


Figure 3.9: The influence of shear (left column) $U(z) = -U_s(z)$, (center) $U_z = 0$, (right column) $U(z) = -U_s(z)$ and the Galilean transform (varied within the graphs on (from top to bottom) the total water content q_t , the buoyancy B , the large-scale horizontal advection L and the vertical velocity w .

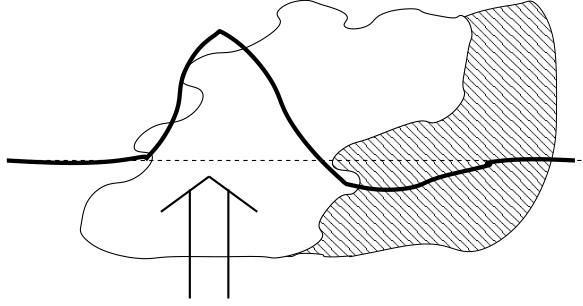


Figure 3.10: The conceptual picture of a cloud tilted due to vertical shear, including its humidity halo (shaded area). The vertical velocity profile is sketched on top of the cloud. Since the cloud core is less skewed than the rest of the cloud, this results in an upshear location of the velocity maximum. The humidity halo ensures a wide and deep subsiding shell on the downshear side of the cloud.

interest to see whether a cloud exists in a realistic way if the cloud dynamics are completely dominated by lateral mixing through the shell.

Assuming rotational symmetry one can rewrite equation 3.1 into

$$\frac{\partial w}{\partial t} = -\frac{1}{r} \frac{\partial}{\partial r}(ruw) - \frac{\partial}{\partial z}(wv) + \frac{g}{\Theta_0}(\theta_v - \bar{\theta}_v) = 0, \quad (3.4)$$

and the continuity equation into

$$\frac{1}{r} \frac{\partial}{\partial r}(ru) + \frac{\partial}{\partial z}(w) = 0. \quad (3.5)$$

Integrating equation 3.5 over the region $n \in \{1, 2, 3\}$ with area $A_n = \pi(r_n^2 - r_{n-1}^2)$, and disregarding vertical gradients as mentioned, after dividing by 2π we get

$$\int_{r_{n-1}}^{r_n} \left[\frac{1}{r} \frac{\partial}{\partial r}(ru_n) \right] r dr = r_n \bar{u}^n - r_{n-1} \bar{u}^{n-1} = 0, \quad (3.6)$$

where \bar{u}^n denotes the average of u over the circle with radius r_n , that is, the boundary between region n and $n+1$. With $r_0 = 0$ this gives $\bar{u}^n = 0$ for all $n > 0$; a direct consequence of the absence of vertical gradients in the flow. Integration of equation 3.4 over area A_n yields

$$2\pi r_n \bar{u} \bar{w}^n - 2\pi r_{n-1} \bar{u} \bar{w}^{n-1} = A_n \frac{g}{\Theta_0} (\Delta \bar{\theta}_v^n) \quad (3.7)$$

with $\Delta \bar{\theta}_v^n = \bar{\theta}_v^n - \bar{\theta}_v$, where $\bar{\theta}_v^n$ denotes the average of θ_v over the area A_n . Decomposing the boundary covariance term into $\bar{u} \bar{w}^n = \bar{u}^n \bar{w}^n + \overline{u' w'^n}$, and using $\bar{u}^n = 0$, we only need to account for the covariance of fluctuations at the boundary, that is, the effect of turbulent mixing at the boundary. Rather than working with the areas

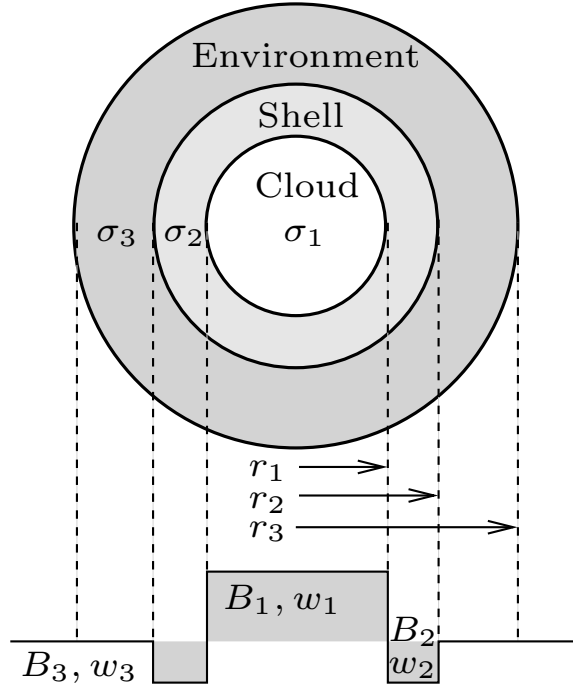


Figure 3.11: The proposed model divides the cloud layer in three shells: in the center the cloud core, with positive vertical velocity and buoyancy; wrapped around the core lies the subsiding shell with negative vertical velocity and buoyancy, and finally an environmental region balancing the other two.

A_n , we will use the relative area coverage $\sigma_n = A_n/(A_1 + A_2 + A_3)$, and use the cloud area as the reference $A_1 = \pi r_1^2$. Substituting $A_n = \pi r_1^2 \sigma_n / \sigma_1$, we obtain

$$\frac{r_1^2}{2} \frac{g \Delta \bar{\theta}_v^{-1}}{\Theta_0} = r_1 \widetilde{u'w'}^1, \quad (3.8)$$

$$\frac{\sigma_2}{\sigma_1} \frac{r_1^2}{2} \frac{g \Delta \bar{\theta}_v^{-2}}{\Theta_0} = -r_1 \widetilde{u'w'}^1 + r_2 \widetilde{u'w'}^2, \quad (3.9)$$

$$\frac{\sigma_3}{\sigma_1} \frac{r_1^2}{2} \frac{g \Delta \bar{\theta}_v^{-3}}{\Theta_0} = -r_2 \widetilde{u'w'}^2, \quad (3.10)$$

while conservation laws dictate

$$\sigma_1 + \sigma_2 + \sigma_3 = 1, \quad (3.11)$$

$$\sigma_1 \bar{w}^1 + \sigma_2 \bar{w}^2 + \sigma_3 \bar{w}^3 = 0, \quad (3.12)$$

$$\sigma_1 \Delta \bar{\theta}_v^{-1} + \sigma_2 \Delta \bar{\theta}_v^{-2} + \sigma_3 \Delta \bar{\theta}_v^{-3} = 0, \quad (3.13)$$

where \bar{w}^n represents the area averaged velocity of region n . Physically, equations 3.8 – 3.10 express that the buoyancy force is counteracted by the turbulent mixing of momentum over the boundaries. By this mechanism a balance is reached, allowing the velocities to reach an equilibrium state. The shell region experiences mixing at both boundaries. Following AK67, we apply Prandtl mixing length theory to the turbulent mixing terms

$$\widetilde{u'w'}^n = -K_n \left. \frac{dw}{dr} \right|_{r=r_n} \rightarrow -K_n \frac{\bar{w}^{n+1} - \bar{w}^n}{\frac{1}{2}(r_{n+1} - r_{n-1})}, \quad (3.14)$$

with for K_n ,

$$K_n = \ell^2 \left| \frac{\bar{w}^{n+1} - \bar{w}^n}{\frac{1}{2}(r_{n+1} - r_{n-1})} \right|. \quad (3.15)$$

For the mixing length ℓ it seems reasonable to assume that the width of the shell is the relevant length scale

$$\ell = \kappa(r_2 - r_1), \quad (3.16)$$

with von Kármán constant $\kappa = 0.4$. We introduce the relative shell size $\zeta = (r_2 - r_1)/r_1$ as a model parameter, and, with $f(w) = w|w|$, rewrite equations 3.8 and 3.9 into

$$\sigma_1 \frac{g \Delta \bar{\theta}_v^{-1}}{\Theta_0} = \frac{8\kappa^2}{r_1} \frac{\sigma_1 \zeta^2}{(1 + \zeta)^2} f(\bar{w}^1 - \bar{w}^2), \quad (3.17)$$

$$\sigma_2 \frac{g \Delta \bar{\theta}_v^{-2}}{\Theta_0} = -\sigma_1 \Delta \bar{\theta}_v^{-1} + \frac{8\kappa^2}{r_1} \frac{\sigma_1^2 \zeta^2 (1 + \zeta)}{(1 - \sqrt{\sigma_1})^2} f(\bar{w}^2 - \bar{w}^3), \quad (3.18)$$

which need be solved together with equations 3.11 - 3.13. Note that σ_2 can be expressed in terms of σ_1 and ζ : $\sigma_2 = \sigma_1(\zeta^2 + 2\zeta)$. The environmental velocity \bar{w}^3 follows from equation 3.12. A further simplification can be obtained by studying the equations in dimensionless form, where we rescale the velocities by the buoyancy velocity scale

$$W = \sqrt{g \Delta \bar{\theta}_v^{-1} (2r_1) / \Theta_0}, \quad (3.19)$$

commonly used in Rayleigh-Benard convection. From the LES data we know that W is of the order unity; for example, for clouds with size $L_c = 2r_1 = 400$ m we find $W \approx 2$ m s⁻¹. Using $w_n = \bar{w}^n / W$ and introducing the parameter b which represents the average buoyancy in the shell relative to the average buoyancy in the cloud, that is, $b = \bar{\theta}_v^{-2} / \bar{\theta}_v^{-1}$, we get

$$1 = \frac{(4\kappa\zeta)^2}{(1 + \zeta)^2} f(w_1 - w_2), \quad (3.20)$$

$$1 + b(\zeta^2 + 2\zeta) = \frac{(4\kappa\zeta)^2 (1 + \zeta) \sigma_1}{(1 - \sqrt{\sigma_1})^2} f(w_2 - w_3). \quad (3.21)$$

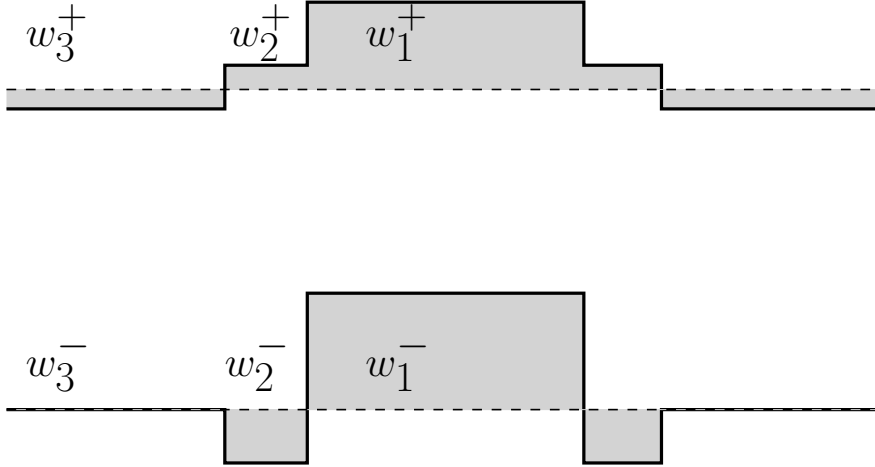


Figure 3.12: The two distinct types of solutions resulting from the conceptual model: (top) solution w_2^+ , the velocity in the shell lies between the cloud velocity and the environmental velocity; (bottom) solution w_2^- , the shell velocity is significantly lower than the environmental velocity.

We can now solve the equations and derive expressions for w_1 and w_2 in terms of the parameters b and ζ , the relative buoyancy, and the relative size of the shell, respectively. Using equation 3.20 one immediately arrives at

$$w_1 = w_2 + \frac{1 + \zeta}{4\kappa\zeta}. \quad (3.22)$$

Substituting this expression in equation 3.21, an expression for w_2 can be found analytically, which gives rise to two distinct types of solutions. These are depicted schematically in figure 3.12: the first (top panel) solution is the one that would be expected to arise when disregarding evaporative cooling, or when the upward force due to shear with the in-cloud updraft would be dominant; then the shell velocity would be somewhere between the mean cloud velocity and the velocity of the environment: $w_1 > w_2 > w_3$. The solution depicted in the bottom panel is the one that actually appears to arise in observations and in LES, with a distinct negative velocity in the shell, that is, $w_2 < w_3$.

The exact expressions are still rather involved, but since the cloud cover σ_1 is small (we take $\sigma_1 = 0.05$) one can get approximate but accurate and more transparent expressions can be achieved by assuming $w_3 = 0$. This is justified since $w_1 = \mathcal{O}(1)$, $w_2 = \mathcal{O}(1)$ whereas $w_3 = \mathcal{O}(\sigma_1)$. Note that this does suggest an inde-

pendence of the solution from the exact value of w_3 . In this way we arrive at

$$w_2 = \begin{cases} w_2^+ = +\frac{1}{4\kappa\zeta} \sqrt{\frac{1+b(\zeta^2+2\zeta)}{(1+\zeta)\sigma_1}} & \text{if } b \geq b^+(\zeta) \\ w_2^- = -\frac{1}{4\kappa\zeta} \sqrt{-\frac{1+b(\zeta^2+2\zeta)}{(1+\zeta)\sigma_1}} & \text{if } b^-(\zeta) < b \leq b^+(\zeta) \end{cases}, \quad (3.23)$$

with

$$b^+(\zeta) = -\frac{1}{\zeta^2 + 2\zeta}, \quad (3.24)$$

$$b^-(\zeta) = -\frac{1 + (1 + \zeta)^3 \sigma_1}{\zeta^2 + 2\zeta}. \quad (3.25)$$

The corresponding cloud velocity solutions w_1^\pm follow from equation 3.22. We have plotted the solutions for w_1 and w_2 as a function of the shell buoyancy b for a fixed relative shell size of $\zeta = 0.5$ in figure 3.13. The interesting point about the graphs and the structure of the solutions is that the descending shell solution w_2^- can only occur if the relative buoyancy and shell-size are just right, that is, b must lie between $b^-(\zeta)$ and $b^+(\zeta)$. For $b > b^+(\zeta)$ the shell (negative) buoyancy is not sufficient for the air to descend and the system settles into the solution w_2^+ ; on the other hand, if $b < b^-(\zeta)$, the shell buoyancy is so negative that the system enters into the unphysical state where $w_1 < w_3$, that is, the shell drags the entire cloud down. Hence the value of the shell buoyancy is rather a subtle parameter. This observation also holds for other values of the relative shell size, as can be seen in the phase-diagram (figure 3.14), where we have indicated the occurrence of the solutions in the parameter space, i.e. the (ζ, b) plane. Clearly the region pertaining to the descending shell solution is rather small.

Of course we would wish to elaborate the model such that it is able to actually *predict* the buoyancy in the shell; to this end the transport of moisture q_t and temperature θ_l ought to be incorporated in the model, after which the buoyancy in the shell could be calculated by mixing cloudy properties (region 1) with environmental properties (region 3) into region 2. While such an approach is certainly feasible, we feel that at this stage such an extension would complicate the present model too much. The general conclusion from the present simple model is that the descending shell solution is an admissible mode within the system, but also a rather unlikely mode when compared to the rising shell mode. Apparently it can only occur as a result of a delicate balance between the shell size, the (negative) shell buoyancy and the cloud fraction. This creates a new puzzle why the descending shell is nevertheless the *preferred* mode in observations and LES.

3.7 CONCLUSIONS

In this study, conditionally averaged results of large-eddy simulations of shallow cumulus clouds were compared with observational results of Rodts et al. (2003) by

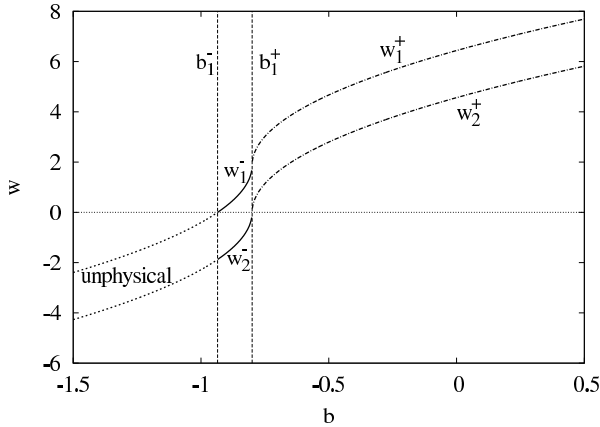


Figure 3.13: Dimensionless cloud velocity w_1 and shell velocity w_2 as a function of the relative buoyancy b in the shell, for a fixed relative shell size of $\zeta = 0.5$. Depending on the value of b the system settles either into solution w^+ (dash-dotted lines: shell velocity between that of the cloud and the environment), or the solution w^- (solid lines: shell velocity smaller than the environmental velocity).

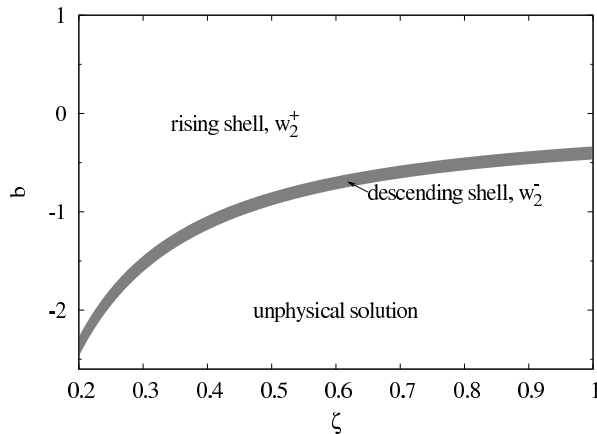


Figure 3.14: Phase diagram: the regions of existence of the solutions are indicated in the parameter space (ζ, b) . The region pertaining to the descending shell solution is remarkably small.

focusing on the dynamical properties of the cloud. It was found that the simulations generate clouds with velocity, temperature, and moisture profiles very similar to the observations. Several important features of the clouds in observations were present in the simulations as well, in particular the descending air mass surrounding the cloud; they were investigated in detail in the LES.

An investigation of the individual terms of the vertical momentum equation showed that buoyancy is the dominant force in the shell, suggesting that evaporative cooling through lateral mixing over the cloud edge is the mechanism responsible for the shell. No evidence could be found for a role throughout the entire cloud layer for mechanical forcing; this should have resulted in a significant negative pressure gradient force, which instead was found to be positive and thus even opposing the downdraft.

While around cloud-top downdrafts can also be caused by overshoots in the form of a crown-like shape around the cloud edge, evaporative cooling ensures a consistent existence of the shell at all but the lowest levels of the cloud. Interestingly this implies that from the point of view of the environment, the cloud is perceived as a negatively buoyant, downwards moving entity. Moreover, the vertical mass flux through the shell appears to be significant compared with upward mass flux in the cloud core; this is especially true for smaller clouds, which are the most numerous.

Since the shell drags along a significant amount of environmental air downward and entrains it into the cloud, this might reconcile the concept of lateral mixing with observations where the in-cloud air appears to originate from higher environmental levels. Since the shell constantly refreshes the air at cloud edge, this could enhance evaporative cooling, ultimately creating a stronger shell.

In the simulations we observed that the lateral cloud profiles are skewed by the mean horizontal wind. Partly, this can be attributed to the discrete grid of the numerical simulations, but this is mostly due to the vertical shear of the horizontal mean wind. This vertical shear creates not only a displacement of the cloud core away from the cloud center, but is also responsible for a humid shadow or halo on the downshear side of the cloud, as seen before in observations. Since this shear results in reduced mixing at the upshear side of the cloud while enhancing mixing at the downshear side, this yields an asymmetry in the appearance and size of the shell.

The behavior of the shell was illustrated by a simple three-layer model analogous to the model by Asai and Kasahara (1967) where buoyancy is balanced by lateral mixing. The model showed that the descending shell is indeed one of the possible realizations in the system, but that it can only occur when the shell buoyancy and the shell size are well tuned to each other. The other model realization, which is more in line with the concept of lateral mixing of scalar quantities and of momentum, displays air around the cloud being dragged along and *rises* with a velocity between that of the cloud and environment. This solution of the model appeared to be much less critical. This makes the occurrence of the descending shells in observations and LES even more surprising.

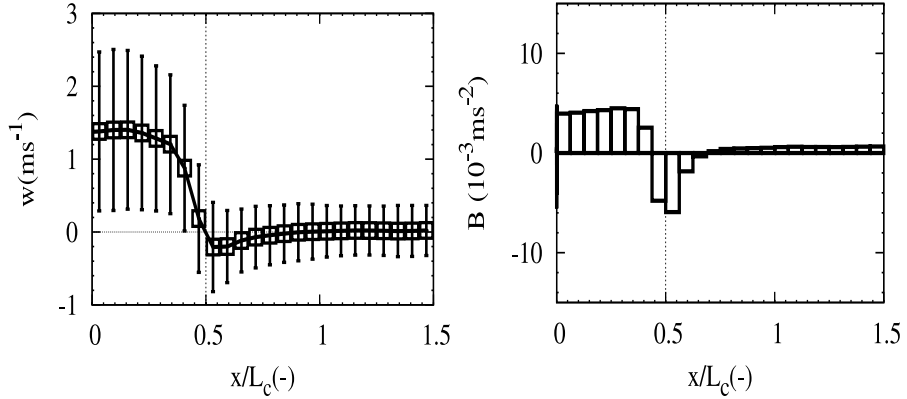


Figure 3.15: Vertical velocity and buoyancy profile obtained from simulations identical with those displayed in figure 3.3, save for a monotonous instead of a non-monotonous advection scheme.

APPENDIX 3.A ADVECTION SCHEME

Besides the physical explanations for the existence of the shell given above, one could argue that the occurrence in LES could also be due to numerical artifacts. For instance, the non-monotonous central differencing advection scheme could cause numerical overshoots (wiggles) at the cloud edge. Such wiggles would look very similar to a subsiding shell - especially since the extent of the shell is only a few grid points. To rule out this possible cause another 11 h BOMEX run is done with the monotonous third order upwind kappa advection scheme (see Hundsdorfer et al., 1995). From the $L_c = 400$ – m-sized clouds present in the final 8 hours of this simulation fly-through profiles were again collected at a height of 1000 m. This yields for the vertical velocity and the buoyancy the results displayed in figure 3.15. Comparing figure 3.15 with figure 3.3, a similar shell can be observed for both schemes, meaning that the shell is not a result of overshoots depending on the used advection scheme.

CHAPTER 4: OBSERVATIONAL VALIDATION OF THE COMPENSATING MASS FLUX THROUGH THE SHELL AROUND CUMULUS CLOUDS

The existence of a subsiding shell around cumulus clouds has been observed before in several aircraft measurement campaigns. Recent results from large-eddy simulations (LES) pointed out that the downward mass flux through the shell compensates a significant fraction of the upward mass flux through the cloud. In this study, airplane measurements from the Rain In Cumulus over the Ocean (RICO) field campaign are used to verify this compensating mass flux. Just like in the LES results, the in-shell downward mass flux is found to be significant. However, a few differences were found in comparison with the LES results; most of them were explained by taking into account the difference between the 2-dimensional slabs in LES and the 1-dimensional lines from airplane observations.

You're like the clouds in my home town
You just grow fat and hang around
and your days stretch out beneath the sun
And you don't live, you don't die,
you don't love so you don't cry
and we wait, to see just what we will become

I AM KLOOT

4.1 INTRODUCTION

The interaction between a shallow cumulus cloud and its environment has been a popular research topic for more than half a century. A significant part of the discussion has dealt with the significance of either cloud-top mixing or lateral mixing. Evidence for each mechanism has been shown both in modeling (e.g., Stommel, 1947; Squires, 1958b; Asai and Kasahara, 1967) as well as in observational studies (e.g., Paluch, 1979; Blyth et al., 1988; Taylor and Baker, 1991). In the same vein, Jonas (1990) and Rodts et al. (2003) investigated the behavior of the subsiding shell of descending air around cumuli, which was also studied by Grabowski and Clark (1991, 1993a,b) in an analysis of the cloud-boundary instability in a stably stratified (but possibly sheared) environment.

More recent studies attributed a larger significance to the shell than was inferred from previous works: Observations by Siebert et al. (2006) showed that the shell is

associated with increased turbulence around the cloud edge. Gerber et al. (2008) pointed out that the shell increases the humidity and lowers the temperature of the air or, in other words, *pre-conditions* the air entrained into the cloud. Both the increased turbulence and the pre-conditioning may lead to more homogeneous mixing at the edge of the cloud and shift the droplet size distribution toward smaller sizes. Heus and Jonker (2008b) found that the shell is able to compensate a significant portion of the in-cloud mass flux. This point was further elaborated by Jonker et al. (2008, hereafter JHS08) who stated that around 80% of the in-cloud mass flux was compensated within 200 m of the edge of the cloud. Thus, where the shell could hitherto be regarded as merely the fingerprint of cloud-environment mixing, it becomes more and more clear that the shell contributes to both the in-cloud droplet size distribution as well as the mass balance of the entire cloud field.

The large downward mass flux found by JHS08 in comparison with the previous studies was attributed to three factors. First, compositing data with respect to cloud edge instead of cloud center (which is more common) enabled JHS08 to better focus on the shell. Second, the determination of the nearest cloud edge was done in the 2-dimensional horizontal plane rather than along the airplane track only. This means that clouds alongside a flight track can also be accounted for; this significantly decreases the distance to the nearest cloud, and therefore the apparent location of the mass flux. Third, consideration of the mass flux rather than the vertical velocity better delineated the differences in importance due to the differences in area between cloud core, shell and far environment. This was a crucial point in the argument of JHS08, because the area of the shell is proportional to the perimeter of the cloud. This means that the area of the shell is significant compared with the area of the cloud core. Because mass flux is equal to vertical velocity integrated over area, the mass flux in the shell is easily underestimated.

In this study, we pursue verification of the numerical results of JHS08 by means of observations. To this end, we apply the JHS08 methodology to the airplane observations from the Rain In Cumulus over the Ocean (RICO) field campaign (Raubert et al., 2007a).

Our comparison of simulations and observations is two-staged. As argued above, a 2-dimensional view of the horizontal plane is necessary to fully appreciate the downward mass flux in the shell. Ideally speaking, we would like to validate the 2D results from LES directly with 2D observational data. Because such 2D observations are not available, we analyse the LES data set twice: Once from a 2D point of view, strictly following JHS08's method, and a second time, from a 1D point of view. The latter method is prone to several biases, as JHS08 argued, but the 1D observations are prone to the same biases. This means that a reliable *validation* can be performed by comparing the 1D LES results with the observations. If this validation is successful, this gives credence to the 2D LES results. The difference between 2D and 1D sampling aside, possible causes for difference between the airplane observations and the LES include the finite resolution of the LES and associated filtering of the subgrid scales, as well as the influence of the non-random flight pattern in the observations.

The details of the methodology of the airplane observations, of the LES, and of our analysis are described in section 4.2. In section 4.3, the results of this analysis are presented, and the reasons behind the differences between observational and numerical results are discussed. The dynamical structure of the cloud layer is more generally treated in section 4.4 and 4.5. Finally, some implications of this study are addressed in section 4.6.

4.2 DATA DESCRIPTION AND METHODOLOGY

4.2.1 Description of the airplane observations

We use data collected by the NSF/NCAR C130 airplane in the RICO campaign. Details of the campaign in general and of the flight plan in particular have been described in Rauber et al. (2007a) and Rauber et al. (2007b); a short summary of the relevant information is given here.

The data was obtained between December 7, 2004 and January 12, 2005 (see table 4.1 for some details). Each flight contains several semirandom trajectories at fixed altitudes with a duration of 30 – 60 min; as an illustration, the flight track of December 7, 2005 is shown in figure 4.1. The term ‘semirandom’ implies that the airplane typically aimed at transecting as many large, active, cumulus clouds as possible within a wide sector and penetrating them away from the edges, but that nevertheless (by chance) smaller clouds and the environment are fairly well represented in the ensemble. That is, there was no completely objective algorithm used to configure the airplane flight path.

Droplet number density was measured with the NCAR FSSP-100, a PMS Forward Scattering Spectrometer Probe with a sample rate of 10 s^{-1} . Velocities were obtained at 25 Hz from navigation information and pressure differences measured with a five-hole system on the aircraft radome. Temperature was measured with a Rosemount thermometer at 25 Hz.

A transect is defined as cloudy if the droplet number density continuously exceeds a threshold of 7 cm^{-3} , to avoid that phantom clouds are created due to sampling noise (see Rodts et al., 2003). The results of this paper are not very sensitive to the exact value of this threshold. Velocity and temperature are downsampled and interpolated where necessary to 10 Hz to match the frequency of droplet number observations. Combined with the average cruise speed of the C130 of 106 m s^{-1} this results in a spatial resolution of 10.6 m. The total number of samples observed by the airplane at each height $N(z)$ ranges between 1×10^5 and 4×10^5 in the cloud layer, and the total number of transected clouds at each height ranges between 644 and 4877.

4.2.2 Description of the LES

The work of JHS08 used simulations based on the Small Cumulus Microphysics Study (SCMS). In comparison with the RICO observations we use, the differences

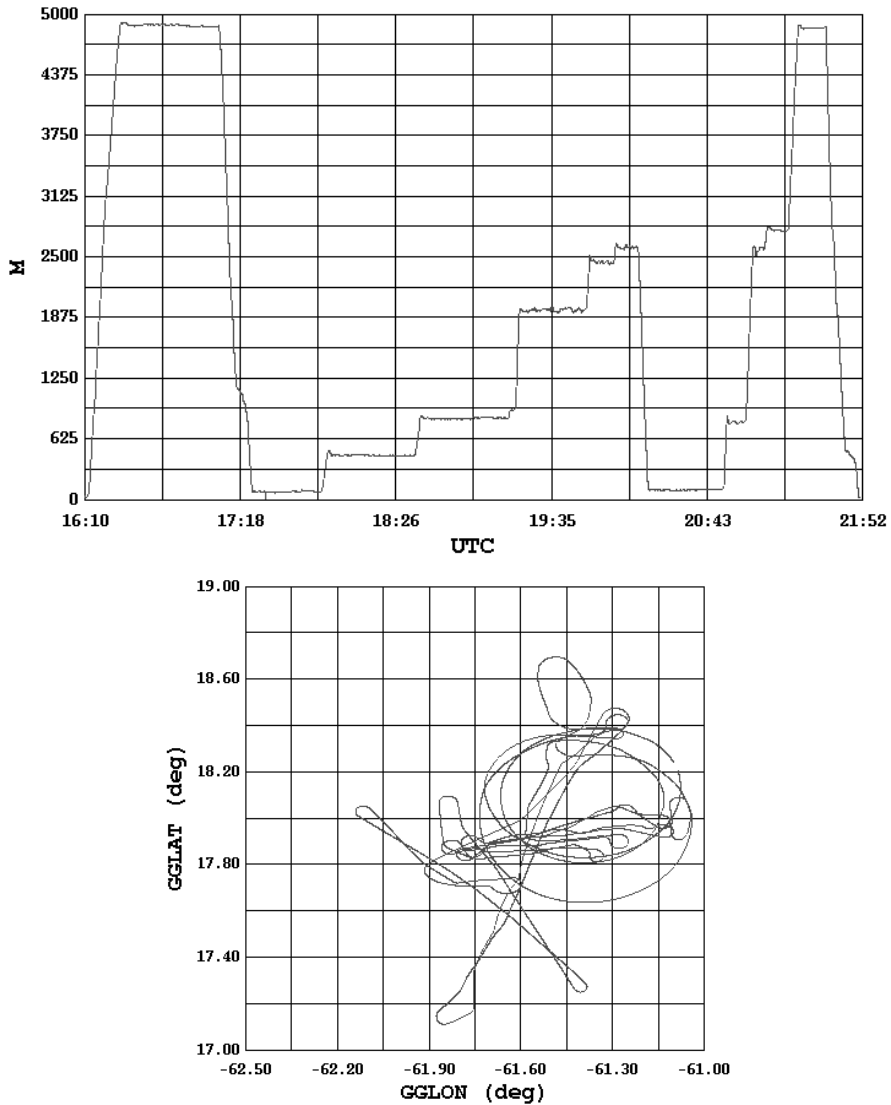


Figure 4.1: The flight track of the NCAR C130 aircraft during December 7, 2004 of the RICO campaign.

Table 4.1: Some specifications of the analyzed flights.

Flight	Date	Cloud base (m)	Flight heights (m)						
RF01	Dec 7	650	830	1940					
RF03	Dec 9	450	830	1470					
RF04	Dec 10	570	650	980	1320				
RF05	Dec 13	300	780	1090	1440	1780	1880		
RF06	Dec 16	550	640	730	790	900	980		
RF09	Dec 20	480	660	830	910	1050	1150	1270	
			1360	2000					
RF10	Jan 5	680	840	980	1160	1320	1620		
RF12	Jan 11	600	800	850	1000	1180	1480	1640	
RF13	Jan 12	400	770	1950					

in boundary conditions between the SCMS case and the RICO case is a possible source of differences. To eliminate this possibility, we compare the airplane observations with the LES intercomparison based on the RICO case as described by van Zanten et al. (2008). The numerical runs are performed using version 3 of the Dutch Atmospheric LES (DALES3; Heus et al., 2008f). We use $1024 \times 1024 \times 100$ gridpoints on a $12.8 \text{ km} \times 12.8 \text{ km} \times 4 \text{ km}$ domain, resulting in a $12.5 \text{ m} \times 12.5 \text{ m} \times 40 \text{ m}$ resolution. Although this is an idealized case, based on the average properties of the RICO observations, and run on a much smaller domain than the airplane could cover, the mean profiles of the liquid water potential temperature θ_l and the total water content q_t after 20 h lie well within the range of observations. See figure 4.2, and see van Zanten et al. (2008) for an in-depth discussion. A time window of 24 h is simulated, of which the final 4 h is used for data collection, with a sampling time of 1 min, yielding around 1.2×10^5 transected clouds per height. In the remainder of this paper, the word ‘observations’ always refers to the airplane observations, and never to the numerical results.

4.2.3 Definition of the variables in use

Because the main aim of this study is to validate the mass flux distribution as observed by JHS08, we follow their method of compositing with reference to the cloud edge as closely as possible. For all samples $i = 1 \dots N(z)$ along a fixed-altitude track the distance r_i to the nearest cloud edge has been determined. For in-cloud samples, r_i is taken to be negative, and for environmental samples r_i is defined positive. A schematical overview of this sampling method is given in figure 4.3. Distances to the cloud edge are obtained by calculating r_i in 2D as well as in the x -direction only, mimicking the 1D airplane observations. If an entire line in the x -direction is cloudless, the 1D distance is set to domain size. This horizontal distance

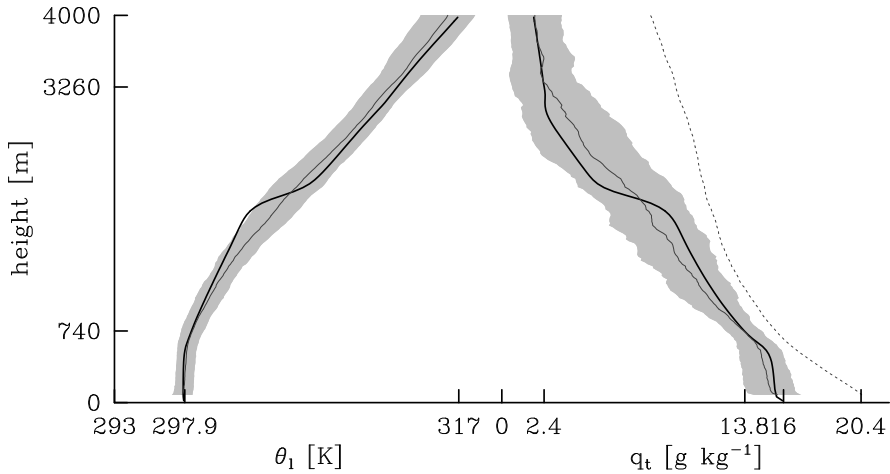


Figure 4.2: Mean profiles of the potential temperature θ_1 and the specific humidity q_t of all radiosondes released from Spanish Point in the period 04/12/16-05/01/08, here shown in dark grey. The shaded area denotes the mean value plus or minus the standard deviation. The dotted black line in the second panel indicates the mean profile of saturation specific humidity during this period. The LES profiles after 20h for the composite case are shown in black. Based on van Zanten et al. (2008).

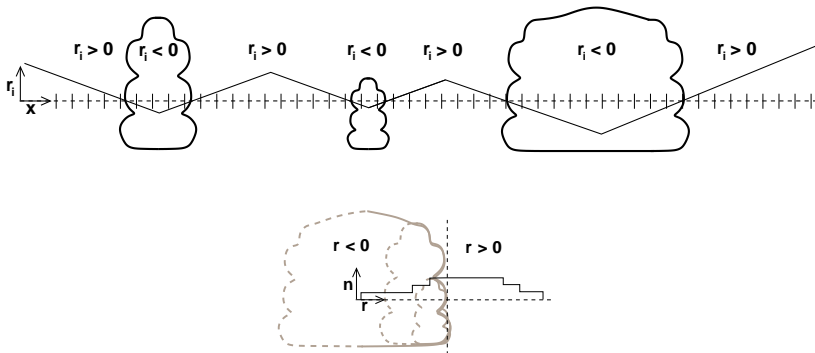


Figure 4.3: A schematic overview of the calculation of the distance to the nearest cloud edge r_i and the resulting calculation of the fractional area density $n(r)$.

to the cloud edge is analogous to what Lenschow et al. (2000) used to study cloud-top entrainment in stratocumulus. Note that we deviate here from JHS08's method; they determined the distance r_i to the cloud edge in 2D, whereas the airplane data only allows for a 1D calculation of this distance. In the analysis of our LES results, distances to the cloud edge are obtained by calculating r_i in 2D as well as in the x -direction only, mimicking the 1D airplane observations. If an entire line in the x -direction of the LES domain is cloudless, the 1D distance is set to domain size. The difference between the 1D and 2D calculation of the distance can be immediately appreciated with help of figure 4.4, where the value of r_i is plotted for a snapshot of the LES domain, either for a 2D calculation of r_i , or for the 1D calculation, flying parallel to the x -axis.

The main argument of JHS08 was that the large negative mass flux around the cloud edge is caused by the relatively large area of the shell. Like JHS08, we define a fractional area density as the normalized number of locations with a distance r to the cloud edge:

$$n(r) = \frac{1}{N(z)\Delta r} \sum_{i=1}^{N(z)} \Pi\left(\frac{r_i - r}{\Delta r}\right), \quad (4.1)$$

with Δr the bin size, and $\Pi(x)$ the unit pulse, which is equal to 1 for $-1/2 < x < 1/2$ and 0 elsewhere. This means that a fraction of $n(r)\Delta r$ of the ensemble is located at a distance to the nearest cloud edge between $r - 1/2\Delta r$ and $r + 1/2\Delta r$. Technically speaking, $n(r)$ is of course a fractional path density for the 1D analysis, but if the observed properties at the flight track are representative over some arbitrary path width δ , $n(r)$ equates to the more familiar area density.

$n(r)$ contains information on the cloud size distribution (for $r < 0$) and the void distance distribution (the free path between two clouds) for $r > 0$. To avoid undersampling, we have chosen the bin size $\Delta r = 12$ m, slightly larger than the average sampling resolution of 10.6 m.

The mass flux density is

$$m(r) = \bar{w}(r)n(r), \quad (4.2)$$

with $\bar{w}(r)$ the vertical velocity, conditionally averaged over all samples i where $r_i = r$ and with the mass density ρ omitted for brevity. If the longest cloud transect has a size of $L_c = L_{\max}$, then integrating $n(r)$ from $r = -L_{\max}/2$ to $r = +\infty$ yields 1 by definition. For a random flight pattern, $m(r)$ integrates to 0 because of mass conservation. After a careful analysis of all flight data, we averaged all tracks within a layer of 300 m. These windows refer to the mean height; so, for instance, the results of 650 m above the Earth's surface have been measured between 500 m and 800 m.

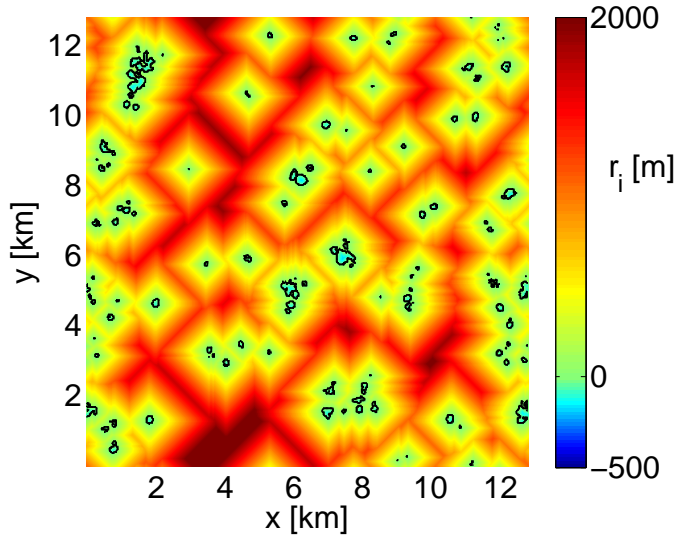
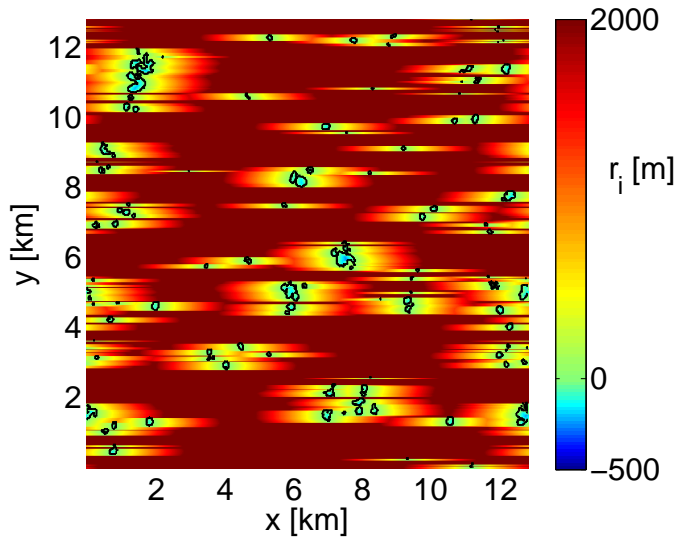
(a) r_i calculated in a 2D manner.(b) r_i calculated in a 1D manner.

Figure 4.4: Distance to the nearest cloud r_i calculated for a snapshot of the LES. Isolines depict the cloud border a) calculated in two dimensions, and b) calculated in 1 dimension parallel to the x -axis.

4.3 VALIDATION OF THE REFINED MASS-FLUX MODEL

4.3.1 Comparison between LES and observations

The fractional area density (figure 4.5) and fractional mass flux $m\Delta r$ (figure 4.6) resulting from observations and from LES are compared with each other. Because we are interested in a process driven by lateral mixing, we only present results for the middle region of the cloud layer, between 900 m and 1800 m above the surface. Outside this region, careful comparison is hampered by the precise location of cloud base and the inversion layer. The 2D results are very similar to the results of JHS08. As expected, there are some notable differences between the 2D and 1D results. By definition, the 1D probability density function $n(r)$ peaks at the cloud edge, because every in-cloud transect begins and ends at cloud edge, and the same can be said about every transect between two clouds. Such conditions need not to hold for the 2D fractional area density, because in that case the fractional area density is proportional to the distance to the nearest cloud center, and is bounded by the void distance between clouds. This results into a maximum in figure 4.5(a) around 500 m outside the cloud. The relatively short tail of the 2D pdf may be explained by the fact that clouds which are located alongside a flight track result in a small value for r in the 2D pdf, but are not taken into account in the 1D pdf's.

The main objective of this study can immediately be achieved with a qualitative look at figure 4.6(c). Our results extracted from the airplane observations show a significant negative fractional mass flux at the cloud edge. Further away from the cloud the net mass flux is close to zero, despite the sizeable area of the far environment. Indeed, the fractional area density in observations peaks much sharper at the cloud edge than even predicted by LES and consequently shows a larger near-cloud downward mass flux.

The accumulated mass flux for the entire cloud field $M(r)$ is defined as

$$M(r) = \int_{-\frac{1}{2}L_{\max}}^r m(r')dr'. \quad (4.3)$$

$M(r)$ is presented in figure 4.7. The total in-cloud mass flux M_c is equal to $M(r = 0)$, because r is negative inside the cloud. For $r \rightarrow \infty$, all locations in the domain are accounted for in the mass flux and $M(r)$ should go to zero, although this can be a slow process for 1D distance calculation, and the sensitivity to a bias in the mass flux density is quite large. This is reflected by the mass flux for large r in observations for different heights, which ranges from stable or even somewhat increasing to sharply negative. Obviously, this should be interpreted rather cautiously. Qualitatively, observations and simulations result in a similarly shaped curve of M . However, the difference in the reported total in-cloud mass flux M_c is surprising. In figure 4.7, this total in-cloud mass flux can be found by looking at the value of M at the cloud edge, i.e., $M_c = M(0)$. According to LES, M_c is less than half of the value found in the observations.

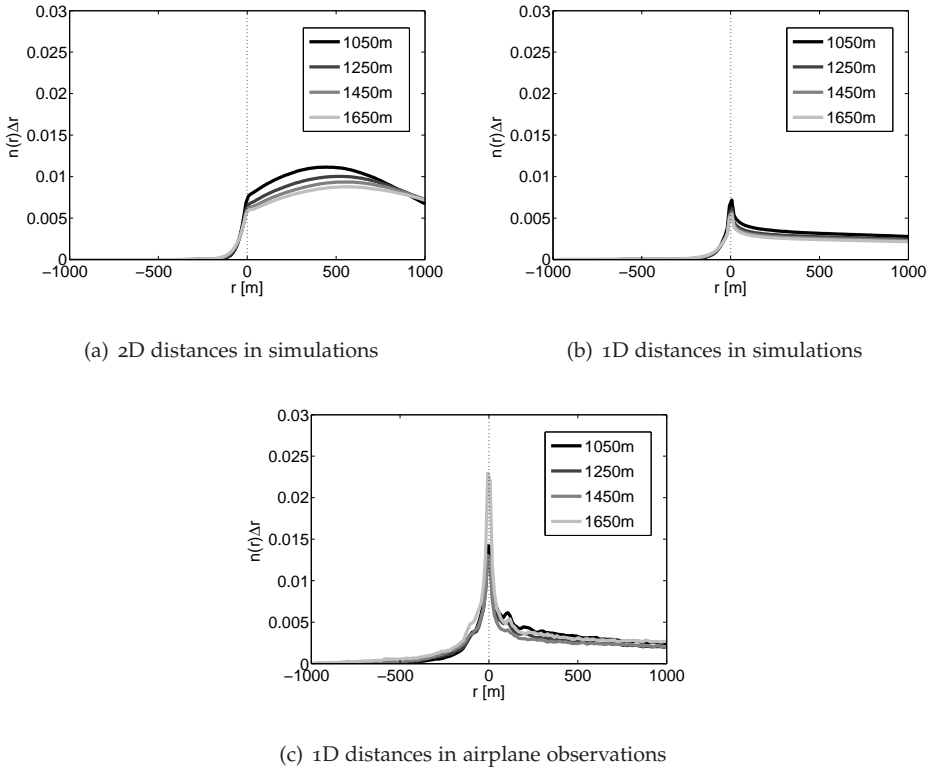


Figure 4.5: Fractional area density function as a function of r for different observation levels.

4.3.2 Causes of the differences between observations and LES results

There are several possible causes of the differences between observations and LES. One is the discrepancy in large clouds between LES and observations, which is most likely due to a bias in the flight pattern toward clouds, and to penetration through the center of larger, active clouds in particular. As Neggers et al. (2003b) showed, this could have a sizeable effect on the observed mass flux. To mimic such a bias in LES, an additional analysis of the numerical data is done, but now only regarding the lines where at some point r_i is below -200 m, meaning that the size L_c of at least one of the transected clouds is larger than 400 m. The results of this analysis are shown in figure 4.8.

According to LES, M_c is less than half of the value found in the observations. This can be completely attributed to the non-random flight track of observations (figure 4.9). While the discrepancy in such a key parameter as the total in-cloud

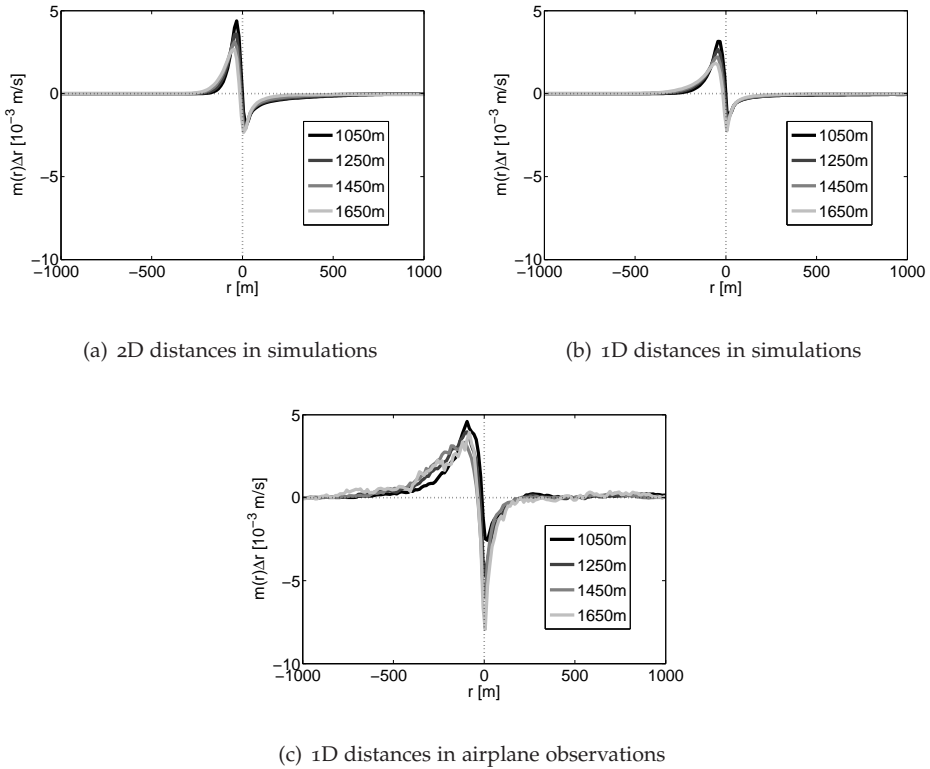


Figure 4.6: Fractional mass flux as a function of r for different observation levels.

mass flux is well-explainable, it is something that should be treated cautiously in any comparison of airplane data and other forms of retrieval.

From a comparison between figure 4.5(c), figure 4.6(c) and figure 4.8 it is clear that after focussing on the large clouds, the in-cloud fractional area density and mass flux density of LES agrees much better with the results from observations. However, the subsiding shell is still underpredicted by LES. More precisely, the width of the shell is well-predicted by LES, but the negative mass flux density very close to the edge of the cloud cannot be matched in simulations. It could be argued that even with a horizontal resolution of 12.5 m, LES cannot fully resolve the shell. Given the computer resources currently available, much higher resolutions simulations could not be performed. However, to obtain an indication of this error, simulations were performed at a lower resolution, with $\Delta x = 100$ m, which is an often used gridspacing for this type of simulations. The massflux density of these simulations are presented in figure 4.10. Clearly, coarser simulations are not able to well resolve the subsiding shell, or the maximum in-cloud mass flux. Although

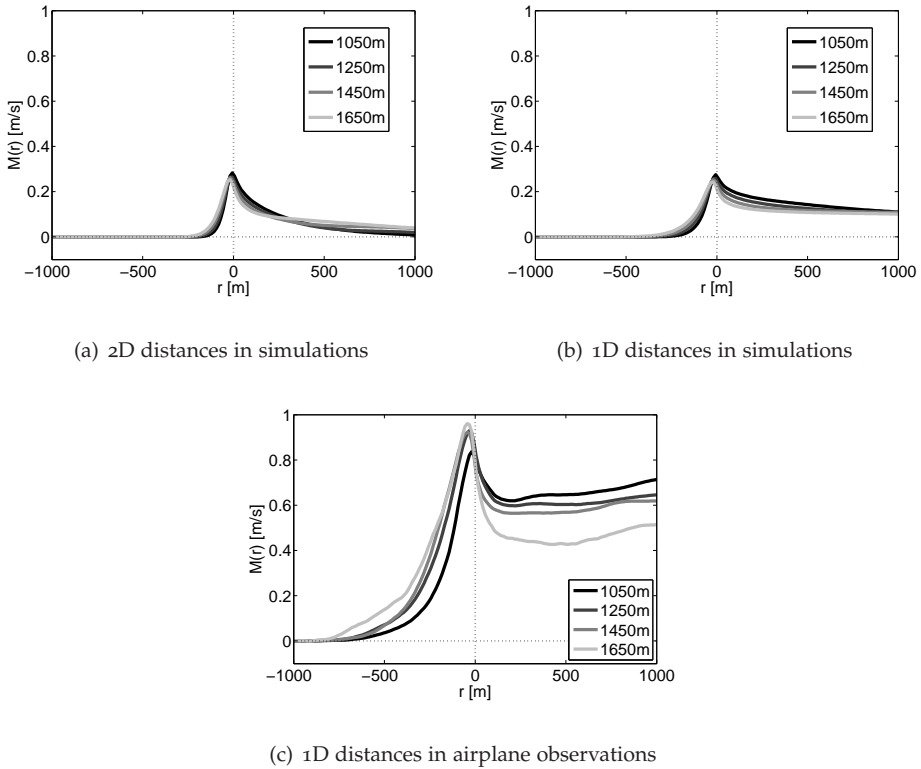
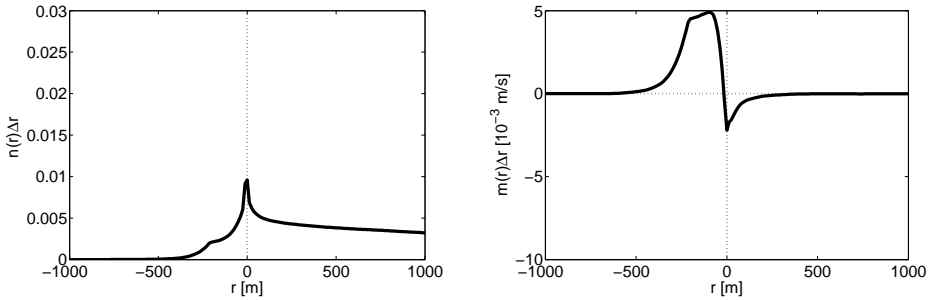


Figure 4.7: Accumulated mass flux as a function of r for different observation levels.

this resolution issue is probably not the only reason why the shell is not as deep in LES as it is in the observations, it seems to be one of the causes. A few other potential discrepancies between observations and numerics have no significant influence on the results as presented above: Filtering out the smallest clouds from the observations, or applying the LES filter over the observational data, did not alter the results by much. Also, subtracting the mean vertical velocity from the observational data to correct for possible calibration errors did not alter the results substantially, save for the fact that this would make the cumulative mass flux go to 0 in the far environment ($r \gg 0$) by definition.

Summarizing, we see that it is non-trivial to obtain ironclad proof from the observational results alone that most of the in-cloud mass flux is compensated within a few hundred meters of the cloud edge. However, with the observations and numerical tools combined, the observed fractional mass flux is shown to behave as expected. This clearly shows that subsiding shell plays the role that has been predicted by JHS08. Given that the vertical velocity at the cloud edge is much more



(a) Fractional area density for 1D distances in LES through large clouds. (b) Fractional mass flux for 1D distances in LES through large clouds.

Figure 4.8: The fractional area density and mass flux density as perceived by 1D measurements in LES over lines containing clouds larger than 400 m.

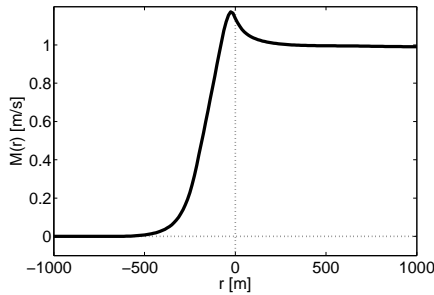


Figure 4.9: Accumulated mass flux as a function of r over lines in LES with large clouds on it.

negative in observations than seen in LES, the role of the subsiding shell seems to be even stronger in reality than predicted. The minimum value of w aside, the agreement between the results obtained from observations and the 1-dimensional interpretation of LES give confidence that the 2-dimensional interpretation of the LES results of JHS08 is correct.

4.4 A CLOSER LOOK AT THE UP- AND DOWNDRAFTS

So far, we concentrated primarily on downdrafts near the edge of the cloud. In this section, also the occurrence of up- and downdrafts deeper inside the cloud

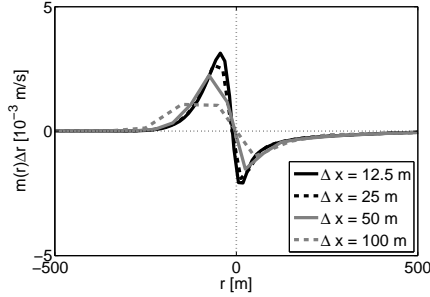


Figure 4.10: The mass flux density as perceived by 1D measurements in LES for several resolutions.

as well as in the far environment are treated. The results will be presented for a measurement height of 1450 m, but as was already shown in the previous section, within the cloud layer, the results are reasonably height-independent. In figure 4.6, the mean fractional mass flux was presented. While these results show that on average the far environment has a negligible velocity, this does not mean that the air in this region remains motionless, only that the upward velocities are balanced by the downward velocities. Likewise, the net positive fractional mass flux inside the cloud is the sum of up- and downdrafts. To better study these up- and downdrafts, we need to further condition the sampling to updrafts ($w_i > 0$, denoted with a +) and downdrafts ($w_i < 0$, denoted with a -). Thus we define an up- and downdraft number fraction

$$n^\pm(r)\Delta r = \frac{1}{N(z)} \sum_i^{N(z)} \Pi\left(\frac{r_i - r}{\Delta r}\right) H(\pm w_i), \quad (4.4)$$

a conditional average velocity

$$\bar{w}^\pm(r) = \frac{1}{n^\pm} \sum_i^{N(z)} w_i \Pi\left(\frac{r_i - r}{\Delta r}\right) H(\pm w_i), \quad (4.5)$$

and a conditional mass flux density:

$$m^\pm(r) = n^\pm(r)w^\pm(r), \quad (4.6)$$

with $H(x)$ the Heaviside step function. By definition, $n^+(r) + n^-(r) = n(r)$. In figure 4.11 the number fractions are presented for the 1450 m window, normalized with $n(r)$; thus, the two curves in figure 4.11 add up to 1. The corresponding average upward and downward velocities are shown in figure 4.12.

In general the vertical velocity corresponds well between observations and simulations. The most notable difference is a larger separation between the average

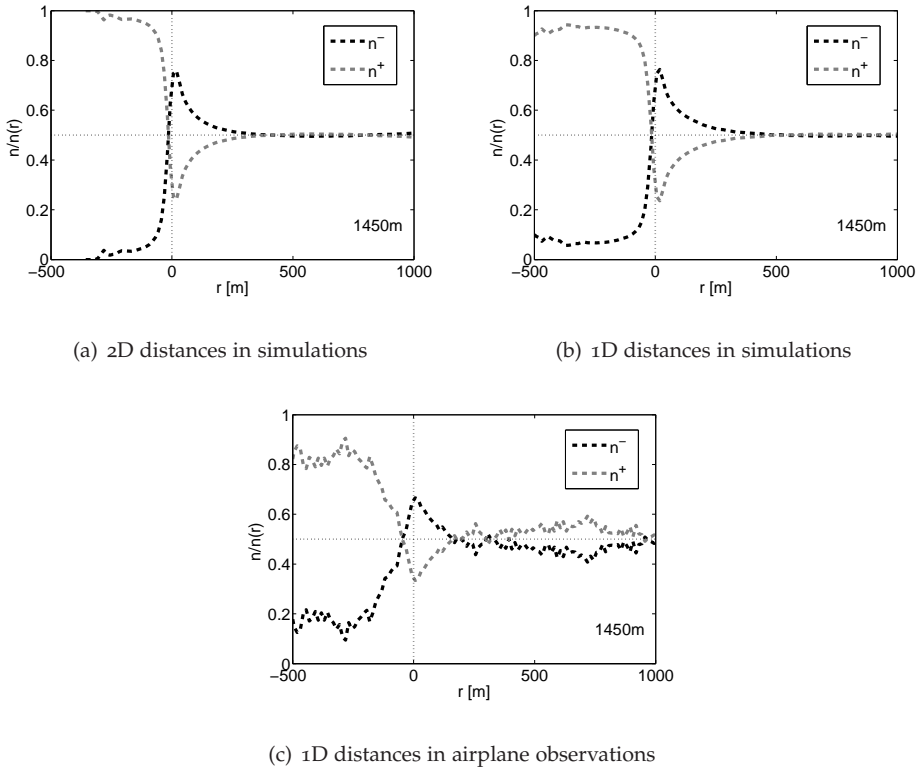


Figure 4.11: Up- and downward number fraction at 1450 m. The light dashed line is the fraction of updrafts, the dark dashed line is the fraction of downdrafts.

upward and downward velocities in observations, inside the cloud, at the cloud edge as well as in the environment. For both air-plane observations as well as in LES, in-cloud downward velocities are only a little smaller than the velocities at the cloud edge. Judging from the similarity between figures 4.12(b) and 4.12(c), these downdrafts seem to be quite well captured by LES. In figure 4.11(a), the number of downdrafts goes rapidly to zero in the 2D analysis for $r < -100$ m. This suggests that most of the downdrafts perceived by the airplane as deep inside the cloud, are actually cloud-edge downdrafts, when the airplane was flying alongside the edge of the cloud.

Another difference between observations and simulations is a sharper transition between cloud (or more precisely, the cloud core), shell and far environment in the simulations than in the observations, that can be seen in both the average velocity (figure 4.12) and especially in the fractional area density (figure 4.11).

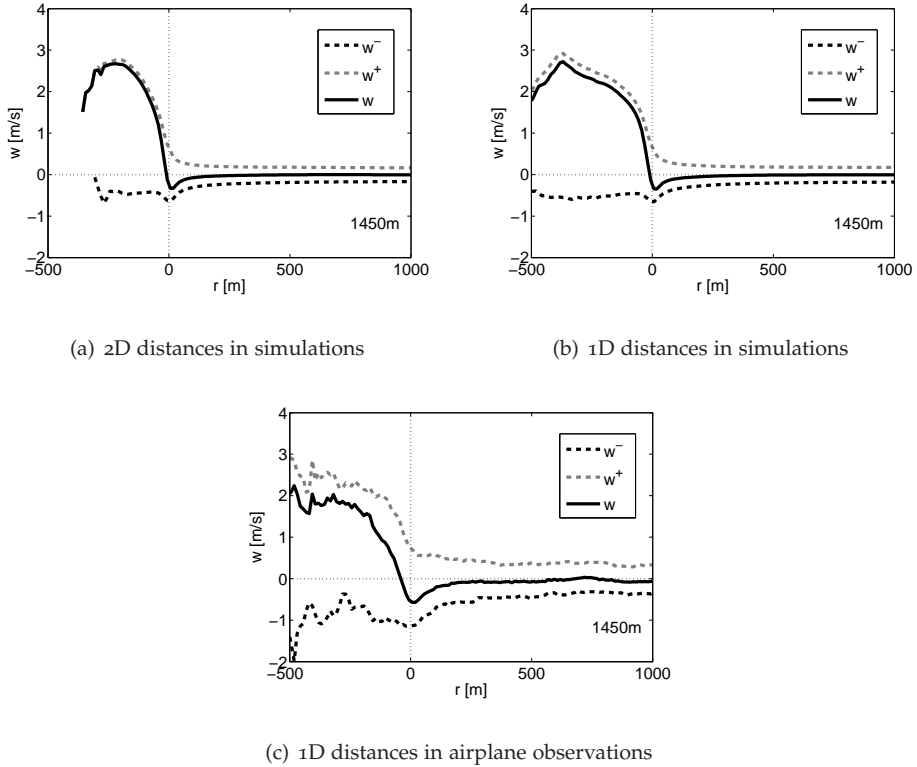


Figure 4.12: Conditional averaged vertical velocity as a function of r at 1450 m. The light dashed line is the average velocity of the updrafts, the dark dashed line is the average velocity of the downdrafts. The full line denotes the unconditionally averaged vertical velocity.

The results of figure 4.11 and 4.12 culminate in the conditional fractional mass flux as depicted in figure 4.13. Both in LES and in observations, the fractional mass flux follows the trend of the vertical velocity; within the cloud, the total mass flux is close to the updraft flux, around the edge the downdrafts dominate, and in the far environment the upward and downward mass flux cancel out each other. This tendency of the total mass flux to follow the dominant conditional mass flux is exaggerated by LES. The more diffuse transitions between cloud, shell and far environment in the observational results are again reflected in figure 4.13.

The coherency of the flow is investigated with the help of the normalized second order structure function

$$D(r, z) = \frac{\overline{(w(z) - w(z_0))^2}}{\sigma_w^2(r, z_0)}, \quad (4.7)$$

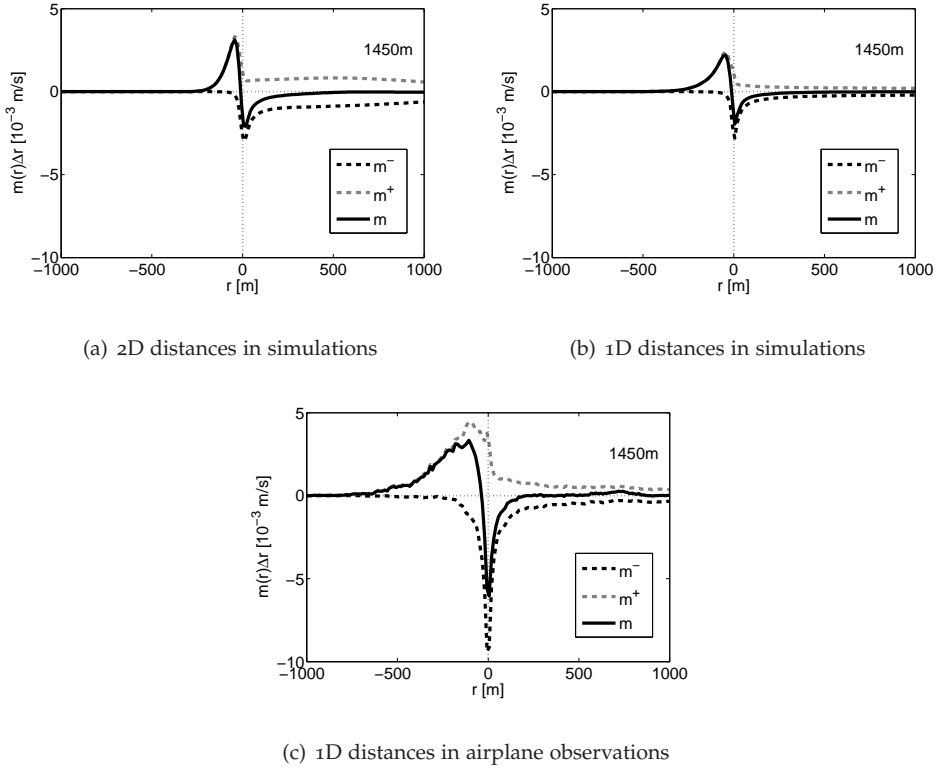


Figure 4.13: The conditional fractional mass flux as a function of r at 1450 m. The light dashed line is the updraft mass flux, the dark dashed line is the mass flux of the downdrafts. The black line denotes the total fractional mass flux.

with $z_0 = 1450$ m the reference height and σ_w^2 the variance of the vertical velocity. The structure function can be seen as the normalized difference in some field between two spatially separated points, and so gives a measure for the coherent length scales of the field. A structure function conditionally sampled over updrafts or downdrafts is defined as

$$D^\pm(r, z) = \frac{\overline{(w(z) - w^\pm(z_0))^2}}{\sigma_w^2(r, z_0)}, \quad (4.8)$$

where, again, $+$ denotes the updrafts and $-$ denotes the downdrafts. Because the height dependent information could not be obtained from the airplane observations, the structure functions were obtained from LES (with r calculated in 2D). They are plotted in figure 4.14. What immediately strikes the eye is the strong coherency in the in-cloud downdrafts. Although these downdrafts are scarce and

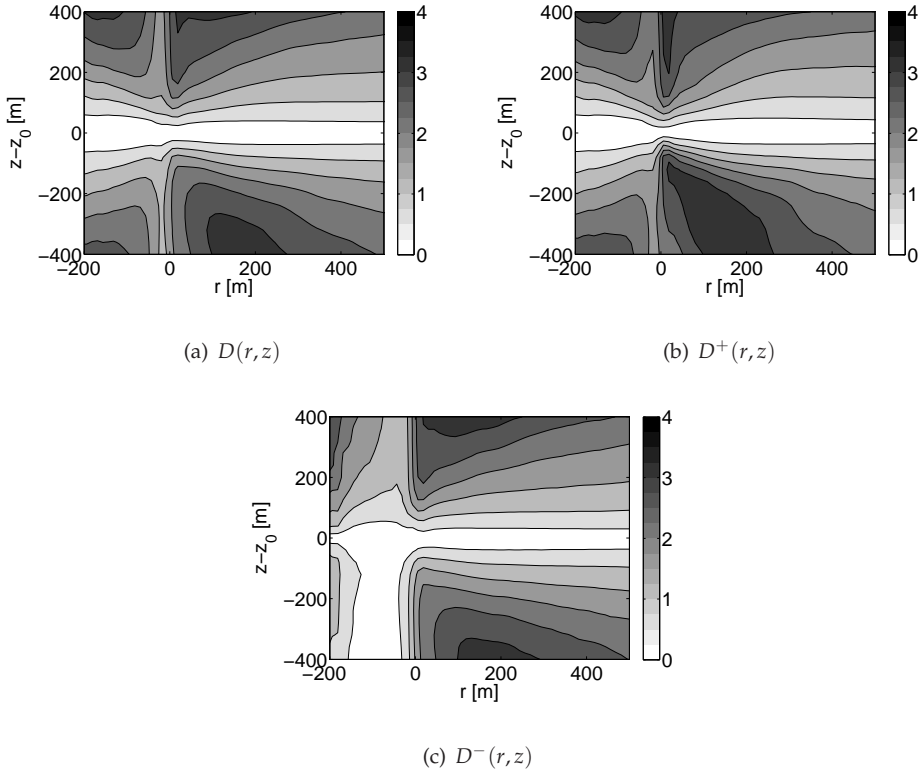


Figure 4.14: The normalized structure function $D(r, z)$ as function of r and distance-to-reference-height $z_0 = 1450$ m. Obtained from LES.

do not contribute much to the mass flux, they clearly do exist and - if present - are able to maintain themselves over a considerable distance. As for the in-cloud downdrafts, there is a clear difference visible in figure 4.14(c) in the coherency with higher levels and the coherency with lower levels in the cloud. The most probable cause of this asymmetry lies in the location of the cloud top. By definition, the local cloud top is somewhere, at varying height, above z_0 for the points inside the cloud, where $r < 0$. Cloud top clearly destroys the coherency of the flow. Because cloud base is located far below z_0 , such an effect does not happen for the coherency with the flow below z_0 .

The in-cloud updrafts on the other hand appear to be much less coherent than the in-cloud downdrafts. For the smaller clouds in the ensemble, z_0 is close enough to the cloud top to show clear changes in the velocity of the updrafts. Moreover, the term ‘updraft’ in this context is not related exclusively to a penetrative, buoyant cloud core; all kinds of small scale fluctuations are also taken into account here.

Because the average in-cloud velocity is larger than zero, the turbulent fluctuations centered around the cloud-mean velocity are almost exclusively accounted for in the updraft structure function of figure 4.14(b). The in-cloud downdrafts need to be quite intense to counteract the mean upflow in clouds, and because of that high intensity, the downdrafts are also more vertically coherent. So in contrast with the downdrafts, the turbulence emphasizes some smaller length scales in the in-cloud updrafts. Because of the predominance of the updrafts inside the cloud, the unconditionally sampled structure function is very similar to the structure function sampled over updrafts only.

In the far environment, the updrafts and downdrafts are similar to each other. Although on average not much is happening, the reduced turbulence and flow patterns like buoyancy waves allow for coherency over relatively large height differences.

Within the shell, around the edge of the cloud, a maximum in turbulence has been observed before (see Siebert et al., 2006; Heus and Jonker, 2008b); this maximum is here expressed in the small coherent length scales at cloud edge. This is especially true for the updrafts, because in addition to the increased turbulence, there is not much mean coherent upflow apparent in the shell. For downdrafts, the coherency is somewhat larger, although, as was shown by Heus et al. (2008a), the Lagrangian dispersion in the shell only extends to about 200 m.

4.5 THE VELOCITY DISTRIBUTIONS IN CLOUD, SHELL, AND ENVIRONMENT

In figure 4.15 we show the probability density function p_w of the vertical velocity conditionally sampled over the cloud core, the shell and the far environment, respectively.

In figure 4.12, it was already shown that the LES generates a more narrow w distribution than the observations; this is reflected in figure 4.15. It remains not entirely clear why exactly the observations and LES differ in this. Selecting or removing specific cloud sizes from the statistics, such as was done in section 4.3, does not change the w -distributions. Another possibility, that the removal of sub-filter-scale fluctuations in LES would diminish the variability turns out to be true, but does not contribute enough to explain the difference between observations and LES. The most likely remaining explanation is that, both in space and in time, the domain covered by the observations is much larger than in LES. This means that the conditions at all the places and times where the airplane flew differ much more from each other than the conditions within the 12.5 km^2 numerical domain varied. Inside the cloud, where the average vertical velocity is much larger than zero, such a narrow distribution is reflected in a decreased number of downdrafts inside the cloud. This could explain that the fraction of in-cloud downdrafts as seen in LES (figure 4.11(b)) is smaller than 10%, while the fraction of in-cloud downdrafts in observations hovers around 20% (figure 4.11(c)).

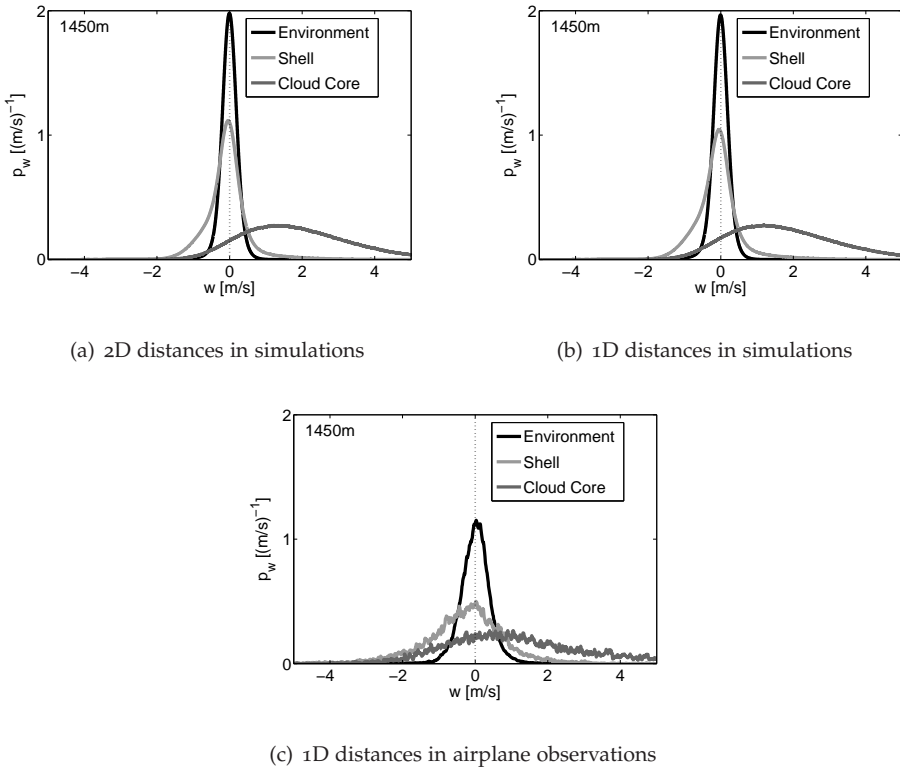


Figure 4.15: Probability density function of the vertical velocity in the far environment (black line), the shell (light gray) and the cloud core (dark gray).

Based on the results from e.g., figure 4.11(c), the shell is here defined as the region where $-50 \text{ m} < r < 150 \text{ m}$, and consequently the cloud core as $r < -50 \text{ m}$ and the far environment as $r > 150 \text{ m}$. We emphasize that the inner region is now not the entire cloud anymore, but only the part of the cloud with upward velocity, in other words, the cloud core. As noted before, the exact location of the borders does not entirely coincide with the location of the shell in LES. This is reflected in some minor variations between the plots, but the general picture obtained from the 3 panels in figure 4.15 is very much similar and confirms the results presented above. The pdf of the far environment is a slender bell-shaped curve with a mean at $w = 0$. The shell and the cloud core show much larger variance, and especially the shell shows a strong skewness that is responsible for a deviation of the mean from the mode. Indeed, the strong but relatively rare up- and downdrafts are the entities that ultimately characterize the flow in the core and the shell. To fully appreciate the role of the cloud core, the shell and the far environment, the fractional areas of the

Table 4.2: Transport properties of the cloud core, the shell and the far environment at 1450 m.

	Area [%]	\bar{w} [m s^{-1}]	M [10^{-3} m s^{-1}]
<i>LES, 2D distances</i>			
Cloud core	0.74	1.88	13.9
Shell	11	-0.060	-6.64
Environment	88	-0.0083	-7.29
<i>LES, 1D distances</i>			
Cloud core	0.97	1.76	14.9
Shell	9.9	-0.069	-6.8
Environment	89	-0.0092	-8.40
<i>LES, 1D distances, large clouds</i>			
Cloud core	4.6	1.87	85.5
Shell	10.1	-0.045	-4.8
Environment	84	-0.011	-9.95
<i>Observations, 1D distances</i>			
Cloud core	6.2	1.18	73.2
Shell	9.4	-0.31	-29.14
Env.	84	0.0081	6.8

3 regions are reported in table 4.2, along with the average velocity and the resulting fractional mass flux of each region. Clearly, while the area of the far environment is dominating over the area of the cloud and the area of the shell, the average velocity in the far environment is close to zero and a large part of the negative mass flux is concentrated in the shell. Once again, 1D calculations over large clouds in LES and in observations show very similar results, save for the vertical velocity in the shell.

4.6 CONCLUSIONS

In this study, the role of the subsiding shell around cumulus clouds was investigated by compositing airplane data with respect to the edge of the cloud, with focus on mass flux rather than on velocities. The role of the shell in the balance between the upward in-cloud mass flux and the downward mass flux outside the cloud was clearly confirmed. As observed before in LES, the shell is responsible for a large part of the environmental downward mass flux. The one-dimensional character of the airplane observations somewhat complicates interpretation of the velocity measurements in the context of a cloud shell. However, the role of the shell appears even stronger in observations than predicted by LES, probably due to a lack of resolution in LES to resolve the finest details of cloud-edge mixing. As in LES,

careful compositing of the observations relative to the cloud edge and sufficient sampling to average out the turbulence turn out to be key factors in revealing the role of the shell in transporting mass.

So far, the shell and its role in the mass flux balance has been discussed for marine and continental shallow cumuli, under sheared and uniform circumstances, for tropical convection and at the midlatitudes (Jonas, 1990). Evaporative cooling provides a direct physical mechanism in creating the shell, as long as lateral mixing is significant. Although the shell is also observable in deeper convection (as, e.g., in Malkus et al. (1953)), it is so far unclear how important the shell is in the mass balance of clouds deeper than a few kilometers. This is a direction for further research.

LES seems to be able to go well beyond qualitative insights and to quantitatively predict the velocity distribution and the mass flux density in and around a shallow cumulus cloud. Differences between simulations and observations can mostly be seen in the underprediction of downdrafts at the cloud edge, and in a smaller variation in vertical velocity. Some of the differences can be explained by biases in the flight path of the airplane, and some by the finite resolution of LES. Even by modern standards, a high resolution is necessary to resolve the important mechanisms of cumulus convection. Some issues however, especially in the variability of the vertical velocity, can not be attributed so easily. One possible cause for the higher variability in observations is the much larger domain covered by the airplane than by LES.

The overall probability density function of the vertical velocity w is dominated by a single peak at $w = 0$. However, for a correct understanding and modeling of the physics of the cloud layer, it is essential to interpret the pdf as trimodal: A large portion (the far environment) with negligible vertical velocity, and two small areas (the core and the shell) that approximately balance each other out.

The overall behavior of updrafts and downdrafts in and around the cloud, including their coherency and their transport of species remains to consist of many fascinating mechanisms. Not all of them could be treated here, and some could only be speculated upon within the framework of this paper. In other words, the dynamics of cumulus clouds is still, and probably will remain for quite some time, an interesting alley of research.

CHAPTER 5: MIXING IN SHALLOW CUMULUS CLOUDS STUDIED BY LAGRANGIAN PARTICLE TRACKING

Mixing between shallow cumulus clouds and their environment is studied using large-eddy simulations. The origin of in-cloud air is studied by two distinct methods: 1) by analyzing conserved variable mixing diagrams (Paluch diagrams) and 2) by tracing back cloud-air parcels represented by massless Lagrangian particles that follow the flow. The obtained Paluch diagrams are found to be similar to many results in the literature, but the source of entrained air found by particle tracking deviates from the source inferred from the Paluch analysis. Whereas the classical Paluch analysis seems to provide some evidence for cloud-top mixing, particle tracking shows that virtually all mixing occurs laterally. Particle trajectories averaged over the entire cloud ensemble also clearly indicate the absence of significant cloud top mixing in shallow cumulus clouds.

Molecules dissipate,
Disperse and re-coagulate.
Breathing in and out,
There is nothing more.
I am mist, you are steam
We are clouds,
We are drifting away.
Particles of light, particles of matter
Come together for an instant, then scatter.

QUASI

5.1 INTRODUCTION

The interaction between cumulus clouds and their environment has been a much debated issue for several decades. Stommel (1947) based his cloud model on the concept of a laterally entraining plume, but Squires (1958b) argued that cloud-top mixing and resulting penetrative downdrafts are better able to predict the behavior of cumuli. In this way, he could, for instance, better explain why liquid water content tends to be relatively constant throughout lateral transects. Later measurements found a lack of mean horizontal flow into the cloud (e.g., Telford and Wagner, 1974) in support of this view. On the other hand, Heymsfield et al. (1978) found

significant lateral mixing in a sheared environment for the nonbuoyant parts of the cloud. This diminishes the size of the moist adiabatic cloud core but leaves the rest of the core largely undiluted.

In the following years, the discussion on cloud-environment interaction was dominated by the use of conserved variable diagrams, as introduced in this field by the key paper of Paluch (1979, hereafter P79). She plotted the phase space of two conserved variables (equivalent potential temperature θ_q and the total water content q_t) of in-cloud air. These in-cloud properties, then, have to be a linear combination of the environmental values at the heights where the entrained air originates from. Because P79 found the in-cloud properties for large rising cumuli to be lying on a line between cloud base and cloud top, she concluded it highly likely that the source level of entrained air lies at cloud top.

More recent observations (e.g., Betts, 1982; Lamontagne and Telford, 1983; Jensen et al., 1985; Reuter and Yau, 1987b) obtained similar results for different pairs of conserved variables, especially in the upper part of the cloud. Others, such as Raymond and Wilkening (1982), Blyth et al. (1988), Taylor and Baker (1991), Neggers et al. (2002) and Zhao and Austin (2005a) observed source levels close to observation level, either in observations or in large-eddy simulations (LES). These sources around observation level, in particular, are found for the lower and middle part of the cloud and are usually explained by a buoyancy-sorting mechanism. In such a mechanism, a cloud core is defined as being positively buoyant with regard to the environment ($\theta_{v,core} > \theta_{v,env}$). It contains parcels of cloudy air rising to their level of neutral buoyancy, where they mix with the environment, evaporate and are eliminated from the ensemble. Taylor and Baker (1991, hereafter TB91) showed that in-cloud observations might appear to be linear combinations of air from two sources on a Paluch diagram but can also be explained by mixing from multiple sources followed by buoyancy sorting. Such a mechanism yields a triangular area that is usually pointing in the direction of observation level in the Paluch diagram, meaning that in-cloud parcels are distributed along a line. This lateral mixing also forms the basis for the mass-flux approach in many operational parameterizations (e.g., Siebesma and Cuijpers, 1995; Siebesma and Holtslag, 1996; von Salzen and McFarlane, 2002; Kain and Fritsch, 1993).

Blyth (1993) emphasized the role of a recirculating vortex at the top of the thermal in cloud mixing. This recirculation can be associated with a descending shell of air around the cloud (e.g., Reuter and Yau (1987a), Jonas (1990)). Rodts et al. (2003) and Heus and Jonker (2008b) found that this descending shell is also observed at lower heights and is due to evaporative cooling induced by lateral mixing. This shell is capable of dragging significant amounts of air downwards alongside the cloud, thus potentially explaining the observation of source levels in Paluch diagrams above observation levels in situations of dominant lateral mixing.

With the advance of radar measurements and the increase of computer power in the last decade, it became possible to give more direct evidence for cloud-environment interaction. Damiani et al. (2006) drew streamlines through radar observations, and others such as Lin and Arakawa (1997) or Carpenter et al. (1998b)

calculated backward trajectories through numerical simulations. Dispersion of a passive scalar allowed Zhao and Austin (2005b) to improve understanding of the role of the recirculating vortex on top of the ascending cloud top. The mechanisms and importance of, in particular, mixing with the bulk of the cloud, however, remain unclear.

This study is an attempt to resolve the issue of cloud-environment mixing of shallow cumuli by departing from the implicit Paluch analysis and determining the origin of in-cloud air explicitly. This is done by incorporating into LES many massless tracer particles that follow the flow and thus can represent in-cloud air parcels from a Lagrangian perspective. Such an approach has been followed before by Weil et al. (2004) or Dosio et al. (2005), for example, for the clear convective boundary layer. Because tracer particles are uniquely identifiable and follow the motion of air, they can serve as a powerful means to study the history of an individual parcel of in-cloud air. This way, the origin of the air inside a cloud can be found without imposing strong assumptions. The advantage of LES is that the cloud and its flow, temperature and moisture fields are known completely, with temporal and spatial resolution that are difficult to achieve in observational campaigns. LES has been widely used in various contexts and has been extensively validated for studies of the dynamics of non-precipitating cumulus clouds (e.g., Siebesma et al., 2003; Heus and Jonker, 2008b; Siebesma and Jonker, 2000). Thus, LES is capable of simulating a cloud field consisting of a large number of independent clouds and a solid statistical approach can be made.

The first part of this paper (section 5.3) consists of a comparison between the results using conserved variable diagrams like P79 and results obtained from particle tracking. The purpose of this exercise is twofold: 1) to see whether LES can obtain results similar to observations, and, if so, 2) to study the origin of the particles and compare it to the origin of the in-cloud air as inferred from the Paluch analysis. This analysis is performed by investigating a number of individual clouds, chosen to be similar to many observed clouds described in the literature.

The second part of this work treats cloud-environment interaction from a broader point of view. The focus shifts towards the ensemble average of the cloud field, instead of measurements of individual clouds that can easily be subject to stochastic events. By careful normalization and conditional sampling of clouds, the focus remains on the behavior of the individual but average cloud.

Discussion of the average motion of the particles in this fashion enables one to study the role of various entrainment and detrainment models:

- cloud-top entrainment followed by penetrative downdrafts, as modeled by Squires (1958b);
- entrainment and detrainment induced by a recirculating vortex at cloud top (Blyth et al., 1988);
- and entrainment and detrainment at the side of the cloud, either in the classical view of the shedding thermal (Stommel, 1947), buoyancy sorting (TB91),

or with some additional downwards motion due to the subsiding shell (Heus and Jonker, 2008b).

Finally, the results of the previous sections are discussed in relation with the role of clouds in transport through the CBL.

5.2 CASE SETUP

A parallelized version of the Dutch Atmospheric LES (DALES) model, as described by Cuijpers and Duynkerke (1993), was used to run the simulations. The numerical case used in the study is based on the Barbados Oceanographic and Meteorological EXperiment (BOMEX; Holland and Rasmusson, 1973). Because this marine cumulus case has no diurnal cycle and is almost in steady state, long simulations can be performed and the cloud field can be considered statistically stationary over the entire run. Sensible and latent surface heat fluxes amount to 8 W m^{-2} and 150 W m^{-2} , respectively (resulting in a Bowen ratio of $r_B = 0.05$). Cloud base is located around 500 m and the inversion layer lies between 1500 m and 2000 m; the typical horizontal cloud size is around 500 m. BOMEX shows a relatively large mean vertical shear, up to $1.8 \text{ m s}^{-1} \text{ km}^{-1}$. More detailed information on the numerical case can be found in the intercomparison study by Siebesma et al. (2003).

Simulations were carried out on a domain of $6.4 \text{ km} \times 6.4 \text{ km} \times 3.2 \text{ km}$, with a resolution of $\Delta x = \Delta y = 25 \text{ m}$, $\Delta z = 20 \text{ m}$ and a timestep of $\Delta t = 1 \text{ s}$. Three simulations (statistically identical, but each with a different random perturbation of the initial field) with a duration of 8 h each were performed; the first 3 h were discarded as spinup.

The Lagrangian Particle Dispersion Model (LPDM) was based on the work of Thomson (1987) and on the implementation of the model in LES by Weil et al. (2004). Here, the equation of motion for the tracer particles is

$$\frac{d\vec{x}}{dt} = \tilde{\vec{u}}(\vec{x}, t) + \vec{u}'(\vec{x}, t), \quad (5.1)$$

where $\tilde{\vec{u}}$ is the LES-resolved velocity and \vec{u}' a contribution to the particle velocity from subfilter-scale (SFS) fluctuations; \vec{u}' is modeled as a Gaussian random term of which the magnitude is determined by the SFS turbulent kinetic energy (TKE) of the Eulerian LES field. Resolved velocities and conserved properties (e.g., the liquid potential temperature θ_l and the total water content q_t) are interpolated linearly to the position of the particle; other scalars, such as the liquid water content q_l and the virtual potential temperature θ_v , are calculated using the interpolated conserved variables. For time integration, the second order Adams-Bashforth method is used. Boundary conditions are kept the same as in the LES, meaning no-slip conditions at top and bottom, and periodic boundary conditions in the horizontal directions. In all simulations, $128 \times 128 \times 80 = 1.3 \times 10^6$ particles are distributed homogeneously throughout the domain. A detailed validation of the particle model is provided in

the appendix. As is shown there, the Lagrangian particles follow the flow within the bulk of the CBL very well for a simulation of BOMEX.

5.3 DETAILED CLOUD INVESTIGATION

5.3.1 Terminology

The first approach to analyse cloud-environment interaction consists of looking into individual clouds and comparing the results of Paluch diagrams with results from particle tracking. For each of the 3 simulations, at observation times $t_{\text{obs}} = 4\text{ h}$, $t_{\text{obs}} = 5\text{ h}$ and $t_{\text{obs}} = 6\text{ h}$, the tallest cloud is selected from the cloud field. This approach is not only followed because of the importance of large clouds in the transport of air through the CBL but also because the vast majority of previous work focuses on large active clouds, allowing for a good comparison. Because these nine clouds yielded similar results, only one of them is discussed in detail here. This cloud has a cloud base at 550m and a cloud top at 1750m (which is in the middle of the inversion layer).

The construction of a Paluch diagram allows freedom in choosing a conserved variable pair. Traditionally, the total humidity q_t is chosen as one variable and is put on the y axis of the diagram. Because the y axis is easily associated with height, it is useful to plot the diagram with a downward-pointing q_t axis.

The x axis is traditionally used for a temperature scale. Which conserved temperature scale is used varies from study to study; P79 used the equivalent potential temperature θ_q , while others used, for instance, the liquid potential temperature θ_l . In the simplest approximation, θ_q and θ_l are related to each other by

$$\theta_q \approx \theta_l + \frac{L}{c_p} q_t, \quad (5.2)$$

where $L = 2.5 \times 10^6 \text{ J kg}^{-1}$ is the latent heat of vaporization and the specific heat of dry air $c_p = 1004 \text{ J kg}^{-1} \text{ K}^{-1}$. Note that because θ_l and q_t are conserved, so too is the approximated θ_q . The importance of an appropriate temperature scale is illustrated in figure 5.1. In the two top panels, the outline of a Paluch diagram is shown with (θ_l, q_t) and (θ_q, q_t) as conserved variable pairs. The area enclosed by the environmental curve and a dashed line drawn between cloud base CB_{env} and cloud top CT_{env} is where the properties of in-cloud air mostly lie. Within such an elongated shape, any uncertainty in either the measurements or in the linear fit would clearly yield large uncertainties in the intersecting points near cloud base z_{ib} and near cloud top z_{it} . However, any linear combination of θ_l and θ_q is also a conserved variable itself. Therefore, by defining an alternative temperature scale θ_α as

$$\theta_\alpha = (1 - \alpha)\theta_l + \alpha\theta_q, \quad (5.3)$$

and maximizing the area between the environmental curve and the $\text{CT}_{\text{env}}\text{-CB}_{\text{env}}$ line as a function of α , an optimal temperature scale θ_α can be found, as illustrated in

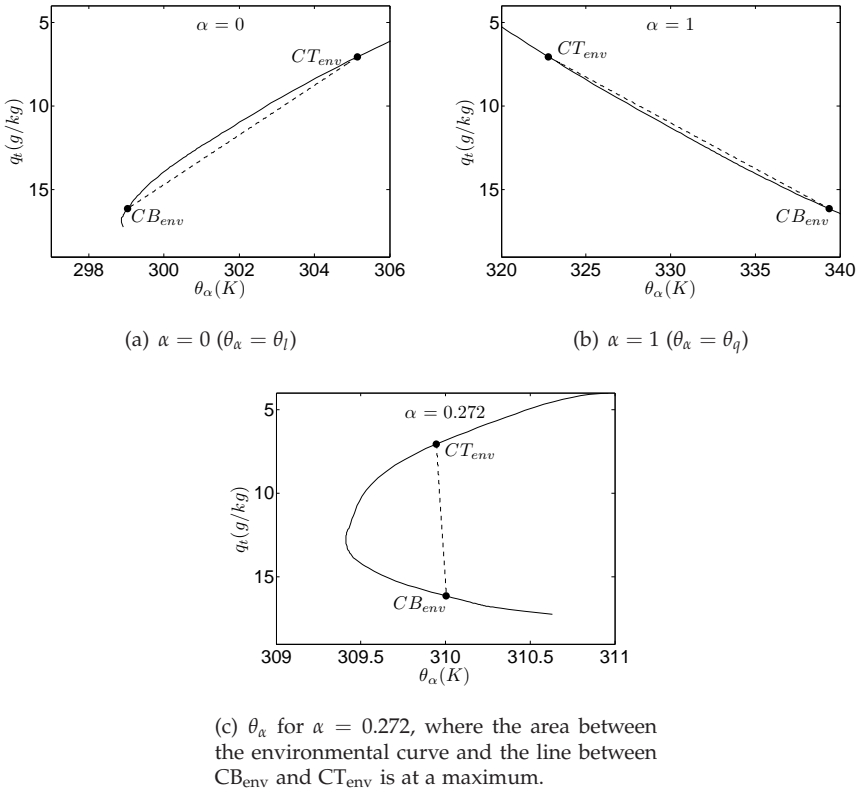


Figure 5.1: Paluch diagram for several pairs of conserved variables (θ_α, q_t) with $\theta_\alpha = (1 - \alpha)\theta_l + \alpha\theta_q$.

the third panel of figure 5.1. For this particular case, $\alpha = 0.272$ was found. It should be stressed that the choice of α is arbitrary in the sense that we do not attribute any direct physical meaning to θ_α , save for the fact that it is a conserved variable in the same sense that θ_l and θ_q are. So that we are still allowed to construct a Paluch diagram with it, any conclusion that holds in (θ_α, q_t) space should also hold in (θ_l, q_t) space. The only reason to introduce θ_α is that the graphical inspection on which the upcoming discussion relies is virtually impossible with either θ_l or θ_q as temperature scale, as is illustrated in figure 5.1.

Because Paluch diagrams are a representation of the physical world in a more abstract phase space, these diagrams can easily become rather complicated. A further complication here is the tracking of air parcels in time. In figure 5.2, four fictitious air parcels are shown, both in a cloud and in the corresponding Paluch diagram. These parcels are observed within the cloud at $t' \equiv t - t_{obs} = 0$ at height z_{obs} and are denoted as open circles in the figures. In the Paluch diagram, the en-

vironment is shown as a solid line, with squares at 200-m height intervals. Four gray crosses at the environmental curve denote (from bottom to top along the environmental curve) the in-cloud properties of cloud-base CB_{cld} (representing the properties of the inflow from the subcloud layer), the height of cloud-base CB_{env} , the observation height z_{obs} and cloud-top CT_{env} are marked with gray crosses on the environmental curve. The dashed line representing the best fit in phase space through the parcels at t_{obs} crosses the environmental curve at z_{it} and z_{ib} . The location of z_{ib} can be interpreted as the average of the lower part of sources. If the presence of subcloud-layer air is dominating the sampling, z_{ib} lies near CB_{cld} . Similarly, z_{it} represents the upper part of the sources. If cloud mixing is modeled as mixing between two sources, these sources lie at z_{it} and z_{ib} . The source at z_{ib} is then associated with inflow from the subcloud layer, and z_{it} with the source of entrained air. This is the main assumption underlying the analysis of the Paluch diagram, and it is usually justified by the high correlation between the linear fit and the properties of the air parcels. As TB91 showed, this only holds if either buoyancy sorting does not apply or if the regions allowed by buoyancy sorting are sufficiently large.

Because the particles in the LPDM representing the air parcels can be tracked backward in time, the position of the parcels before observation time $t' = 0$ can now also be plotted in the Paluch diagram. For some time $t' < 0$, the parcels are shown as solid dots. Before entering the cloud, the fictitious parcels in figure 5.2 (of which one originates from the subcloud layer, two from around observation level, and one from above cloud top) have the same properties as the environment at their respective heights. The aim of this paper is to study the origins of air entrained from the cloud layer into the cloud. Thus, in the calculation of the average height of the parcels the subcloud layer must be excluded. This average height of parcels that reside above cloud base is indicated by a large gray dot on the environmental curve and denoted by $\langle z \rangle_p(t')$.

For quick reference, an overview of the definitions used in this section is given in table 5.1.

5.3.2 Results and interpretation

In figure 5.3 Paluch diagrams of the simulations are shown for four observation levels z_{obs} within the cloud. Additionally, the TB91 buoyancy-sorting regions are enclosed by gray lines denoting the saturation level q_s , a line from cloud base to observation level and a gray area where $\theta_v < \theta_{v,\text{env}}$. Note that the latter is sharply influenced by the presence of liquid water.

Assuming buoyancy sorting, all points below the $CB_{\text{cld}}/z_{\text{obs}}$ line come from below and should be positively buoyant; all points above this line come from above and should be negatively buoyant. Note that because of the use of θ_α the allowed regions are (optically) significantly larger than in the θ_q plots used originally in TB91.

In all figures, the vast majority of points come from below and are positively buoyant. However, a few appear to come from above, while from $z_{\text{obs}} = 1000\text{m}$

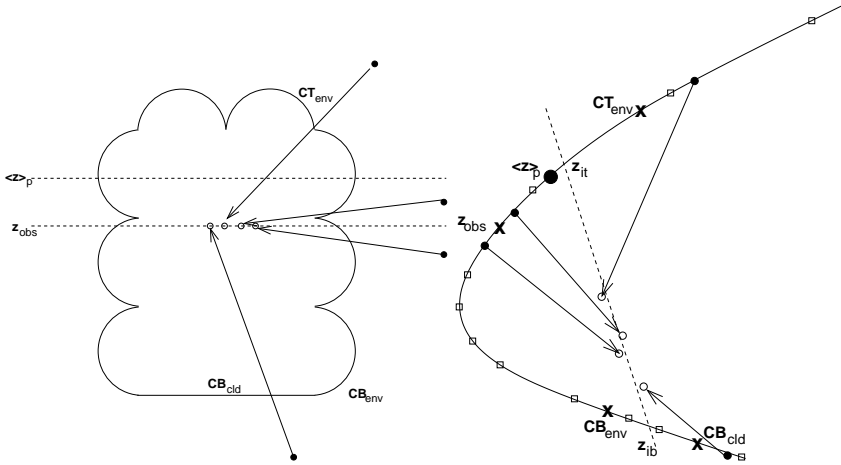


Figure 5.2: (left) Conceptual picture of air parcels moving through a cloud and (right) through the corresponding Paluch diagram. Crosses on the environmental line denote (top to bottom) cloud top (CT_{env}), observation height (z_{obs}), cloud base (CB_{env}) and the average in-cloud cloud-base properties CB_{cld} . This is the average of all air parcels in the cloud at $t = t_{obs}$ and $z = z_{cb}$. Squares denote intervals of 200m. Circles signify parcels in the cloud at $t = t_{obs}$ and $z = z_{obs}$. The dashed line is a best linear fit through the parcels at $t = t_{obs}$ and $z = z_{obs}$, and crosses the environmental curve at $z = z_{ib}$ and at $z = z_{it}$. The average height of the parcels residing in the cloud layer is marked with the large dot labeled $\langle z \rangle_p$.

Table 5.1: Summary of the key variables used in section 5.3.

Variable	Description
θ_α	$(1 - \alpha)\theta_l + \alpha\theta_q$; optimized temperature scale
α	0.272; optimization parameter in θ_α
CB_{env}	Environmental properties at cloud-base height
CB_{cld}	In-cloud properties at cloud-base height
CT_{env}	Environmental properties at cloud-top height
t_{obs}	Moment of observation
t'	$t - t_{obs}$; time relative to observation time
z_{obs}	Height of observation
z_{ib}	Lower source level inferred from Paluch diagram
z_{it}	Upper source level inferred from Paluch diagram
$\langle z \rangle_p(t')$	Average height of air parcels residing above cloud base
z_s	$\langle z \rangle_p(t' = -1800\text{ s})$; average source level of cloud-layer parcels

upward, the parcels of which almost all water has been evaporated are clearly negatively buoyant despite coming from below. This can be either explained by the buoyancy reduction due to evaporation itself, or because these parcels overshot their buoyancy-sorting level. This has also been observed by for instance Neggers et al. (2002). Clearly, for $z_{\text{obs}} = 1600$ m, the cloud has reached the inversion layer and all parcels are in such an overshoot. This is also the only height where two-point mixing is clearly not valid, because the points are no longer distributed along a line. For all other heights, the points are distributed along a line with a tendency stronger than can be explained by buoyancy sorting alone.

For all heights, the inferred upper-source-level z_{it} lies around or slightly above observation level. It should be noted that the inferred upper source levels are markedly different from an orthodox cloud-top entrainment view, where the upper-source-level z_{it} should be located at cloud top, and the lower-source-level z_{ib} at cloud base for all observation heights. Within the framework of cloud-top entrainment, this is usually explained by air being entrained in an earlier life stage of the cloud when the ascending cloud top of the growing cloud passed the observation level. However, the increase in height of the lower-source-level z_{ib} (reaching 650 m at $z_{\text{obs}} = 1600$ m and only equaling CB_{env} in passing at $z_{\text{obs}} = 1300$ m) also hints at lateral entrainment. This increase of z_{ib} has also been observed by Lamontagne and Telford (1983).

Blyth et al. (1988) plotted the source level z_{it} as a function of observation level z_{obs} . In figure 5.4, their result is shown, accompanied by the same analysis of the current data. Both results display an upper source level that lies at or somewhat above observation level. For higher altitudes, z_{it} is especially higher than z_{obs} ; this was associated by Blyth (1993) with entrainment induced by the recirculating vortex at cloud top. In any case, the results from simulations of BOMEX look similar to the observations in Blyth et al. (1988) of much deeper cumuli (CT up to 6 km), regardless of the interpretation of z_{it} .

In figure 5.5, the evolution of particles located at $z_{\text{obs}} = 1000$ m at $t' = 0$ s is shown at previous times. Clearly, most particles present in the cloud layer before $t' = -600$ s are concentrated around or below z_{obs} . Indeed, the average level of cloud-layer particles $\langle z \rangle_p(t' = -600 \text{ s})$ lies below both z_{obs} and z_{it} in (q_t, θ_α) phase space. This suggests that at least for this height, the inferred upper-source-level z_{it} overestimates the true source level of the in-cloud air.

To get a better idea of the location of the particles, the probability density function (PDF) of the height of the particles is shown in figure 5.6. Two processes are clearly visible here. The particles in the subcloud layer (below 550 m) are initially homogeneously distributed ($t' = -3600$ s), then start to congregate near the surface ($t' = -1800$ s) and finally rise into the cloud in the 10 minutes before t_{obs} . Irrespective of this subcloud process, the PDF in the cloud layer only changes due to the influence of the cloud towards z_{obs} in the final ten minutes before observation time; going further backwards in time, the PDF is broadened due to some turbulent diffusion. This could be expected, because the cloud has a typical lifetime of less than half an hour. Therefore, we define the location of cloud-layer particles $\langle z \rangle_p$ at

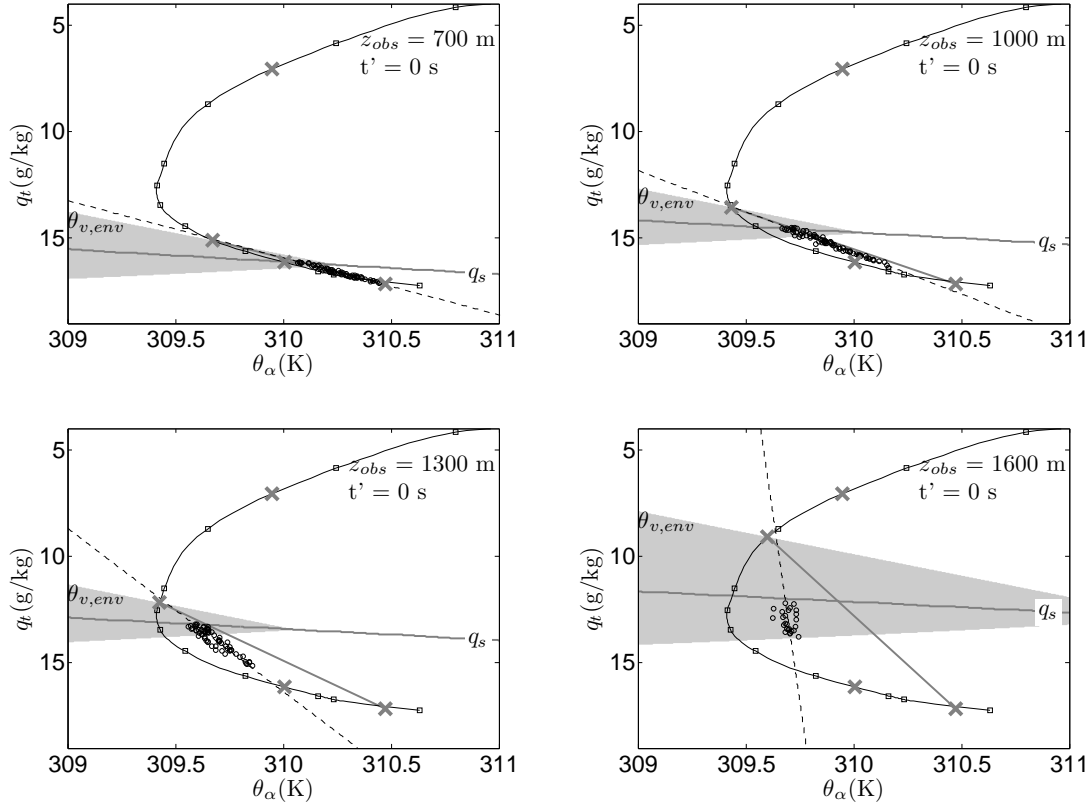


Figure 5.3: Paluch diagram at observation level $z_{obs} = 700$ m, 1000 m, 1300 m and 1600 m, respectively. The allowed regions of buoyancy sorting of TB91 are enclosed by one gray line that denotes the saturation level q_s and another gray line between CB_{cld} and z_{obs} . In the shaded area, $\theta_v < \theta_{v,env}$. See figure 5.2 for explanation of the other symbols.

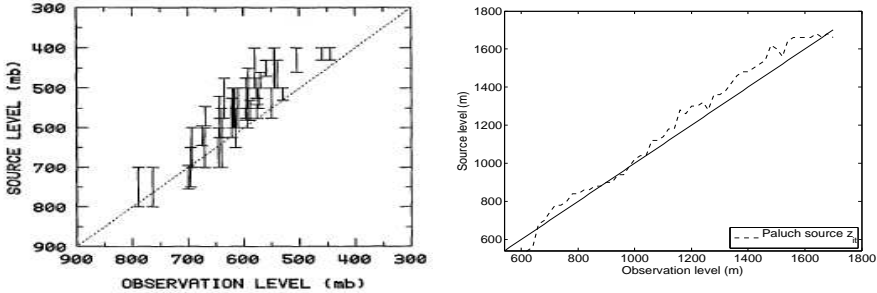


Figure 5.4: The upper-source-level z_{it} as a function of observation height z_{obs} . (left) Observational results for Montana cumuli from Blyth et al. (1988); (right) current LES results of BOMEX.

$t' = -1800$ s as the source-level z_s of the air; the cloud has not yet entrained the particle, and the low cloud fraction of around 10% makes it highly unlikely that earlier clouds are still influencing the trajectory of the particles. In calculation of z_s , only the particles have been taken into account that remain above cloud base during the entire period between $t' = -1800$ s and $t' = 0$ s. This way, biases due to spatial fluctuations in cloud-base height or recirculation from the cloud layer into the subcloud layer, for example, can be eliminated.

Looking at the distribution of cloud-layer particles in figure 5.6, it is clear that hardly anything originates from more than 200 m above z_{obs} . The cloud influences the environment and particles move toward z_{obs} only in the 5 minutes preceding the observation time.

The two source levels z_s and z_{it} can now be plotted against z_{obs} (figure 5.7). For higher observation levels, a clear discrepancy can here be observed between the source-level z_{it} (dashed line) inferred from the Paluch analysis and the origin z_s of the particles (solid line).

5.4 ENSEMBLE AVERAGING OVER THE CLOUD FIELD

The previous section focused on the inspection of a single cloud, which is useful for comparisons between this study and earlier observations. However, the rich dataset of LES can now be used to obtain source heights averaged over a very large number of clouds. This reduces the influence of stochastic events and advances the results towards a more statistical representation of the cloud field. The difference between this approach and a bulk parameterization should be stressed: the aim here is to understand the physical properties of the individual clouds by careful conditional sampling and rescaling of the clouds, not to represent the entire field as a (not necessarily physically realistic) bulk cloud. As a consequence, any cloud-top mixing should still be visible in the results.

Taking a representative average over the entire ensemble of clouds has to be

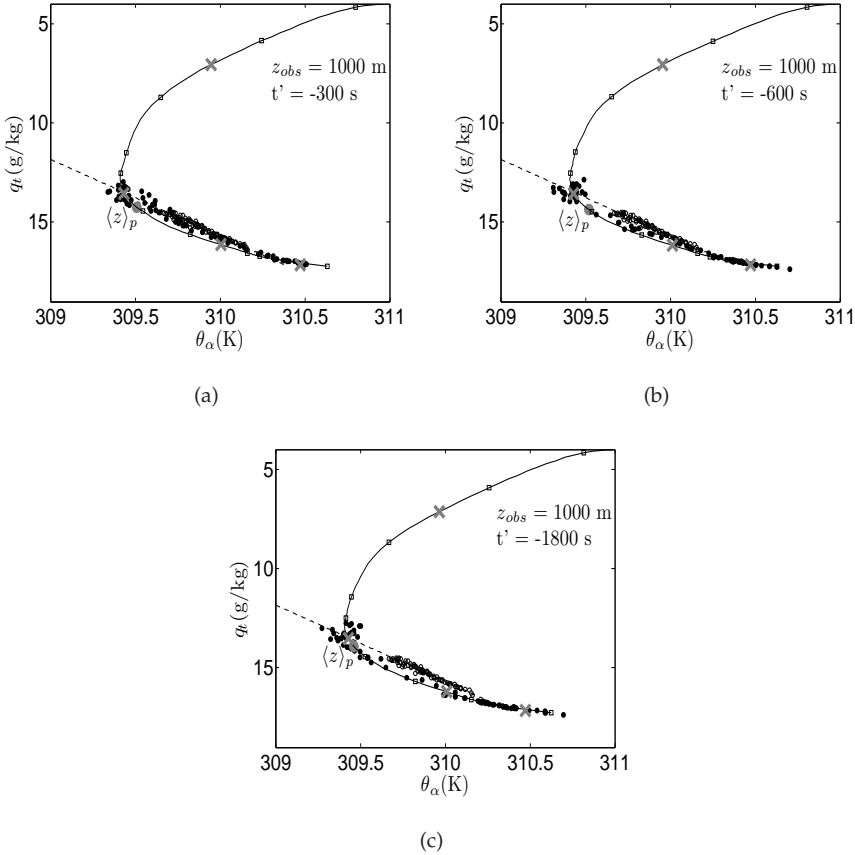


Figure 5.5: Paluch diagram evolving in time for $z_{obs} = 1000$ m. Instances where a) $t' = -300$ s, b) $t' = -600$ s and c) $t' = -1800$ s. See figure 5.2 for explanation of the symbols.

done with some caution. For instance, averaging over an ensemble of clouds of different sizes requires an accurate definition of the cloud size; the dynamics of a small chunk broken from a cloud can be expected to differ from a large cloud topping a thermal. Another point is that turbulent diffusion at cloud edge might cause many particles entering and immediately leaving a cloud without causing significant mixing.

To take these effects into account, results are split between ensembles over all particles that reach the cloud and particles that reach the cloud core (i.e., $\theta_v > \theta_{v,env}$) at some point during their residence in the cloud. To remove passive clouds and dissipating chunks from the ensemble, only clouds with a height of at least 300 m

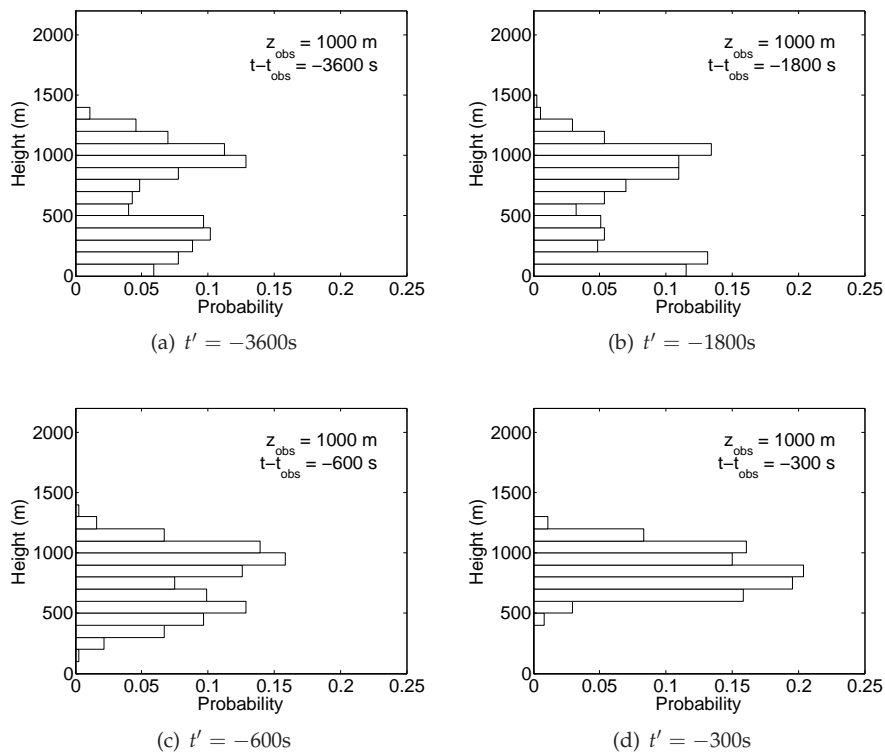


Figure 5.6: PDF of the height of the particles evolving in time for $z_{\text{obs}} = 1000$ m.

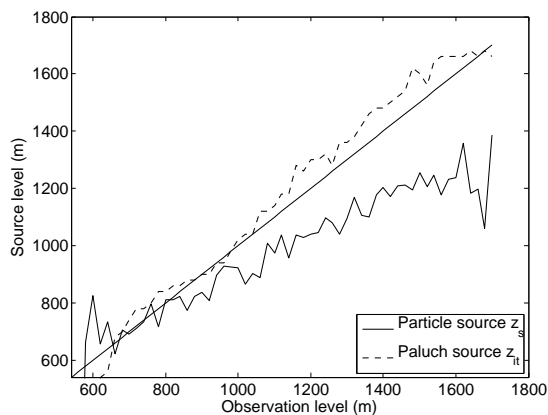


Figure 5.7: Source level as a function of observation height, following Paluch analysis (dashed line) and the source level z_s as defined in the text (solid line).

are taken into account. To see whether clouds reaching the inversion layer have different properties, a distinction is made between all clouds larger than 300 m and clouds larger than 1000 m.

A subtle point is the exact definition of cloud height for normalizing the height where a particle enters or leaves a cloud. This height $h(t)$, defined as the height difference between the highest and the lowest level of adjacent gridpoints where $q_l > 0$, can vary strongly in time between the moment when a parcel enters the cloud t_{in} , the moment of observation within the cloud t_{obs} , and the moment when the parcel leaves the cloud t_{out} . As a guideline, the maximum height $h_{max} \equiv \max(h(t_{in} : t_{obs}))$ is taken of the cloud between the time of entry t_{in} and the moment of interest, yielding a normalized height $z'(t) = (z(t) - z_{cb})/h_{max}$, where z_{cb} is the height of the cloud base. The justification of this choice is that the history of the cloud is relevant for the position of a particle, but the future of the cloud is not. The relative entry level is thus defined as $z'_{in} = (z(t_{in}) - z_{cb})/h_{in}$, and the relative exit level as $z'_{out} = (z(t_{out}) - z_{cb})/h_{max}$. With these definitions, cloud-top entrainment results in a high value for the relative entry level z'_{in} , even in the case of an ascending cloud. This definition also results in a relative exit level that is unbiased by chunks breaking from the main cloud: if, for instance, a chunk breaks from the cloud at midlevel and then dissipates, thus leaving the particle in the environment, z'_{out} would be equal to 0.5, which is reasonable looking from the perspective of the main cloud. For quick reference, an overview of the definitions used in this section is given in table 5.2.

In figure 5.8, the fraction of particles entering or leaving at a relative height z' are shown for all four sampling conditions: 1) clouds larger than 300 m; 2) clouds larger than 1000 m; 3) particles reaching the positively buoyant core of clouds that are larger than 300 m; 4) particles reaching the core of clouds larger than 1000 m. The overall look of the results is quite similar for all conditions: the inflow peaks sharply at cloud base and there exists a region between $z' = 0.2$ and $z' = 0.6$ where the inflow approximately balances the outflow, and the cloud-environment interaction is constant in height. In the top part of the cloud, inflow decreases, but outflow does not. Because z'_{in} is scaled with the total cloud height at that moment, this strongly suggests an absence of cloud-top mixing. Note that the rescaling of clouds also eliminates effects of reduction of cloud fraction with height; only the geometry of individual clouds (in the sense of a cone-like shape, e.g.) could still have an influence.

Although figure 5.8 shows that entrainment and detrainment are balanced at mid-cloud, there are also region of net in- or outflow. Most pronounced is the large outlet of air in the cloud-top region for the largest clouds, which can be associated with the intrusion in the inversion layer and a resulting increased (anvil-like) outflow. Another interesting difference is the net exchange rate in the midlayer of the cloud: the small clouds display more particles leaving the cloud than entering it, whereas the largest clouds, and especially their cores, are net entraining air from the environment. This is consistent with Neggers et al. (2003b) who found a mass flux increasing with height for large clouds.

Table 5.2: Summary of the key variables used in section 5.4.

Variable	Description
t_{obs}	Moment of observation
t_{in}	Moment the particle enters the cloud
t_{out}	Moment the particle leaves the cloud
$h(t)$	cloud height
h_{max}	$\max(h(t_{\text{in}} : t_{\text{obs}}))$; maximum height of the cloud between entry time and observation time
$z'(t)$	$(z(t) - z_{\text{cb}})/h_{\text{max}}$; relative height of the particle with respect to the cloud
z'_{in}	$(z(t_{\text{in}}) - z_{\text{cb}})/h_{\text{in}}$; relative height of the particle at entry time
z'_{out}	$(z(t_{\text{out}}) - z_{\text{cb}})/h_{\text{max}}$; relative height of the particle when leaving the cloud
\bar{z}	Average height of a set of particles
\bar{z}^+	Average height of all particles with $z > \bar{z}$
\bar{z}^-	Average height of all particles with $z < \bar{z}$
Source level	Particle height at $t = t_{\text{in}} - 1800$ s
Entry level	Particle height at $t = t_{\text{in}}$
Observation level	Particle height at $t = t_{\text{obs}}$
Exit level	Particle height at $t = t_{\text{out}}$
Destination level	Particle height at $t = t_{\text{out}} + 1800$ s

The equivalent of figure 5.7 (i.e., observation level versus entrance level) in the field-averaged approach can now give more conclusive evidence on the role of lateral and cloud-top entrainment. As is illustrated schematically in figure 5.9, cloud-top entrainment will result in emphasis on the top horizontal bar. Because the definition of z' accounts for ascending cloud-tops, any signal at or below the diagonal must be due to lateral mixing, but for the lower horizontal bar, which signifies the inflow from the subcloud layer. As can be seen in figure 5.10, no cloud-top mixing is observed anywhere in the cloud field. Aside from an expected strong inflow at cloud base, lateral entrainment is clearly dominating cloud mixing. For smaller clouds, some air can be seen to come from higher levels but not specifically from cloud top. Moreover, this band of in-cloud downdrafts is relatively much smaller for large clouds, and can best be explained by the in-cloud turbulence. The complementary graph of figure 5.10 –the relative vertical position where air leaves the cloud as a function of observation level– is shown in figure 5.11. Here, it can be seen that most detrainment occurs at or slightly above observation level. As in figure 5.8, a relatively large outlet of air is observed around $z'_{\text{out}} = 0.8$, especially for the cloud core of large clouds. Rather unsurprisingly, hardly any particle observed

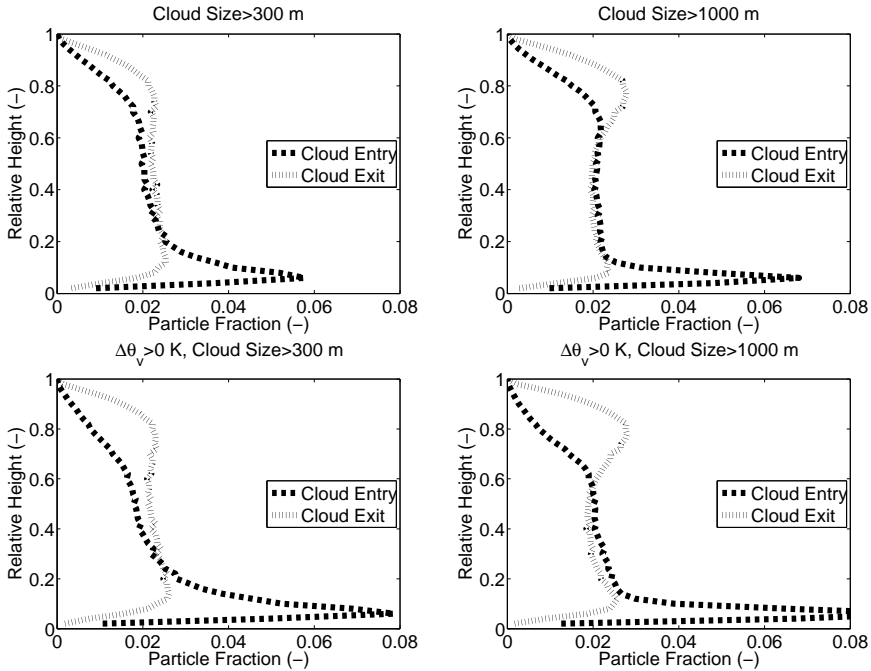


Figure 5.8: Relative number of particles entering (dashed line) or leaving (dotted line) the cloud as a function of the relative height h for clouds of at least (left) 300 m or (right) 1000 m. The top graphs include all events of entering/leaving a cloud; the results in the bottom figures are conditionally sampled over particles that reach the cloud core (i.e., are positively buoyant at some time between entering and leaving the cloud).

in the cloud core leaves the cloud at a lower level.

The role of the cloud on the dynamics of the cloud layer can not only be felt within the cloud itself but also in its immediate surroundings. To illustrate this, the average height \bar{z} of particles entering large clouds at 1200 m is shown in figure 5.12 as a function of time before and after the moment of entry $t = t_{in}$. The same is done in figure 5.13 for particles leaving the cloud at 1200 m with reference to exit time $t = t_{out}$. While some air is indeed coming from above cloud top and descends 500 m in the 250 s before entering, these downdrafts are extremely rare; half an hour before entering the average height of the particles \bar{z} is 1050 m, and the average height \bar{z}^+ of all particles above \bar{z} is 1200 m, that is, equal to entrance height.

For the outflow the picture is somewhat different: a small portion of air rises on (possibly after reentraining into the cloud), but the average height clearly decreases after the detrainment event with 0.2 m s^{-1} in the first 500 s. Because the detrainment happens far below cloud top, this suggests that the downward motion can

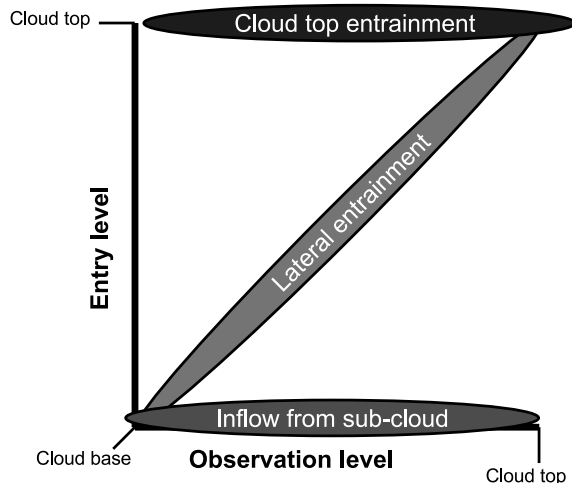


Figure 5.9: Conceptual picture of an observation- vs. source-level diagram. Inflow from the subcloud layer will show up at the base of the graph, cloud-top entrainment at the top and the diagonal signifies lateral entrainment.

be associated with the descending shell (see Heus and Jonker, 2008b; Jonker et al., 2008).

5.5 NET VERTICAL TRANSPORT DUE TO CLOUDS

As discussed in section 5.4, the influence of clouds on the vertical transport of air is not limited to flow within the cloud itself. To give an overall view of the vertical transport due to the cloud, three stages are distinguished in the residence of a particle in the (near vicinity of the) cloud: 1) the 30 minutes before entering the cloud, 2) the time between entering and leaving the cloud, and 3) the 30 minutes after having left the cloud. This is done by defining, apart from the entry level and the exit level, the source level as the height of a parcel of air 30 minutes before having entered the cloud and the destination level as the height of a parcel of air 30 minutes after having left the cloud. As shown in section 5.3, this half-hour time window is long enough to include all interactions of the particle with the cloud while excluding interaction with later clouds.

The behavior of air before entering the cloud, during residence in the cloud and after having left the cloud is shown in figure 5.14. Because the tallest clouds have nearly identical cloudtops between 1600 and 1800 m, their heights can be shown in absolute numbers, allowing for inclusion of the sub-cloud layer in the discussion. Looking at figure 5.14(a), most air clearly enters the cloud at cloud base coming from the subcloud layer as expected; air that enters the cloud laterally

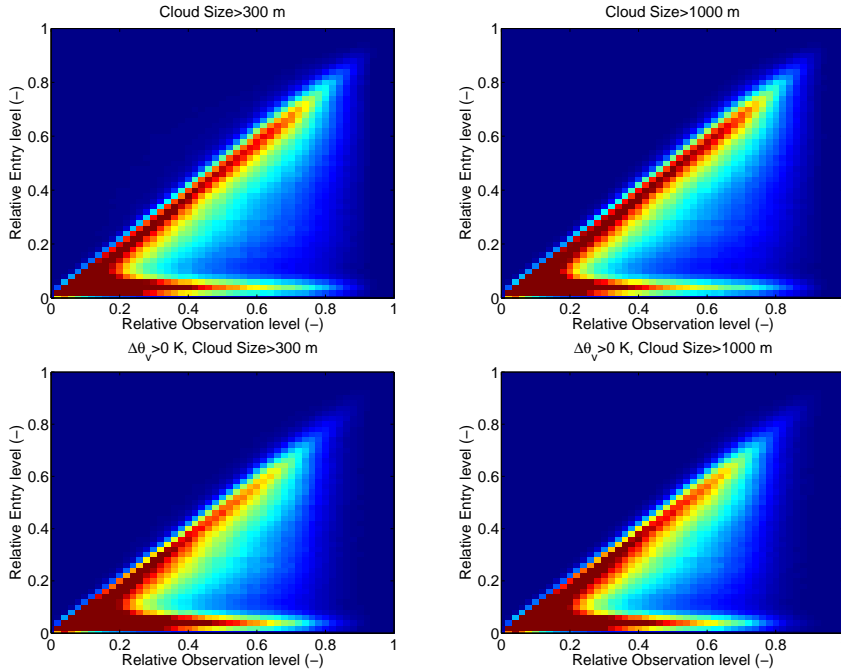


Figure 5.10: The relative height where particles entered the cloud as a function of relative observation level. Distinction is made between clouds with a height of at least (left) 300 m or (right) 1000 m. In the bottom panels the particles are furthermore conditionally sampled on their presence in the cloud core; that is, they had to be positively buoyant at some time between entering and leaving the cloud.

mostly originates from entry level height. No clear evidence of descending air (be it by the recirculation vortex or the subsiding shell) can be found in this figure. A minor fraction of the entrained air originates from other (mainly lower) levels; this is probably air that has left and then immediately reentered the cloud. Once air has entered the cloud (depicted in figure 5.14(b)), it is likely to leave the cloud again at a level equal to or higher than entry level. A cloud core consisting of subcloud-layer air is clearly visible in the form of a dark vertical band at an entry level of 550 m. Penetrative in-cloud downdrafts would show in the lower-right triangle of the figure but are not observed here.

In contrast with the time before entering the cloud, the fingerprint of the subsiding shell is clearly visible for air that has left the cloud as the dark area below the diagonal in figure 5.14(c). The appearance of this dark area for all exit levels suggests that this downdraft is indeed due to the subsiding shell, and not due to the recirculation vortex that would mark only the area around cloud top. The cloud-top region around 1500 m shows only a somewhat larger downdraft population, while

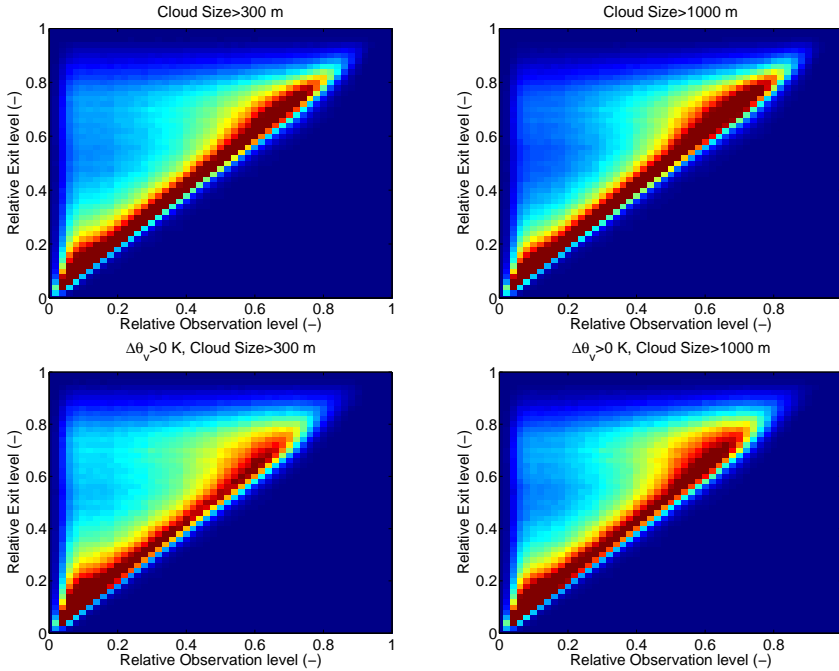


Figure 5.11: The relative height where particles leave the cloud as a function of relative observation level. Distinction is made between clouds with a height of at least (left) 300 m or (right) 1000 m and between the (top) entire cloud and the (bottom) cloud core.

the particle descent remains around 200 m, similar to particles exiting lower in the cloud. It is interesting to note that as a result in the lowest part of the cloud layer the subsiding shell enhances mixing of cloud-layer air into the sub-cloud layer.

The total net vertical transport by the cloud and its surroundings is the resultant of the three graphs in figure 5.14, shown in figure 5.15, where the destination level is plotted against the source level. Clearly, it can be seen here that the downward motion of air having left the cloud is strong enough to result in a net downward displacement for a significant number of air parcels. The fact that this downward transport is equally strong at all heights shows that the role of cloud-top-driven downflow is subordinate in the dynamics of shallow cumulus clouds.

5.6 CONCLUSIONS

In this paper the origins of in-cloud air has been studied for shallow cumulus clouds in LES by two different methods: Paluch diagrams and Lagrangian tracer particles. From the Paluch diagrams an inferred source level around observation height was

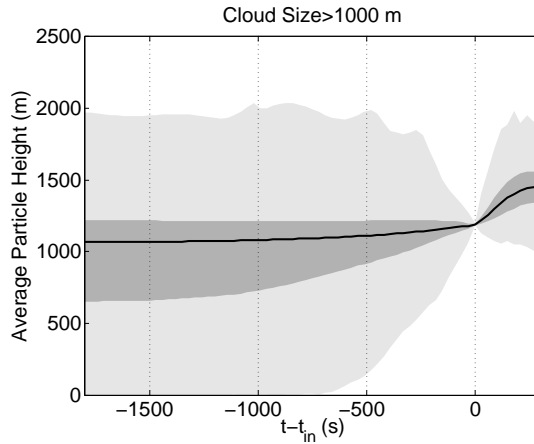


Figure 5.12: Average height as a function of time of all particles entering kilometer-sized clouds at 1200 m. For $t < t_{in}$, particles are located in the environment; for $t > t_{in}$, particles are located within the cloud. The line denotes the average height \bar{z} of all particles. The edges between the dark and light gray area are the average of all particles below \bar{z} , indicated in the text by \bar{z}^- , and particles above \bar{z} , indicated by \bar{z}^+ . The light gray area envelops the entire particle distribution.

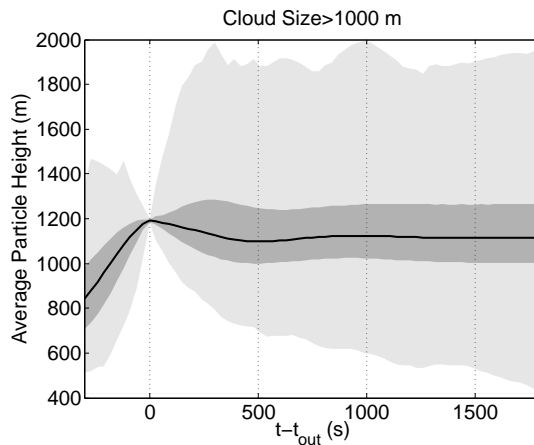


Figure 5.13: Average height as a function of time of all particles having left the kilometer-sized clouds at 1200 m. For $t < t_{out}$, particles are located in the cloud; for $t > t_{in}$, particles are located within the environment. See figure 5.12 for further explanation.

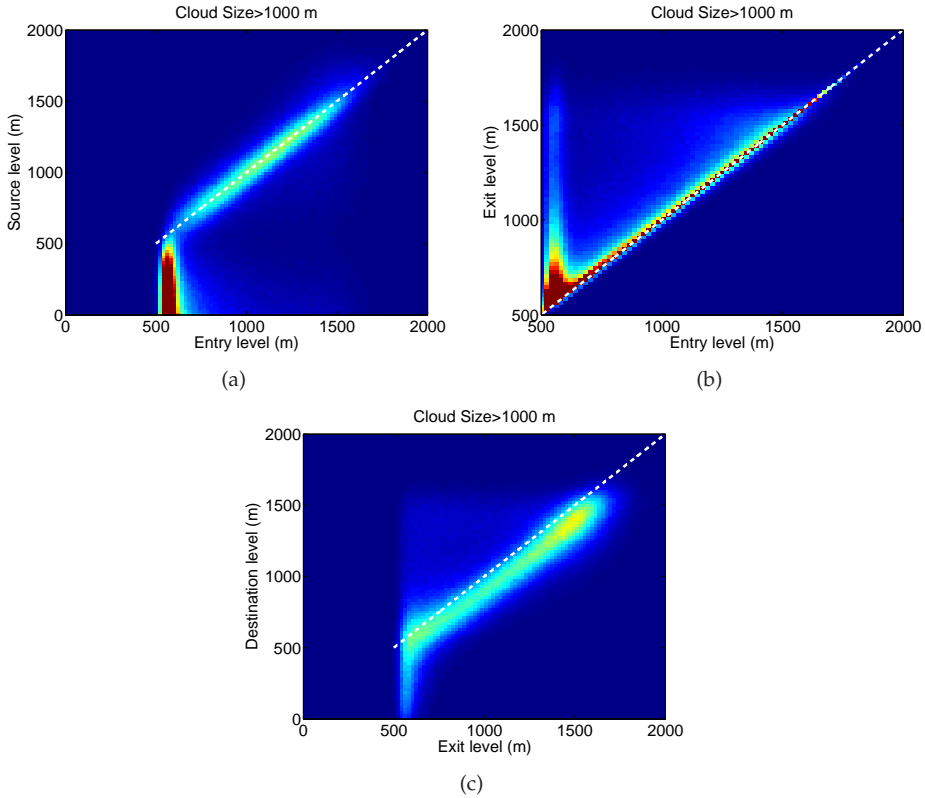


Figure 5.14: The effect of the three stages on the cloud-environment interaction for clouds larger than 1000 m. (a) Source level versus entry level, (b) exit level versus entry level and (c) destination level versus exit level.

obtained, which is also often found in the literature. However, the source level found by explicit backtracking was significantly lower than observation level. Both in the analysis of individual clouds as well as in ensemble averaging of the entire cloud field no evidence could be found for significant cloud-top mixing.

Why the Paluch diagrams overpredict the source level and why they correlate so well with two-point mixing remains not entirely clear. Most of the inherent correlation between the pair of conserved variables has been eliminated by the use of the optically optimized θ_α temperature scale. The use of θ_α also widened the allowed regions of buoyancy sorting from TB91, which suggests that buoyancy sorting alone cannot explain the linear distribution of points in the Paluch diagram. One possible explanation might be found in the pathlines within the diagram of diluting parcels in a laterally entraining cloud; lateral entrainment tends to pull already diluted air towards the line between the properties of less diluted air and the properties of

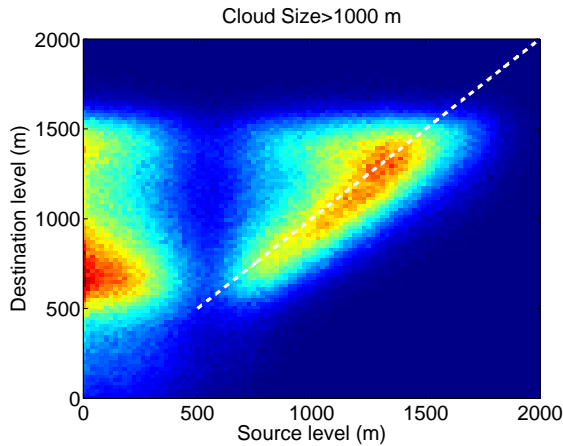


Figure 5.15: The destination level versus the source level for clouds larger than 1000 m.

observation level. Another reason for the overprediction of the source level might be that the inferred source level is calculated in phase space, thus giving too much weight to air parcels with a large deviation from the mean temperature or moisture – most prominently, air coming from above the inversion.

The conceptual picture of a cloud emerging from this study is schematically shown in figure 5.16. A cloud core consisting of air originating from the subcloud layer is recognizable throughout the entire cloud and is constantly diluted by lateral mixing. Part of the laterally entrained air is lifted to higher levels, but another part leaves the cloud at levels comparable with the source level. This is in agreement with the results of Kuang and Bretherton (2006), for example, who found hardly any undiluted parcels above cloud base. Also, their observed similarity between deep and shallow cumulus is supported by the similarity in figure 5.4 between our Paluch diagrams and the ones found for much deeper cumuli by Blyth et al. (1988). The specific scaling of the entrainment height showed no evidence in favor of entrainment due to the ascending cloud top, as discussed in Blyth (1993) and Zhao and Austin (2005b), but it should be noted that life cycle effects like pulsating growth of cumulus (e.g., as discussed in French et al. (1999) and Zhao and Austin (2005b)) have not been taken into account here and demand further investigation. The subsidence due to evaporative cooling after detrainment from the cloud ensures that some of this air is net transported downwards during its stay in or near the cloud. It is notable that air entrained into the cloud appears to be less affected by the subsiding shell than the air detrained from the cloud. This is consistent with the results of Heus and Jonker (2008b) and Jonker et al. (2008) who found a shell induced by evaporation of detrained air parcels, while environmental air can only be transported downwards if dragged along with the descending shell.

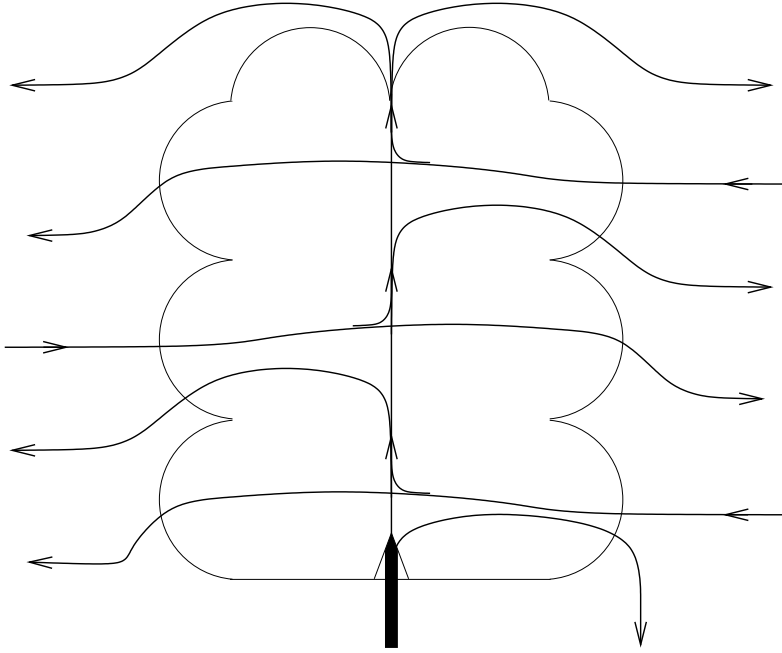


Figure 5.16: A conceptual picture of cumulus cloud mixing following from this study.

APPENDIX 5.A VALIDATION OF TRACER PARTICLES IN CUMULUS FLOW

The used LPDM has been tested in the clear CBL (Weil et al., 2004) but not in cumulus topped boundary layers. We define two criteria for validation of the LPDM: 1) a homogeneous particle distribution remains homogeneous in incompressible flow and 2) Lagrangian and Eulerian statistics must converge for a sufficient number of particles.

5.A.1 Homogeneity of the distribution

The particle distribution at $t = 7h$ (i.e., 4h after initialization of the particles) has been investigated with regard to homogeneity of the particle distribution. The initial focus is on the particle density as a function of height, which is normalized by the total number of particles divided by the number of bins, meaning that the expected value of this function is 1 for all heights.

In figure 5.17 it can be seen that for a large part of the domain, this expectation is met both for particles advected with (dashed line) and without SFS diffusion (dotted line). However, the amount of particles in the surface layer exceeds the average by

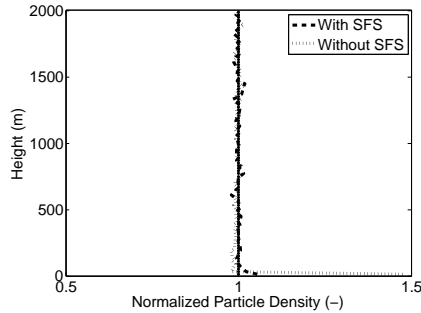


Figure 5.17: The normalized particle density at $t = 7$ h as function of height for a simulation with (dashed line) and without (dotted line) SFS diffusion.

50% when the SFS scheme is turned off. This is enough to drain a significant amount of particles from the subcloud layer. This behavior could be expected because in the surface layer, the influence of subgrid processes is much more significant than in the bulk of the domain. With the particle SFS scheme turned on, the excess is reduced to a few percent only. Because this effect is rather small and the field of interest of this study lies far away from the surface, it is deemed to be insignificant for this study; it should however be taken into consideration in studies of the surface layer.

The homogeneity of the distribution can also be validated by comparing the cloud fraction observed from both the Eulerian and the Lagrangian viewpoints. This is not only of interest because clouds are the topic of interest of this study, but also because clouds are most likely to be the subject of inhomogeneities, as they represent the most turbulent structures of the domain. The cloud fraction as function of height (figure 5.18) shows a general agreement between Lagrangian (circles) and Eulerian (dashed line) statistics, but for the cloud fraction at cloud base, where the peak in cloud fraction is undersampled in Eulerian statistics.

5.A.2 Comparison between Eulerian and Lagrangian statistics

If the massless particles are both well distributed and follow the flow correctly, averages of thermodynamical quantities as seen from a Lagrangian point of view should be comparable with the averages taken from the Eulerian viewpoint. In particular, the particle velocity is of interest here: This is calculated more or less autonomously from the LES velocity, but these two must be identical if the particles do follow the flow.

In figure 5.19, the mean sum of the variances of the resolved velocities and the SFS-TKE is plotted as a function of height from both the Eulerian and the Lagrangian viewpoints. While the SFS-TKE agrees very well, the Lagrangian-resolved variance is slightly lower than the Eulerian version. This is due the calculation

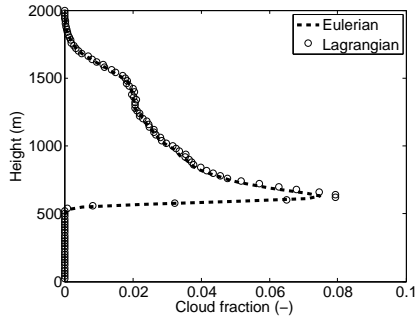


Figure 5.18: The cloud fraction between $t = 6\text{ h}50\text{ m}$ and $t = 7\text{ h}$ as a function of height according to Eulerian (dashed line) and Lagrangian (circles) statistics.

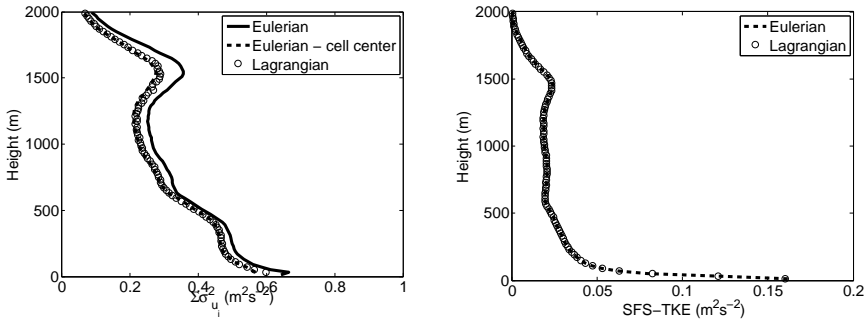


Figure 5.19: The slab averaged sum of variance of the (left) resolved velocities and the (right) subfilter-scale turbulent kinetic energy between $t = 6\text{ h}50\text{ m}$ and $t = 7\text{ h}$ as function of height according to Eulerian (solid line) and Lagrangian (circles) statistics. For the resolved variance, the dashed line denotes Eulerian statistics after interpolation of the velocities to cell center.

of variances using interpolated velocities (as is done for the Lagrangian statistics), which results in decreased variance. If the same approach is taken in the Eulerian statistics (see the dashed line in figure 5.19), the two approaches again agree. While it is important for the SFS parameterization to calculate the variance correctly, this difference in interpolation does not influence the dynamics of the particles very much, because the dependency on the variance of the SFS contribution in the LPDM is much smaller. This is illustrated with the agreement in SFS-TKE between Eulerian and Lagrangian statistics.

Finally, in figure 5.20, the in-cloud vertical velocity is shown. Here, Lagrangian statistics yield generally a slightly lower value than Eulerian statistics do. This can be explained (similar to the interpretation of figure 5.18) by the fact that the particles

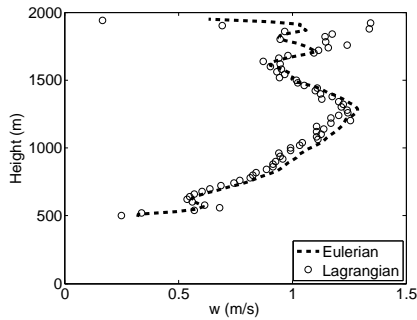


Figure 5.20: In-cloud average of w between $t = 6$ h50 m and $t = 7$ h, using Eulerian (dashed line) or Lagrangian (circles) statistics.

better sample the region near the edge of a cloud than the fixed Eulerian grid can.

To summarize, the LPDM appears to meet the criteria of a homogeneous distribution and of reliable statistics very well within the bulk of the domain and can be used with confidence for the purposes of this study.

CHAPTER 6: A STATISTICAL APPROACH TO THE LIFE-CYCLE ANALYSIS OF CUMULUS CLOUDS SELECTED IN A VIRTUAL REALITY ENVIRONMENT

In this study a new method is developed to investigate the entire life cycle of shallow cumulus clouds in large-eddy simulations. Although trained observers have no problem in distinguishing the different lifestages of a cloud, this process proves difficult to automate, because cloud-splitting and cloud-merging events complicate the distinction between a single system divided in several cloudy parts and two independent systems that collided. Because the human perception is well equipped to capture and to make sense of these time-dependent three-dimensional features, a combination of automated constraints and human inspection in a 3D virtual reality environment is used to select clouds that are exemplary in their behavior throughout their entire lifespan. The considerable number of selected clouds warrants reliable statistics of cloud properties conditioned on the phase in their life cycle. The most dominant feature in this statistical life-cycle analysis is the pulsating growth that is present throughout the entire life time of the cloud. The pulses are a self-sustained phenomenon, driven by a balance between buoyancy and horizontal convergence of dry air. The convection inhibition just above cloud base plays a crucial role as a barrier for the cloud to overcome in its infancy stage, and as a buffer region later on, ensuring a steady supply of buoyancy into the cloud.

Every silver lining has a cloud.

THE SUPERNATURALS

6.1 INTRODUCTION

The turbulent behavior and transient nature of cumulus clouds makes them a challenging topic of study. Due to heavy in-cloud turbulence, a small but systematic signal can easily be hidden among large random fluctuations. Furthermore, when averaged over the entire life time of a cloud, a steady-state conceptual model may describe a cumulus cloud quite well, but this does not hold for a single instance. Traditionally, a cloud life time is split into three phases: a) a young cloud with a strong vertical growth, b) a mature cloud, where the inflow of air from the sub-cloud thermal is assumed to be in balance with detrainment from the cloud into the environment, and c) a decaying cloud where the underlying thermal has died out and the cloud is slowly mixed away into the environment.

For as long as cumulus clouds have been studied, there have been studies into the difference between the stages of the lifecycle of clouds. For instance, Malkus (1952); Scorer and Ludlam (1953) gained a lot of qualitative insight by looking at sequences of photographs taken from cumulus congestus clouds. In these photographs, a pulsating (or bubbly) growth of the clouds is visible. These pulses are often thought to be important for cloud evolution, because each pulse increases humidity and cools the air, thus creating more favorable circumstances for subsequent pulses. This mechanism is thought to be important in the development of deeper convection (Khairoutdinov and Randall, 2002; Kuang and Bretherton, 2006). However, pulses are also often observed in a system of shallow cumulus clouds. Grinnell et al. (1996) and Blyth et al. (2005) for instance, followed a single, isolated cumulus near Hawaii throughout its lifecycle using radar; French et al. (1999) combined radar with simultaneous penetrations of clouds by multiple air planes. All these studies showed that cumulus clouds consist of one or a sequence of multiple pulses. With state-of-the-art 3D radar scanning radar techniques, field campaigns like Rain in Cumulus over the Ocean (RICO Rauber et al., 2007a) or even in longer time series as currently planned in the Atmospheric Radiation Measurement program (ARM), the life cycle can be studied in ever increasing detail.

Observational studies aside, large-eddy simulations (LES) serve as a convenient way to study the behavior of cumulus clouds because, in LES, in principle the 3 dimensional, time dependent fields of all variables are available. However, these complete data sets can easily cause a huge amount of data, which makes it difficult to retrieve any needle at all from the haystack.

Ideally, one would implement an automated criterion to isolate in time and space the clouds one wants to study. However, determination of such a criterion is not as straight-forward as it may seem. Not only does a representative cloud need to be somewhat isolated from the rest of the ensemble to remove unexpected cloud-cloud interaction from the statistics; but also the cloud needs to be large enough, active enough and possess a certain longevity while still being similar to the many smaller clouds in the ensemble. One way to remedy this problem is to follow a cloud through its life cycle by perturbing the sub-cloud layer (see, e.g., Bretherton and Smolarkiewicz, 1989; Grabowski and Clark, 1991, 1993a,b; Carpenter et al., 1998a; Blyth et al., 2005). This creates a cloud at a predictable space and time, but the artificially created sub-cloud thermal may cause anomalous inflow into the cloud. In the spirit of Malkus (1952), Scorer and Ludlam (1953) and also of French et al. (1999), Zhao and Austin (2005a,b, hereafter ZA05a and ZA05b) chose to hand-pick 6 clouds from their LES by watching an animation of the cloud field evolving in time. Thanks to their manual selection of clouds, ZA05a and ZA05b circumvented for a large part the necessity of setting a numerical criterion for an automated selection of representative clouds. Yet, the labour-intensive selection process of clouds makes it non-trivial to study more than a few clouds. Therefore, a statistically reliable representation of the cloud life cycle that yields quantitative results remains difficult to achieve.

This study aims to remedy this, and look at the lifecycle of cumulus clouds using

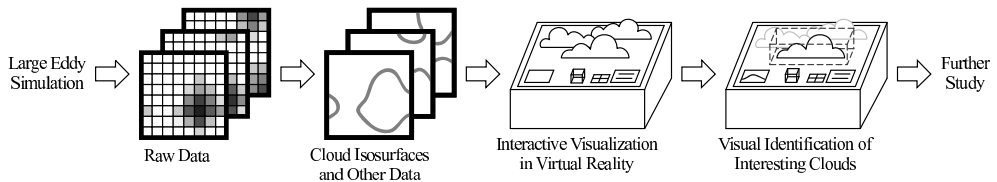


Figure 6.1: Overview of the workflow of post processing. From Griffith et al. (2005).

the statistical sampling over a large number of clouds. In this way, the differences between younger and older clouds, and especially the role of pulses in the evolution of clouds, is studied extensively.

As argued above, the main obstacle to overcome is devising a selection process that is sufficiently fast to select a large number of suitable clouds. Instead of aiming at building a highly intelligent automated cloud selection, we make use of the fact that the human eye is well capable of selecting clouds in space and time. In this study, we therefore use a Virtual Reality Environment (VE) to visualize the cloud field because such an environment is much better equipped than a 2D computer screen to visualize time dependent 3D fields, and, thus, it connects well with both the human perception as well as the physics of the clouds. The observer can, aided by the VE, swiftly select many clouds that fit the requirements. After this selection procedure, further post processing away from the VE can then result in a statistical approach to the life-cycle analysis of cumulus clouds.

The remainder of this study consists of the following parts. In section 6.2, the methodology used is described, including details of the LES, case descriptions, and the post processing procedure with the VE. In section 6.3, the life cycles of two individual clouds are treated, followed in section 6.4 by a discussion of the (thermo-) dynamical properties of a suitably averaged representation of the life cycle of the entire ensemble of selected clouds.

6.2 METHODOLOGY

The workflow of this study is illustrated in figure 6.1. First, cloud field datasets are created with large-eddy simulations, and then the cloud fields are visualized in the VE, where representative clouds are selected. After obtaining the location of these clouds, their properties are further studied outside of the VE.

6.2.1 Large-eddy simulations

A parallelized version of the Dutch Atmospheric LES (DALES) model, as described by Cuijpers and Duynkerke (1993), was used to run the simulations. With this model, we performed six simulations of the well-documented Barbados Oceanographic and Meteorological EXperiment (BOMEX, Siebesma et al., 2003), one simu-

lation of BOMEX without large scale forcings, and one simulation based on observations at the Southern Great Plains (SGP) site of the Atmospheric Radiation Measurement (ARM) program, following the intercomparison by Brown et al. (2002). The relevant details of the three cases are briefly summarized in this section.

Following Siebesma et al. (2003), the sensible and latent surface heat fluxes in the standard BOMEX case amount to 8 W m^{-2} and 150 W m^{-2} , respectively (resulting in a Bowen ratio of $r_B = 0.05$). Lifting condensation level is located around $z_{\text{LCL}} = 450 \text{ m}$ and the inversion layer lies between 1500 m and 2000 m . BOMEX shows a relatively large mean vertical shear, up to $1.8 \text{ m s}^{-1} \text{ km}^{-1}$.

Simulations were carried out on a domain of $6.4 \text{ km} \times 6.4 \text{ km} \times 3.2 \text{ km}$, with a resolution of $\Delta x = \Delta y = 25 \text{ m}$, $\Delta z = 20 \text{ m}$. For each of the 6 runs (statistically identical, but each with a different random perturbation of the initial field), 7 hours were simulated, of which the first 3 hours were discarded as spin-up. The complete 3D fields of the 3 components of the velocity u , v , and w , as well as liquid water potential temperature θ_l , the total water content q_t and liquid water content q_l were recorded to disk for every 6 s of simulation time in short (2 bytes) form. This resulted in a 1.7 TB sized data set, that contains a complete description of the flow.

To gain a better understanding of the clouds, several hypotheses will need to be tested on cases different from the standard BOMEX case. In this study, two additional experiments are done to meet this requirement. Firstly, BOMEX is performed without any large-scale forcings but with otherwise identical specifications. This means that, in comparison with the specifications of Siebesma et al. (2003): a) no Coriolis force is applied, b) the geostrophic wind is set to 0, and c) no large-scale subsidence, longwave radiative cooling or mean moisture tendency is present. Especially the removal of large-scale subsidence in this simulation results in a significant growth of the atmospheric boundary layer. This means that, unlike the standard BOMEX case, the simulation is not in quasi-steady-state anymore, which is reflected in the cloud base reaching 800 m and an inversion height of 2400 m during the simulation, although the inversion height remains well below domain height during the 7 h of simulation.

The characteristics of the ARM case include a diurnal cycle with the sensible and latent heat flux peaking at 140 W m^{-2} and 500 W m^{-2} , respectively. These surface fluxes are much stronger than for BOMEX, and also result in a much higher Bowen ratio ($r_B = 0.28$), as can be expected for a continental ABL. While the mean wind is comparable with BOMEX ($U \approx 10 \text{ m s}^{-1}$), less vertical shear is observed ($0.3 \text{ m s}^{-1} \text{ km}^{-1}$) in the bulk of the domain. Similar to Brown et al. (2002), the simulation is performed on a $6.4 \text{ km} \times 6.4 \text{ km} \times 4.4 \text{ km}$ domain with a resolution of $\Delta x = \Delta y = 25 \text{ m}$, $\Delta z = 20 \text{ m}$. The first 7 h are discarded, allowing the cloud layer to fully develop. Clouds are selected from the 8th to the 13th hour. Typical values for the cloud base height and inversion height are 1100 m and 2200 m , respectively. Again, all data is written to disk every 6 seconds.

6.2.2 The Virtual reality environment

The Virtual Reality Laboratory at Delft University of Technology is the result of a collaboration between the faculty of Computer Science and the faculty of Applied Sciences. One of the goals of this collaboration is to develop new data visualization techniques, which can be directly applied to data from research on physical processes, such as atmospheric phenomena. The virtual environment used in this paper is a product of this collaboration, and it was especially developed for visualizing cloud data (see Griffith et al., 2005).

The virtual environment runs on a Virtual Workbench system. Such a system supports the lab bench metaphor, where users look down on their data rather than being immersed in it. See figure 6.2.

Our workbench has a display area that is 179 x 110 cm in size and has a resolution of 1400 x 850 pixels. The system is driven by a dual Pentium 4 Xeon 3.6 GHz computer with 2 gigabytes of RAM. The data to be visualized is stored locally on a RAID, which has read speeds of up to 160 megabytes/second. Our software is based on OpenSceneGraph (www.openscenegraph.org), which is an open source scene graph library.

The stereo, or “3D”, effect of the virtual reality system is created by showing different, specially rendered images to the user’s left and right eyes. In our workbench, this is achieved with the help of two projectors, one for each eye, that are equipped with special filters. We use INFITEC filters (www.infitec.net), which alternatively filter out the left or the right half of the red, blue and green portions of the color spectrum. The projectors are housed inside the workbench and project, via a mirror, the separate images onto the back of the screen. The stereo effect is completed by having users wear special INFITEC goggles that have corresponding filters to block out the image for the other eye.

In our setup, users directly interact with the data by looking at it and with two input devices: a stylus (e.g. for pointing and selection) and a Plexiglass panel (e.g. for slicing through the data). The 3D position and orientation of these devices and the user’s head are tracked by a Polhemus Liberty electromagnetic tracker. Our software uses the Virtual Reality Peripheral Network (VRPN, Taylor et al., 2001) to interface with the tracker. Tracking the user’s head position allows us to render the virtual scene from his or her perspective, which then always gives the user a correct view of the scene and enhances the 3D effect.

6.2.3 Cloud selection in the virtual environment

To visualize the clouds, all gridpoints that are neighbors (taking the horizontal periodic boundary conditions into account) in 4D space-time are considered to be of the same cloud system and are labeled that way. In the VE, clouds are visualized by depicting the interface where q_l becomes larger than zero. Additional information on selected clouds, like the evolution of mass or liquid water content in time, is shown in 2D graphs beside the cloud field. Cloud systems that collide or split,

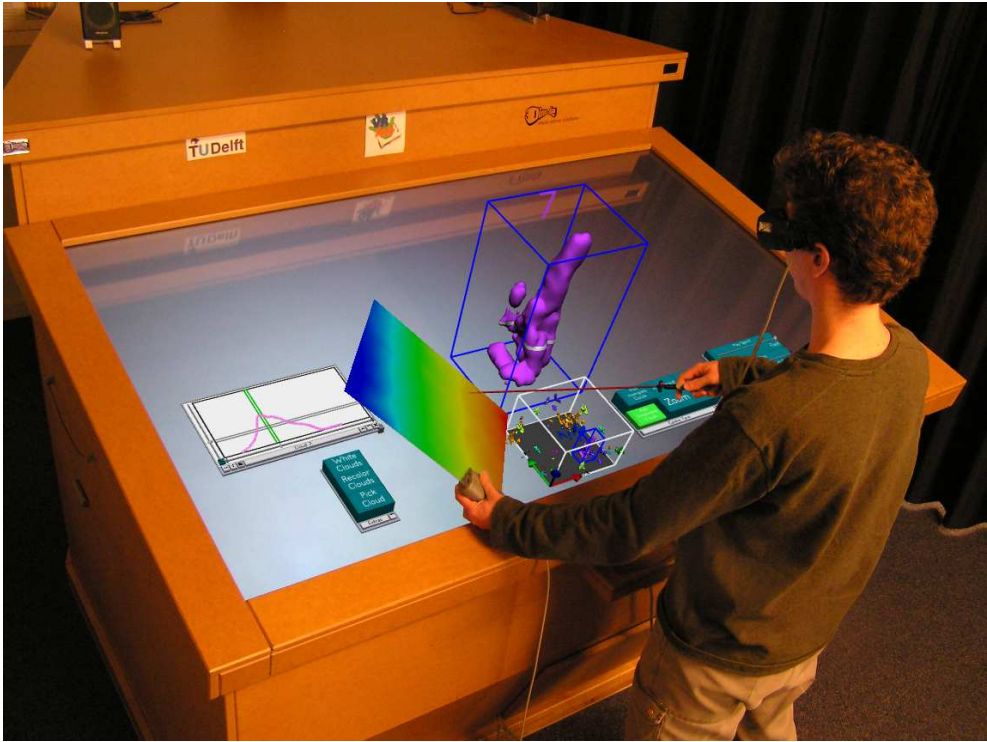


Figure 6.2: A user working on the virtual environment running on our Virtual Workbench. The user looks down on the data and can use the Plexiglass panel or the stylus to interact with the virtual environment. By wearing electromagnetically tracked, INFITEC goggles, the user is provided with a stereo view of the scene, which is rendered from the user's perspective. The cube containing the cloud field can be rotated, zoomed in upon and browsed through in time. By selecting individual clouds, more information becomes available (e.g., the volume as a function of time)

systems that already exist at the beginning or still exist at the end of the simulation can be automatically removed from the selection. Additional controls enable the observer to zoom in on a specific region of the cloud field, to rotate the field, or to browse back and forth in time.

Using the VE to browse through the data, active cumulus clouds are selected that, during the bulk of their lifetime, consist of a clear main body with possibly a few chunks broken off. This criterion works rather well during the visible inspection. If a group of clouds is labeled by the VE as one single cloud system, but the observer perceives them as separate clouds that collide at a certain time, the group can be easily dismissed. Like in most observational (airborne) campaigns, the focus

of cloud selection lies on active clouds with reasonable life spans. Although this criterion by definition removes many passive, small and short-lived clouds from the ensemble, the selected clouds aim to be representative of all the active clouds in the cloud field.

Using this method for all datasets, 35 clouds are selected from the regular BOMEX case simulations. From the BOMEX case without large scale forcings, 12 clouds are selected. From the ARM case, 32 clouds are selected. With this number of clouds in the ensemble, we have confidence that a reliable statistical approach is possible.

6.3 INSPECTION OF INDIVIDUAL CLOUDS

Before advancing towards a statistical approach, we start with a description of two clouds, referred to as cloud A and cloud B, that are exemplary for the entire BOMEX ensemble. To get a good feel for the lifecycle of these two clouds, we look at the evolution in time and height of various slab-averaged properties:

$$\bar{\phi}(z, t) = \frac{1}{A_c} \int_{A_c} \phi dx dy, \quad (6.1)$$

with A_c the area of the cloud as a function of height and time, and $\phi \in \{\rho\Delta z, w, \Delta q_t, q_l, \Delta\theta_l, \Delta\theta_v\}$. If $\phi = \rho\Delta z$, this can be seen as the mass of a slice of the cloud with height Δz , and density ρ . The other variables are the vertical velocity w , the total water excess with regard to the environmental average Δq_t , the liquid water content q_l , the liquid water potential temperature excess $\Delta\theta_l$, and the virtual potential temperature excess $\Delta\theta_v$. The time-height variations for these six variables are shown for cloud A and cloud B in figures 6.3 and 6.4, respectively. For all 12 figures, the presence of the pulses immediately strikes the eye. To assess the typical time between these pulses, we define the pulse interval time t_p as the average time between two maxima in cloud mass at 800 m. Averaged over all 35 clouds, t_p is equal to 408 s. This does not match with the convective timescale of the subcloud-layer convection:

$$t^* = \frac{z_{cb}}{\left(\frac{g}{\Theta_0} \overline{w'\theta'_v}\right)^{1/3}} \approx 720 \text{ s} \quad (6.2)$$

with $z_{cb} = 450$ m is taken as the depth of the subcloud layer, Θ_0 a reference temperature, g the gravitational acceleration and $\overline{w'\theta'_v} \approx 1.7 \times 10^{-2} \text{ Km s}^{-1}$ the buoyancy flux. This pulse timescale t_p is universal over all clouds in the ensemble; the difference between smaller, shortlived clouds and larger long-lived clouds lies mainly in the number of pulses. If we look at each pulse individually, the emergent view is reminiscent of the shedding thermal of Blyth (1993). From a nearly neutral cloud base, a short but strongly buoyant thermal head develops, dragging along the region below; this is expressed in the broader and less pronounced pulses in the average vertical velocity. Near the top of the pulse, the cloud becomes negatively

buoyant first, goes through a momentum overshoot after that, and shows a small period of cohesive downward motion during collapse.

Of all the panels in figures 6.3 and 6.4, pulsating growth is most pronounced in the mass of the cloud, meaning that a cloud during a strong pulse is simply wider. But a clear signal is also observed in the other panels of figures 6.3 and 6.4, although effects of height dependency sometimes dominate, especially for the liquid water potential temperature.

For all the clouds, the pulses are relatively narrow when looking at the liquid water content and at the total water content; the onset of the pulse in terms of those variables also slightly precedes the pulse in the cloud-mass graph. One recognizes clearly the onset of a pulse is triggered by an excess in moisture, an increase in buoyancy, followed by an increase in cloud mass and vertical velocity. The vertical velocity shows, due to the inertia of the pulse, slower adjustment to the pulse; during the decay of a pulse, especially, the vertical velocity remains high for a long time. At higher levels in the cloud, the buoyancy can be negative, but, due to inertia, the pulse continues to rise.

Usually, the first pulse is one of the strongest pulses that occur in the life of the cloud. However, contrary to ZA05b's findings, a general trend where every pulse is weaker than its predecessor is not observed. Large pulses sometimes split in separate branches at higher levels. The influence of a pulse on subsequent pulses is somewhat unclear here; on the one hand, a previous pulse tends to moisturize and cool the air and make it more favorable for future pulses. On the other hand, the strong downdrafts at the end of a pulse life time often prevent the subsequent pulse from fully developing.

Finally, it is interesting to note the presence of the convection inhibition (CIN) layer slightly above cloud base; buoyancy is close to zero, as is the liquid water content. Also, the total water content and the liquid water potential temperature are more or less constant in time; although trends on an even longer timescale are present in the size of the cloud, the pulse as observed at higher levels, has not yet developed. In the earliest lifestages of the cloud, the entire cloud is a forced cloud; similar to what happens in the transition from shallow cumulus to deep convection (Khairoutdinov and Randall, 2002; Kuang and Bretherton, 2006), these shallow cumuli themselves need to moisten their immediate environment before the CIN can be overcome.

If we neglect mixing between cloud and environment, vertical advection would be the only way properties could travel through the diagrams. In other words, the value of w should match with the slope of the isolines of the conserved variables in figures 6.3 - 6.6. This holds qualitatively for the updrafts, traveling from the lower-left corner to the upper-right corner, with a steeper slope (acceleration) as the pulse travels to higher levels. However, this does not hold at all during the decay of the pulse, where the vertical velocity goes to zero or becomes negative, but information still propagates upward. Only the downdrafts at the cloud top are able to propagate in the lower-right direction. Other downdrafts, located below a pulse, propagate upward, along with the pulse. This is a signature of a buoyancy

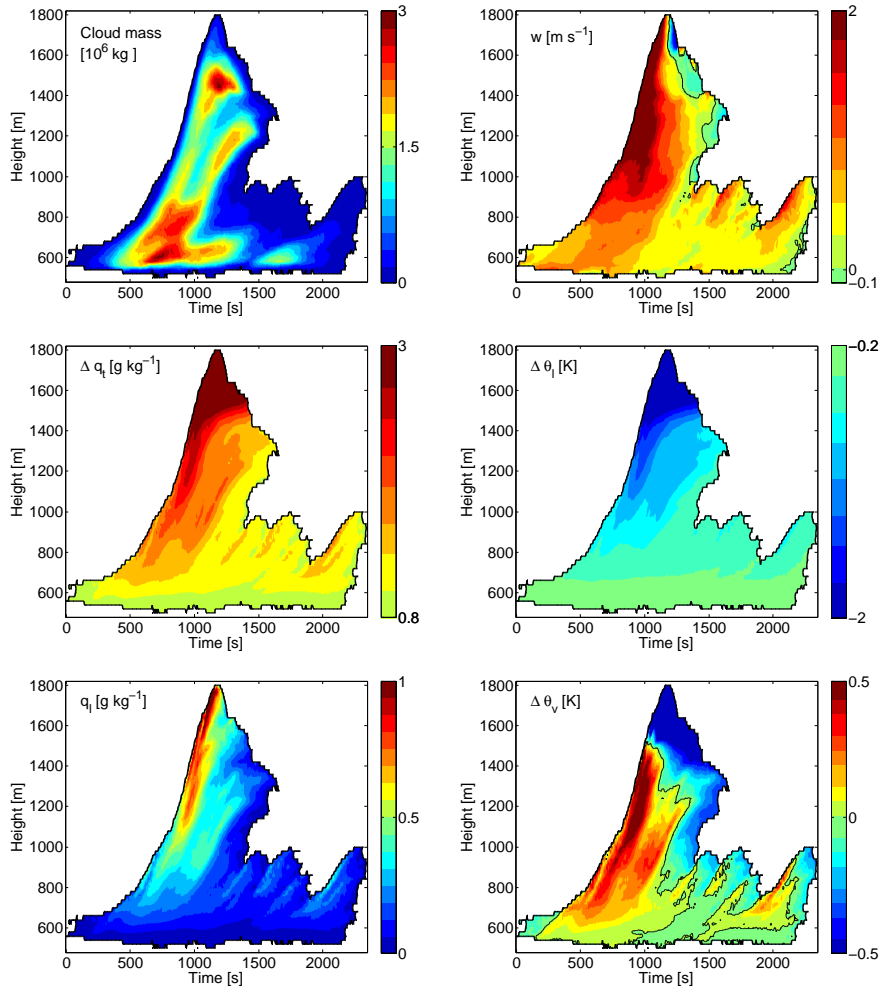


Figure 6.3: Height-time plots of the cloud-area averaged mean properties for cloud A. The thick line denotes the cloud top and cloud base; the thin contour line denotes the 0–isoline.

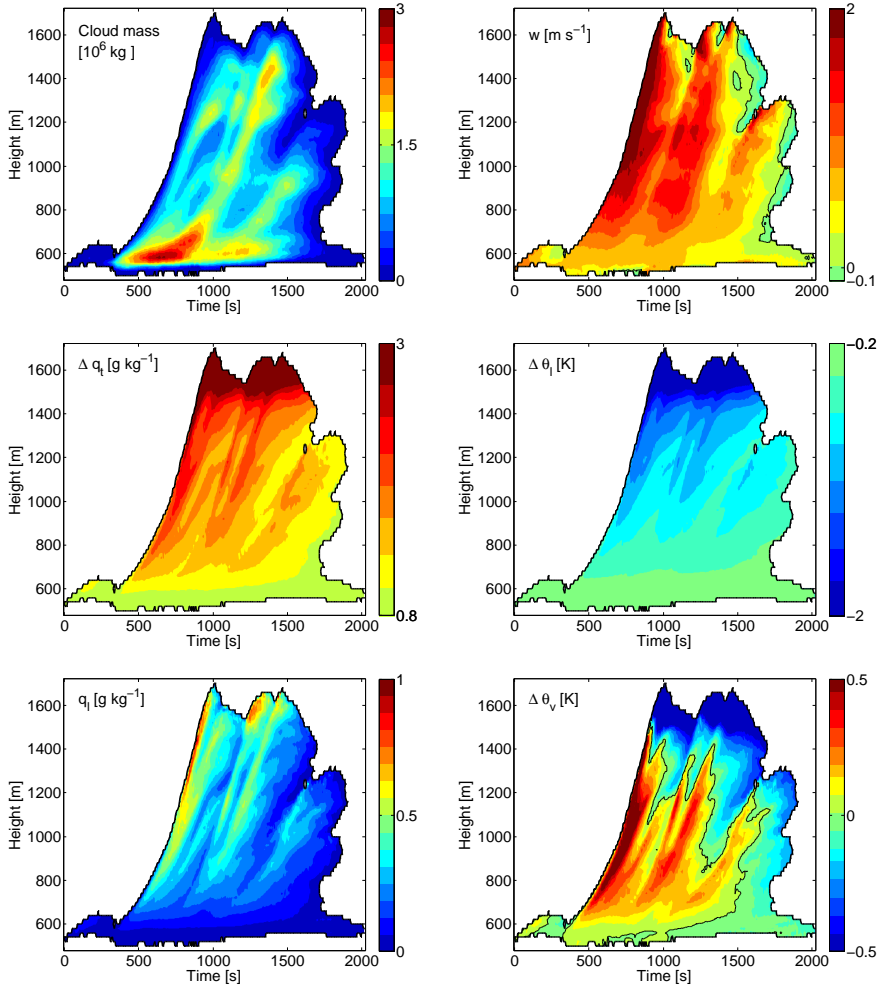


Figure 6.4: Height-time plots of the cloud-area averaged mean properties for cloud B. The thick line denotes the cloud top and cloud base; the thin contour line denotes the 0-isoline.

sorting mechanism; in the wake of a bubble, air that is less buoyant slows down and mixes away into the environment, and by leaving the cloud, the downdraft leaves the ensemble by definition.

To study the time dependent behavior of the cloud-environment interaction, the near-cloud region can be taken into account. This near-cloud region can be defined in several ways; ZA05a defined it by the concentration of a passive tracer that originated in the sub-cloud layer, and Couvreux and Rio (2008) showed that a threshold in q_t -excess also reveals much of the near-cloud region. Heus and Jonker (2008b); Jonker et al. (2008); Heus et al. (2008a,d) showed that a subsiding shell can be expected in an area of 200 m immediately around the cloud. However, hardly anything is known about the behavior of the shell in time. So, here we define the shell as all environmental air that resides within 200 m from the edge of the nearest cloud edge at that height, and we can define the shell-averaged properties of a cloud as:

$$\bar{\phi}^s(z, t) = \frac{1}{A_s} \int_{A_s} \phi dx dy, \quad (6.3)$$

with $A_s = A_s(z, t)$ the area of the shell. In figures 6.5 and 6.6, the mean excesses of liquid water potential temperature, total water content, and virtual potential temperature and the mean vertical velocity of the shell are presented for cloud A and cloud B.

The liquid water potential temperature and the total water content excesses are roughly anti-correlated. This results in a virtual potential temperature that follows the liquid water potential temperature in a subdued manner. For most of the time and most of the heights, the conserved variables θ_l and q_t mix linearly and display values between their in-cloud and slab-averaged environmental value. The virtual potential temperature and vertical velocity are negative, meaning that a subsiding shell is indeed present. However, patches of *positive* excess in the liquid water potential temperature (and negative excess in the total water content) are very pronounced. The only possible source of this air is from higher levels of the environment. Presumably, this is air dragged down by the shell that is induced at higher levels. Note, however, that the excesses are relatively small; an excess in liquid water potential temperature of 0.1 K, or a deficit in total water content of -0.1 g kg^{-1} , suggests that this air has been dragged down by about 20 m. This relatively small displacement can also be observed in the upward pointing isolines of the vertical velocity, even for regions with negative velocity in the shell. Clearly, the velocity in the shell is a slave to the cloud system and does not propagate very far on its own.

Due to the many mixing effects interacting in the physics of the shell, the signature of the pulses is not as pronounced in the shell as within the cloud, despite the fact that the shell dynamics are a slave to the cloud dynamics. Some signature of the pulse can be observed in the vertical velocity, where strong environmental downdrafts directly correlate with strong pulsating growth. The onset of the first pulse, the ascending cloud top (ACT), travels through an undisturbed environment.

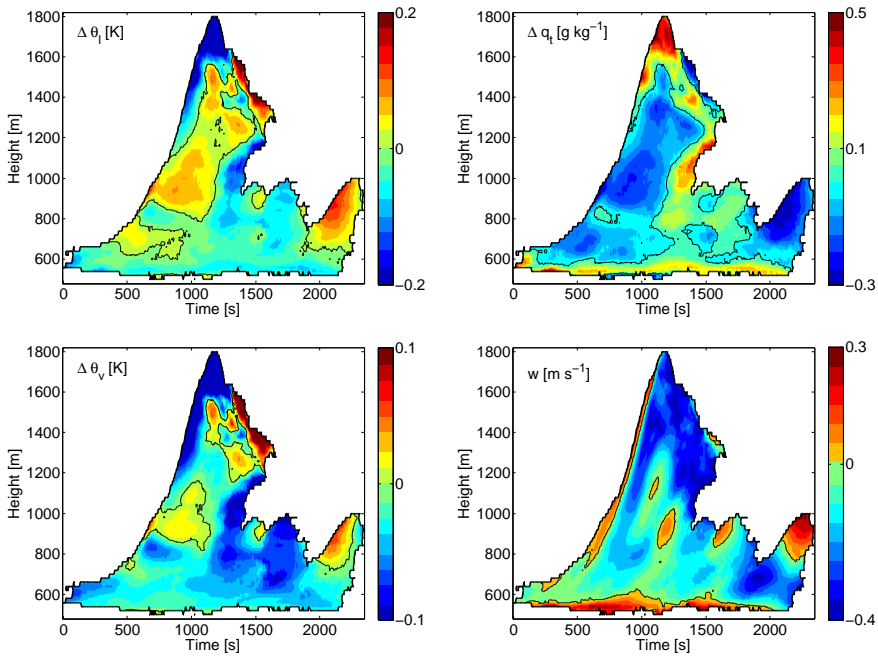


Figure 6.5: Height-time plots averaged over the environment within 200 m of cloud A. The thick line denotes the cloud top and cloud base; the thin contour line denotes the 0-isoline.

This results, for a short while, in environmental air being dragged upward before the effect of mixing results in downward motion in the shell. During the decay phase of the pulse, subsidence in the shell decreases, up to the point where environmental velocities can even become positive. This can be explained as follows. As discussed by Heus and Jonker (2008b), the vertical velocity in the shell consists of a balance between environmental air being dragged upward by the momentum of the cloud, and detrained cloudy air moving downwards due to buoyancy reversal. Firstly, during the decay phase of the pulse, the in-cloud air is greatly diluted. If such air detrains from the cloud, only a little buoyancy reversal occurs. Secondly, the decay of the pulse triggers a period of highly negative horizontal divergence, resulting in more entrainment and less detrainment. Both mechanisms combined result in an increased vertical velocity.

Although the pulses are still clearly visible in the vertical velocity diagrams of figures 6.3 and 6.4, hardly any of its signal can be found in the thermodynamic quantities. Where conservation of momentum tends to spread the region of negative vertical velocity, the region of negative buoyancy is much smaller; the buoyancy minimum should lie at or very near to the cloud edge. This means that, for the ther-

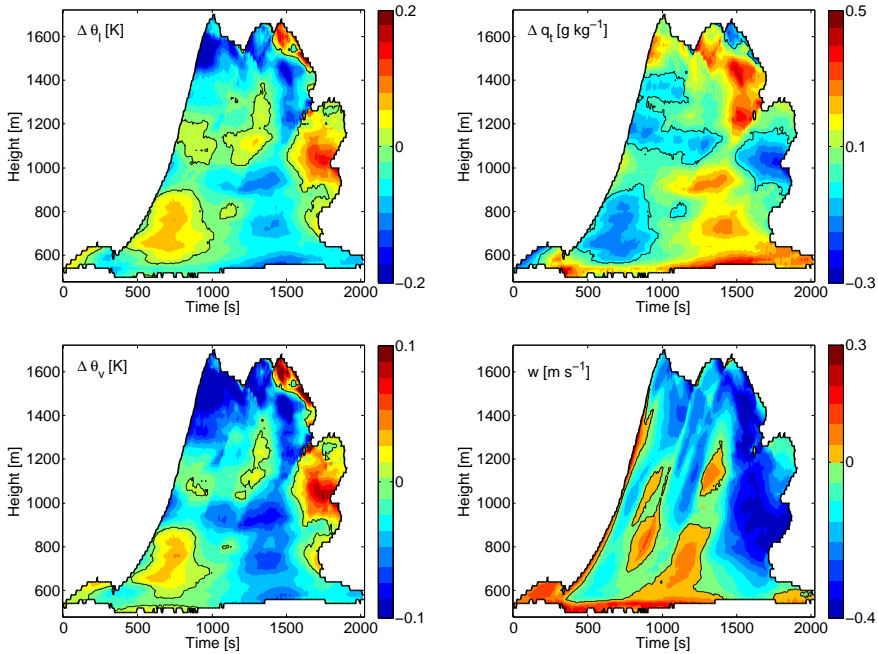


Figure 6.6: Height-time plots averaged over the environment within 200 m of cloud B. The thick line denotes the cloud top and cloud base; the thin contour line denotes the 0-isoline.

modynamic variables, a large part of the 200 m wide shell consists of environmental air that is only very indirectly part of the cloud system and cannot react fast enough to accommodate for changes in the cloud properties along the life cycle of a pulse.

The total mass flux through the cloud and the shell combined is equal to

$$\begin{aligned}
 M_c(z, t) + M_s(z, t) &= \int_{A_c} \rho w(x, y, z, t) dA \\
 &+ \int_{A_s} \rho w(x, y, z, t) dA,
 \end{aligned} \tag{6.4}$$

with ρ the density of the air and with A_c and A_s the area of the cloud and the shell, respectively. They are shown for the two clouds in figure 6.7.

In general, these results are very similar to the ones reported by ZA05a, with a positive mass flux during the first stages of the cloud lifetime and a negative mass flux afterwards. However, while ZA05a argued that the regime change from positive to negative mass flux propagates downward in time for large clouds and upward in time for smaller clouds, neither can be concluded from our results. Instead, the phase change from an upward transport in the cloud system to a downward

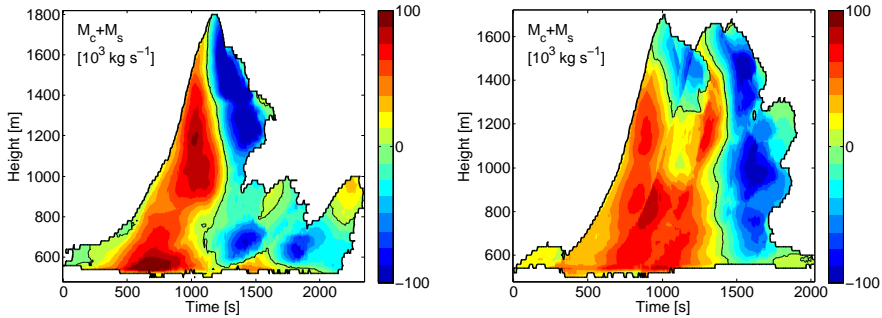


Figure 6.7: The massflux integrated over the cloud and the shell for both clouds.

transport goes on a very short time scale, that is, within 200 s over the entire 1000 m high cloud. This means that, regardless of the exact cause of this phase change, information about the change travels through the cloud with a speed of 5 m s^{-1} , much higher than the maximum velocity observed in the cloud at any time or height.

6.4 STATISTICAL REPRESENTATION

As was shown in section 6.3, many processes, especially inside the cloud, are more governed by the life cycle of the pulses rather than by the life cycle of the entire cloud. In a sense, a cloud can be seen as a sequence of one or more pulses, and the life time is defined by the number of pulses a cloud consists of. In figure 6.8, a composite cloud has been built by scaling all selected clouds with their individual life time t_c . This way, a natural emphasis lies on the beginning and the end of the cloud life cycle, because these are automatically synchronized by this procedure. The decline in cloud mass, and the negative buoyancy, especially, at the end of the cloud life cycle are clearly visible. However, because the mature phase of the cloud is not so well synchronized, much of the pulse-like structure is averaged out. Thus, an important element of the cloud life cycle is ignored.

Therefore, if we want to do a life-cycle analysis, it stands to reason to do a life-cycle analysis over the pulse instead of over the entire cloud. To perform such an analysis, an averaging procedure as schematically drawn in figure 6.9. Each of the 35 clouds is divided up in pulses with a duration of $t_p = 408 \text{ s}$, counting from the moment the ascending cloud top passes through observation level. Quantities are conditionally sampled with their time and height in the pulse. An average pulse is composited from this sampling, with the pulse onset defined as the average pass-through time of the ACT. This procedure means that the onset of the first pulse is by definition synchronized for all clouds. However, because each cloud consists on average of 4 pulses, much of the signal after sampling is governed by the subsequent pulses, and not by the ACT itself.

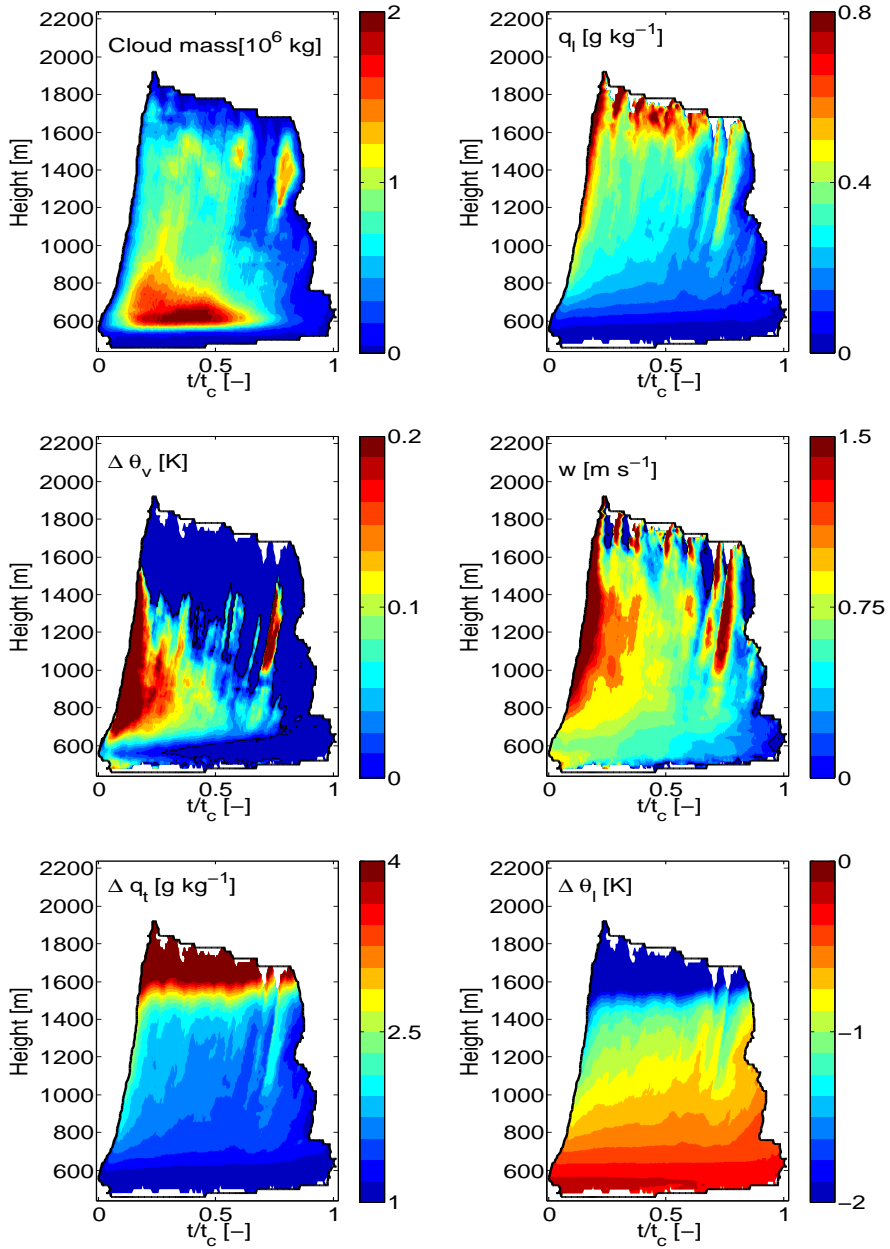


Figure 6.8: Thermodynamical properties averaged over the life time of clouds instead of the pulses.

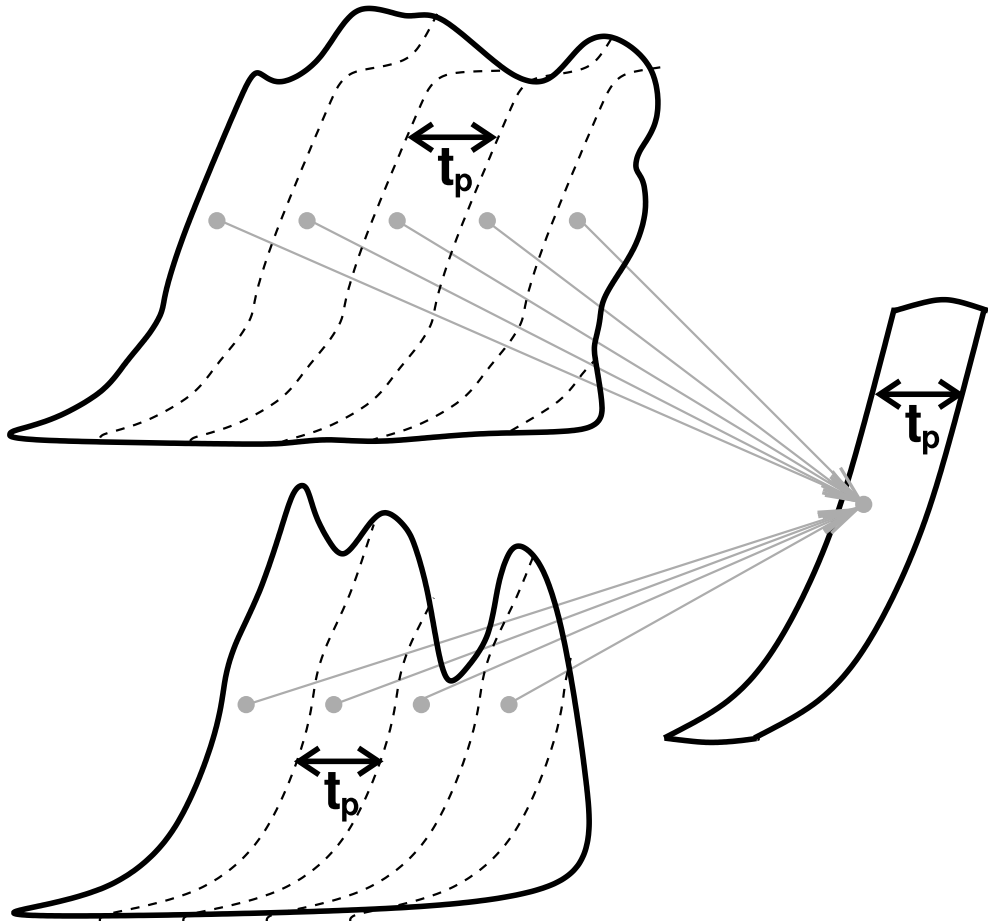


Figure 6.9: A schematical overview of the averaging procedure over all pulses. All clouds are divided in pulses with a duration of $t_p = 408$ s, and quantities are conditionally sampled with their time and height in the pulse.

In figure 6.10, the thermodynamic properties of the composite pulse are presented. We expect, for levels where the pulsating growth is important for the behavior of the cloud, to see a clear evolution in time, i.e. vertical contour lines. For the cloud mass, liquid water content and (consequently) buoyancy, especially, this signal is very clear throughout the entire pulse. For higher levels, the periodic behavior also becomes pronounced in the vertical velocity. Clearly, the fluctuations are initiated by an increase in buoyancy, which is followed at higher altitudes (above 1000 m) by increased advection that can push the air well into the inversion region, despite its negative buoyancy.

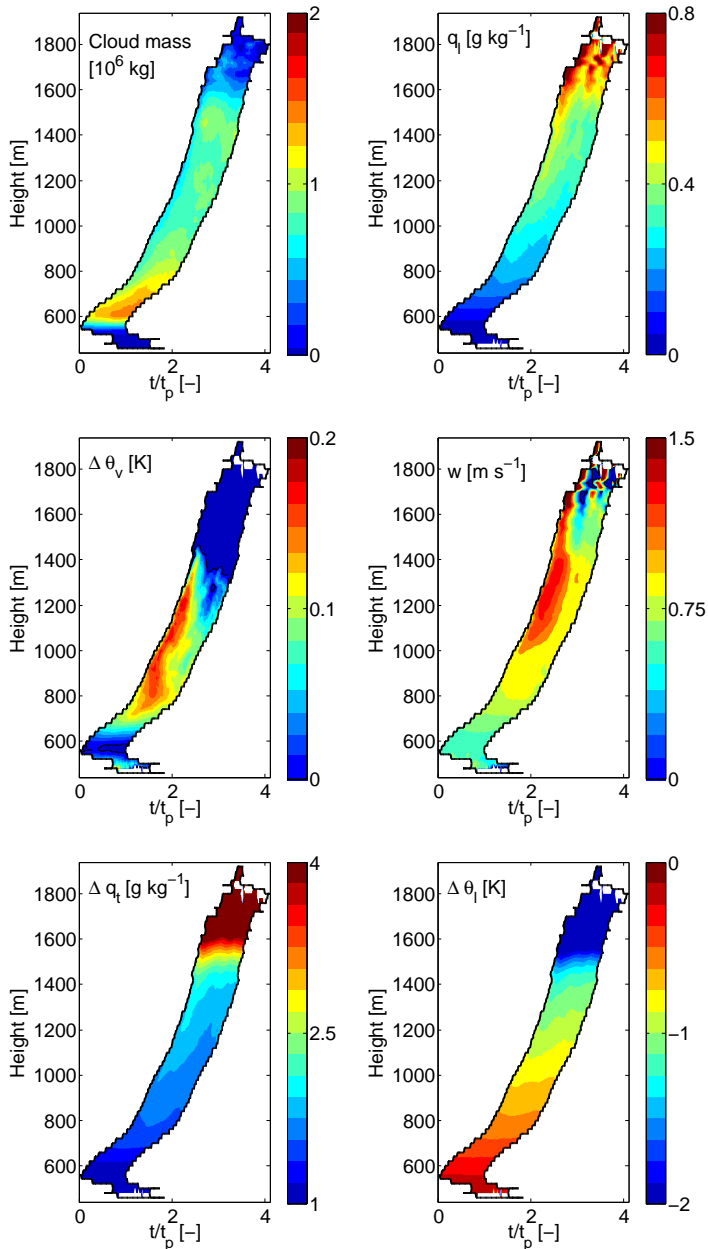


Figure 6.10: Thermodynamical properties of the pulse within the cloud.

However, effects of stratification hide the appearance of the pulse in the signal of θ_l and q_t , and, also for θ_v in the inversion layer. Therefore, it is interesting to look at the normalized deviations from the cloud averaged values:

$$\phi''(z, t) = \phi(z, t) - \langle \phi \rangle(z), \quad (6.5)$$

with $\phi = \{w, q_l, q_t, \theta_v, \theta_l\}$ and $\langle \phi \rangle$ is the slab-averaged value, conditioned over all selected clouds. By definition, this graph will always display a zero-crossing at some point in time, so it is important to look at the size and coherency of the fluctuations. This is done in figure 6.11. In terms of liquid water content or buoyancy, the pulse flows coherently into the inversion layer. After reaching cloud top, the pulse breaks up in an oscillating motion. This should probably be interpreted as chunks of cloud that, during their dissipation phase, go through a couple under- and overshoots.

The fluctuations of the conserved quantities at 1000 m, q_t'' and θ_l'' , are in the order of 0.2 g kg^{-1} and 0.1 K , respectively. This is roughly equal to 10% of the mean in-cloud excess of these quantities. Despite these relatively small fluctuations, the effect on the buoyancy is relatively large, on the order of 40% of the mean excess. This is due to the fact that all the fluctuations in q_t'' are one-to-one mirrored in the liquid water content q_l'' , which in turn has a strong impact on the buoyancy.

6.4.1 Possible mechanisms behind pulsating growth

So far, we have seen that pulsating growth is important in the life-cycle of cumulus clouds, but it is yet unclear what the driving mechanism is behind these pulses. Three possible mechanisms are:

1. The cloud layer is decoupled from the sub-cloud layer, and the clouds drift from thermal to thermal. Such a process can be disregarded as unlikely, because a decoupling should result in a discontinuity in the mean horizontal velocity, which is not the case.
2. The sub-cloud thermal itself consists of separate pulses, for instance due to strong mean shear.
3. The pulse is part of the cloud dynamics.

To investigate the possibility of the pulsating sub-cloud thermal, it is instructive to look at two other cases of shallow cumulus besides standard BOMEX: a modified BOMEX case, without any large scale forcings, and the ARM case. Although the ARM case shows a mean wind of 10 m s^{-1} , this mean wind is constant in the bulk of the sub-cloud layer, so no mean shear is observed there. In figure 6.12, the buoyancy of a typical cloud from both cases is shown; both clouds clearly show pulsating growth and on a timescale comparable with $t_p = 412 \text{ s}$ as observed in standard BOMEX. What is more, the (relatively big) CIN layer is clearly visible in the ARM case as a layer without any oscillations visible in time; this was already

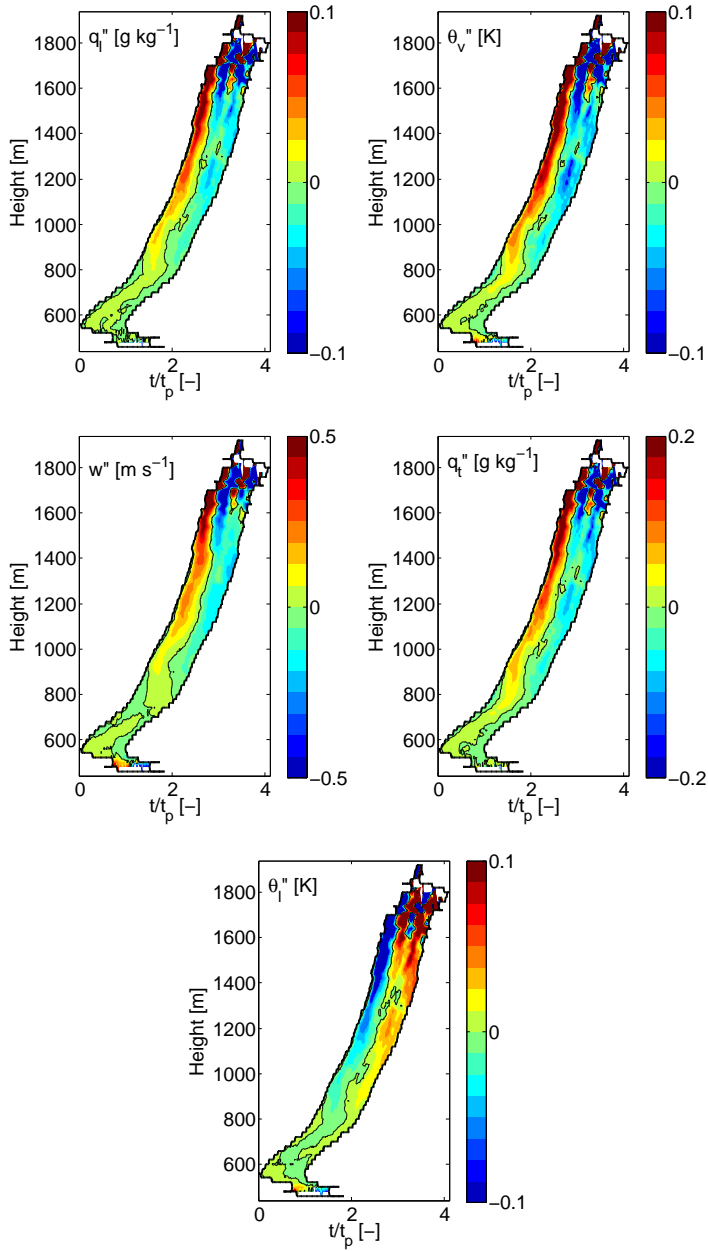


Figure 6.11: Fluctuations of thermodynamical properties of the pulse within the cloud.

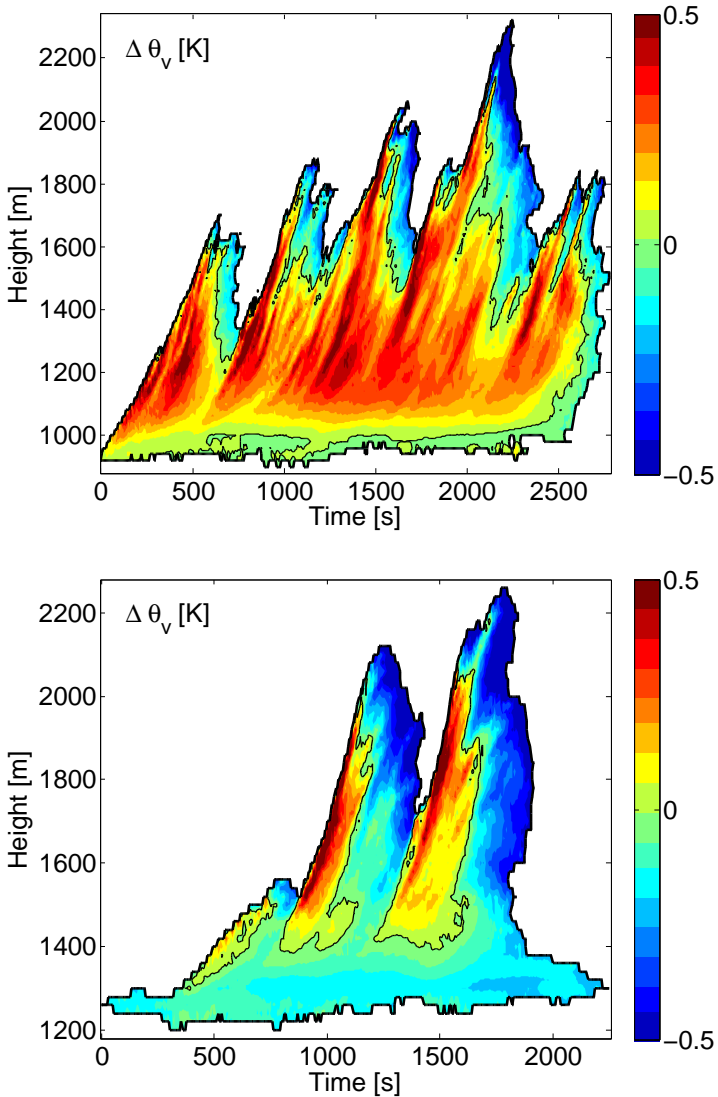


Figure 6.12: The mean virtual potential temperature of two clouds, one (top) from BOMEX without large scale forcings and one (bottom) from ARM.

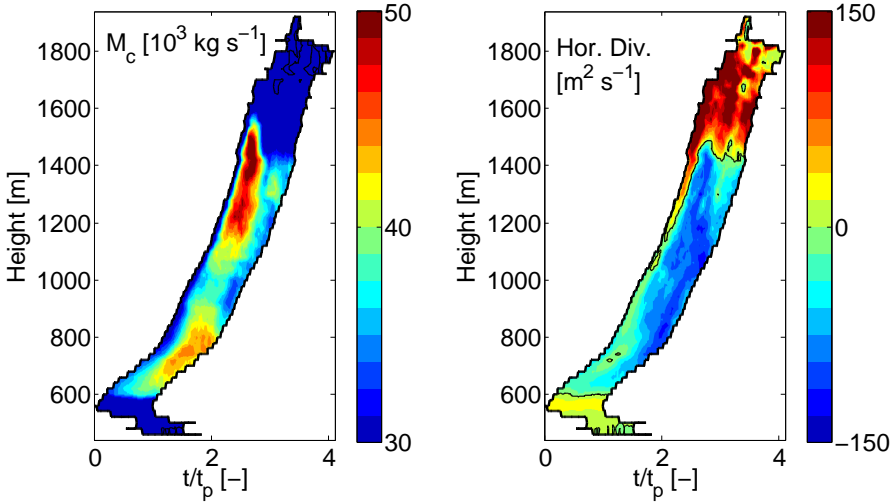


Figure 6.13: Mass flux and horizontal divergence in the pulse.

visible in standard BOMEX, although the CIN layer is much weaker in that case, and the effect is consequently less pronounced. Apparently, the CIN layer serves as a buffer between the sub-cloud thermal and the convective cloud; fluctuations in the inflow of air into the CIN layer (if any) are buffered by it and can thus not be the cause of the pulsating growth of the rest of the cloud.

Therefore, the third possible mechanism, that pulsating growth is a feature of the cloud’s own dynamics is the most likely candidate remaining. In figure 6.13, the in-cloud massflux M_c and the horizontal divergence D

$$D = \int_{A_c} -\frac{\partial w}{\partial z} dA, \tag{6.6}$$

are plotted. Focussing on the region below 1000 m, we see that the maximum in $\Delta\theta_v$ in figure 6.11 precedes the maximum mass flux, which in its turn is followed by the divergence, that has a minimum (i.e., maximum convergence) near the end of the pulse, similar to the mechanism described by Hunt et al. (2003). The cloud is first fueled with buoyant air from the subcloud layer. The buoyancy creates a large mass flux. This pulse accelerates, induces lateral inflow, becomes detached from its source of supply and fades again. An important (maybe dominating) part in this mechanism could be caused by the fact that the vertical acceleration results in convergence of dry, warm air from the environment in the wake of the pulse, effectively recreating the convection inhibition.

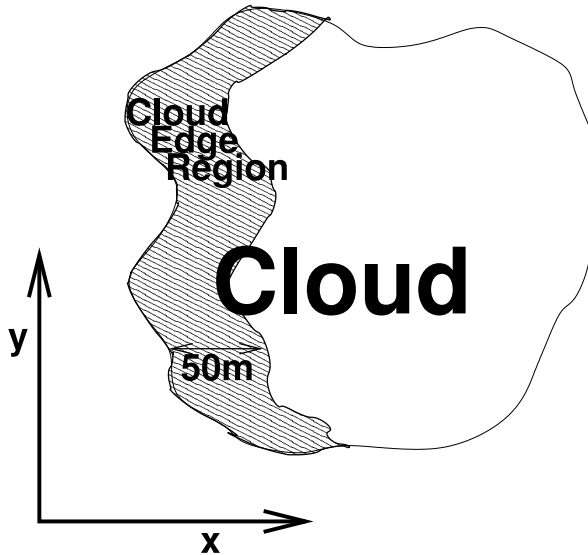


Figure 6.14: The cloud edge region as discussed in the text to calculate the edge-liquid water path \tilde{q}_e . The cloud is observed in the x -direction, and the liquid water content q_l is integrated over the first 50 m from the cloud interface to obtain \tilde{q}_e .

6.5 HOW SHARP ARE THE EDGES?

In observations the life stage of a cloud is often judged from the sharpness of the edges. To express this ‘sharpness’ in terms of a quantity available in LES, we associate the sharpness with the horizontally integrated amount of liquid water at the edges of a cloud \tilde{q}_e . As is schematically shown in figure 6.14, the edge region is taken for every horizontal slab of the cloud as the region within 50 m from the cloud interface in the x -direction. The idea is that an increased amount of liquid water near the edge of the cloud leads to lower transmissivity, up to the point where the transmissivity approaches zero and the edge is perceived as ‘sharp’.

In the evolution in time and height of \tilde{q}_e in figure 6.15 for the two clouds A and B that were discussed in section 6.3, several features are visible. As the saturation mixing ratio q_s decreases with height, the edge-liquid water path increases trivially. During the early life stages of the cloud, \tilde{q}_e is high and the edges are sharp as expected, especially near the ascending cloud top where values of \tilde{q}_e are the highest. However, during the remainder of the cloud life time, \tilde{q}_e does not decrease monotonously, but displays a strong periodic component. This can be associated with pulse-like behavior, meaning that low values of \tilde{q}_e are not so much associated with the decaying stage of the entire cloud, but rather with the decaying stage of a pulse.

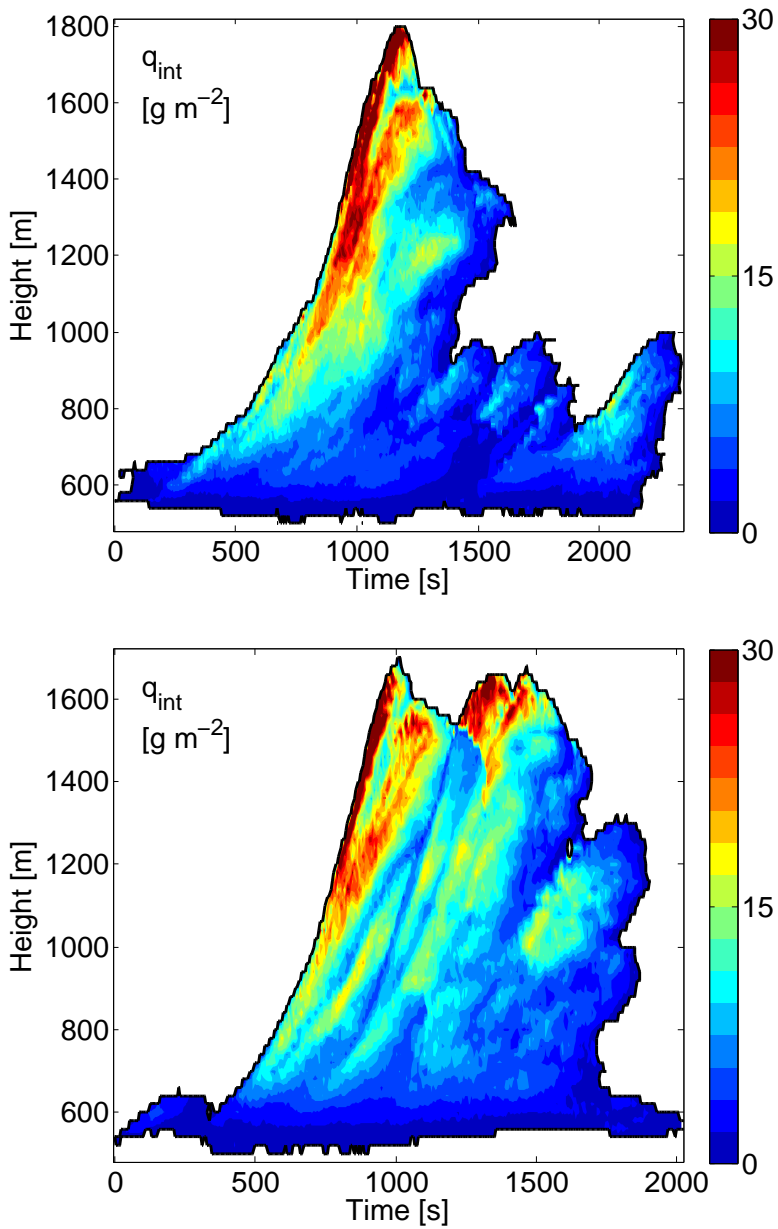


Figure 6.15: Edge-integrated liquid water content q_{int} as a function of height and time for cloud A and cloud B. The thick contour line indicates cloud top and cloud base.

6.6 CONCLUSIONS

In this study, we have made an attempt to do a life-cycle analysis of cumulus clouds in a statistically reliable way. The use of the VE has facilitated the selection process in such a way, that a sufficient number of clouds could be selected – to the best knowledge of the authors, for the first time. Of course, using human perception to make a selection of clouds generated by numerical simulations could initiate a bias towards the clouds that are perceived as favorable by the observer. But, because conditional averages of the mean thermodynamic variables over the entire cloud field yields results similar to the values found in the averages over the selected clouds, the selection process is reliable and, given the outcome, rather effective.

The oscillating nature of cumulus clouds is shown to be a key factor in the understanding of the life cycle of clouds. For many purposes, a cloud can best be seen as a sequence of pulses, which is in agreement with the findings by Malkus (1952); French et al. (1999); Zhao and Austin (2005a,b).

The pulses are observed in several cases, and are independent from large-scale lateral forcings on the sub-cloud layer. This means that the pulses originate from the cloud layer and, in combination with the earlier reports of the pulse, pulsating growth is clearly a generic feature of the dynamics of cumulus clouds.

In the course of this study, the convective inhibition (CIN) has proven to be a small yet clearly visible layer in the cumulus cloud, and it is hypothesized that the CIN plays a crucial role in the life cycle of cumuli. First of all, the CIN functions as a barrier during the initial stage that has to be overcome by a steady supply of buoyancy from the sub-cloud thermal. During this stage, the cloud complies with the classical image of a forced cloud. The first pulse can only shoot through the cloud layer after the local CIN is sufficiently moistened and cooled. Later on in the life cycle of the cloud, the CIN serves as a buffer layer that releases its supply of buoyancy into the cloud with a more or less steady rate.

Above the CIN, the pulses are driven by a system where buoyancy induces acceleration, horizontal convergence, and detachment of the pulse from its source (see figure 6.16). This is similar to the model proposed by Hunt et al. (2003) for the formation of thermals and/or plumes in the dry convective boundary layer. The fundamental difference between the dry and the cloudy convective boundary layer is that, for clouds, the instability can be much stronger due to hostile environment of the cloud and due to the latent heat release of condensation. In terms of momentum budget, this would be a time dependent balance between buoyancy and vertical advection.

One feature of the cloud system (that is, the cloud and its immediate surrounds) cannot be captured by the pulse-like model of the cloud: at some point during the life cycle of the cloud system, the total mass flux of the system switches from net upward to net downward. At that moment, the mass flux within the cloud remains positive but is dominated by the downward mass flux in the shell. Interestingly enough, this change of sign seems to occur within a short time over the entire height of the cloud, suggesting that information about the regime change has traveled

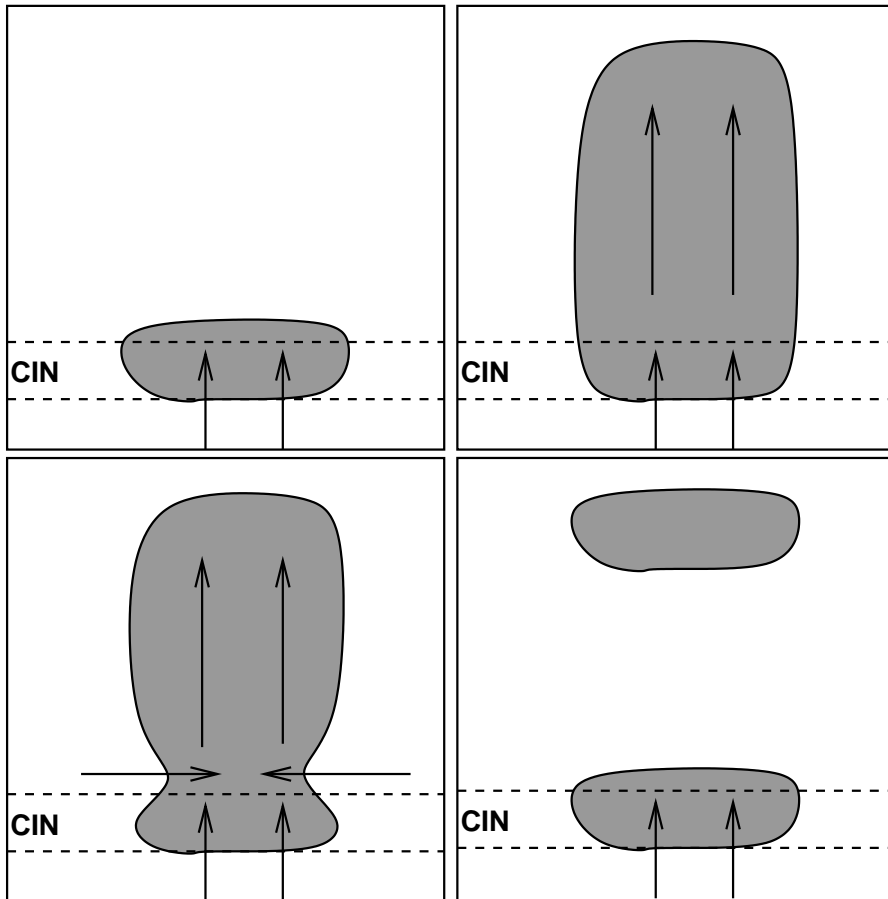


Figure 6.16: Conceptual picture of the pulse. A steady supply of buoyant air enters the cloud through the CIN, the air accelerates, generates horizontal convergence and inflow of environmental air, which causes detachment of the pulse from its source and finally, the pulse decays.

through the cloud with a speed higher than the maximum velocity observed within the cloud.

CHAPTER 7: CONCLUDING REMARKS

In this thesis, the interaction between shallow cumulus clouds and their environment has been explored, and fluctuations of these interactions in space and time. Detailed findings are thoroughly discussed in the concluding sections of chapters 3 to 6, but the overall picture that emerges from these studies is as follows.

I've looked at clouds from both sides now,
From up and down, and still somehow
It's cloud illusions I recall,
I really don't know clouds at all.

JONI MITCHELL

7.1 OVERVIEW

A schematic view on the cloud (see figure 7.1) It was shown in chapter 3 that the subsiding shell is consistently present at all heights around shallow cumulus clouds, and that the shell is driven by lateral mixing and evaporative cooling. The mass flux through this shell is such that it compensates a large part of the in-cloud upward mass flux (see chapter 4, Jonker et al. (2008)). However, the shell should not be interpreted as a clean elevator transporting the former in-cloud air all the way down back to the sub-cloud layer. It should be stressed that coherent penetrative downdrafts, extending over substantial heights, are extremely rare, although some were found, both inside the cloud or alongside the cloud. In general, air descends no more than 200 m within the shell, while further mixing with environmental air. Thus, the compensating mass flux in the shell consists of air that left the cloud just above the level of observation, or air that originates from the environment just above the level of observation. Interestingly enough, the most effective mechanism to transport a parcel of environmental air downward is to get the parcel close to an active cloud.

In chapter 5 it was shown that clouds have a tendency to predominantly entrain air from the sides, and not so much from the top, although Paluch diagrams suggest different sources of entrained air, even more than can be explained by the buoyancy sorting argument of Taylor and Baker (1991). In terms of transport of environmental air by the cloud, it was shown that the environmental air entrained into the cloud, on average ends up a few hundred meters higher than where it originated from. Part of this gain in height is undone by the evaporative cooling when such a parcel leaves the cloud again.

On average, air in the far environment remains nearly motionless. As shown in chapters 4 and 5, this does not mean, however, that the instantaneous vertical velocity is zero. Air usually leaves the cloud in an over- or undershoot, and this excites a buoyancy wave in the environment. Such waves can be quite coherent, have a sizeable amplitude, but do not contribute to dispersion or to balancing the in-cloud mass flux.

The time dependency of the cloud's motion (see chapter 6) shows that for a correct description of the cloud, it is best to describe the cloud as a sequence of bubbles or pulses. Each pulse is fed by the sub-cloud thermal, that is stabilized by the convective inhibition. The buoyancy surplus in each pulse results in an acceleration, detachment from the cloud base and massive entrainment from the sides. After this, the formation of a new pulse can begin. This procedure repeats itself at a time scale that is distinct from the convective time scale of the sub-cloud layer, and will continue as long as the sub-cloud thermal feeds the convective inhibition.

Comparison between LES and observations The fine-grained comparison between simulations and observations of in-cloud dynamics as presented in chapter 3 and chapter 4 gives much confidence in the validity of LES for future research on detailed cloud physics. Specifically, LES is capable of calculating the mean velocity profiles in and around the cloud at a high level of accuracy. However, as can be seen in the comparison of the variances in section 3.3, and in the overall conclusions from chapter 4, the fluctuations are generally underpredicted by LES. It is assumed that this underprediction is due to the finite grid of LES. These unresolved subfilter-scale fluctuations do not show up in a probability density function of w obtained from LES, but are accounted for by observations.

As long as such limitations of both are firmly kept in mind in studies however, especially the combination of the physical reality of observations and the completeness of LES has proven to be very powerful.

Use of the virtual reality environment One of the main objectives of this joint research project of the faculties of applied physics and of computer sciences was to investigate the use of a virtual reality environment in this kind of research, beyond the scope of making fancy graphics for presentation purposes.

Although the Virtual reality Environment only had a place in chapter 6 of this thesis, it should be stressed that it was a prominent one; the selection of such a number of clouds would not have been possible without the way the VE visualizes 3D, time-dependent data. The VE implementation of the Lagrangian particles dispersion model (Dussel, 2007) has already proven its use in, for instance, the dispersion studies by Remco Verzijlbergh and in direct numerical simulations of cloud droplets (Woittiez et al., 2008).

While the VE can play a pivotal role in investigating 3D, time-dependent data, the aims of VE-use should be chosen with care. By definition, research always hovers on the edge of the unknown, generating questions that demand for ad-hoc

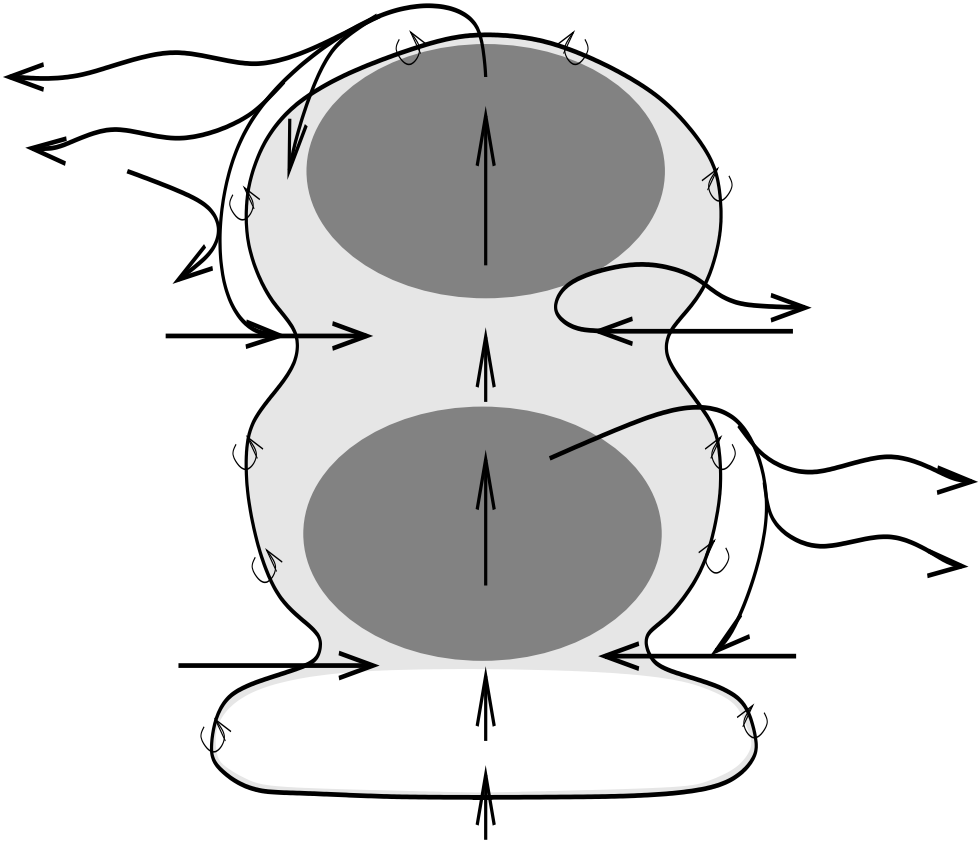


Figure 7.1: Conceptual picture of the motion of air in and around the cloud.

development of methodology; users can hardly expect the development of the VE to keep up with this. Likewise, while it may be tempting to extract quantitative results from the VE, it will always be hard to predict what qualitative results will be desired in future results. Focus on generating reliable qualitative visualization of multi-variable datasets may better play the strengths of the VE. Although the role of the VE might be less clear to pinpoint in the final, qualitative, result of a research project, its role can easily be a pivotal one.

7.2 OUTLOOK

Like nearly every research project, more questions have been raised than have been answered. Some of them seem to yearn for an immediate answer; a few of those research paths are listed below.

Improved modeling of the cloud, shell and environment The conceptual model as presented in section 3.6 is limited in the sense that it assumes a steady-state cloud and disregards any dependency of height. In the Bachelor's thesis of Sanders (2007), time and height variations have been accounted for, but other work still remains to be done. For instance, lateral mixing is currently modeled as a function of the size of the shell, while ideally, this size of the shell should be an outcome of the model rather than an input parameter. Also, since the pulsating growth as discussed in chapter 6 is also rooted in a balance between buoyancy and lateral mixing between the three layers, the analytical model can be expected to show such oscillating behavior as well.

The influence of the shell on entrainment For a reliable parameterization of the cloud including the subsiding shell, the role of the shell on entrainment has to be further explored. It remains unclear so far if and in what sense the subsidence of detrained air has an influence on the air that is to be entrained into the cloud. Events of entrainment and detrainment could be separated in space (see also section 3.5.3) and in time (see chapter 6); therefore, the location of entrained air is not altered too much by the shell (see section 5.5). However, for the composition of the air mixed into the cloud, the shell might be more relevant, as it acts as a buffer layer between cloud and environment. This means that only pre-conditioned air is mixed into the cloud, which has consequences for the homogeneity of the cloud droplet mixing, and through that on the droplet size distribution (Gerber et al., 2008), and also for the mass flux parameterization of the cumulus cloud. In a mass flux parameterization, the lapse rate of conserved variables inside the cloud is given by:

$$\frac{\partial \phi_c}{\partial z} = -\varepsilon_c (\phi_c - \phi_e) \quad (7.1)$$

where ϕ is one of the conserved variables θ_l or q_t , and ε the entrainment rate as a function of height. The c subscript denotes cloud values, and the e subscript denotes environmental values. The incorporation of the shell would result in an additional equation:

$$\begin{aligned} \frac{\partial \phi_c}{\partial z} &= -\varepsilon_c (\phi_c - \phi_s) \\ \frac{\partial \phi_s}{\partial z} &= -\varepsilon_s (\phi_s - \phi_e) + \delta_c (\phi_c - \phi_s) \end{aligned} \quad (7.2)$$

with the s subscript denoting the shell; see also figure 7.2. However, whether or not the subsiding shell really plays such a buffering role, whether this role is also relevant in a description of an entire cloud field as a single bulk cloud, and whether it is necessary to incorporate it for a better description of cumulus clouds in large scale modeling, has yet to be determined.

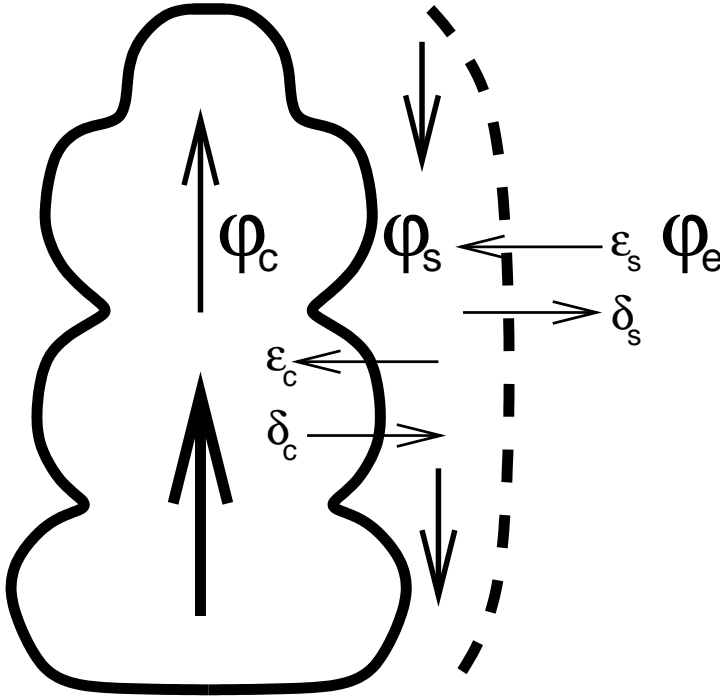


Figure 7.2: A modified mass flux scheme where the shell acts as a buffer between cloud and environment.

Explain the mechanism behind the Paluch diagrams While Taylor and Baker (1991) showed a very plausible explanation for the discrepancy between the real source level of entrained air and the source level as inferred from Paluch diagrams, chapter 5 showed that their buoyancy sorting regions are not able of fully explaining the shape of the Paluch diagrams. Given the monumental status of the Paluch (1979) paper, this paradox deserves resolution, even if only for historical reasons.

Ongoing development of DALES As to the code development beyond the current version DALES₃, there are always many options for code improvement, for making it faster, more accurate or broaden its scope, although such improvements are not necessarily new, ground-braking science in itself.

First thing to do is to make sure DALES could run on many-core supercomputers. This will be necessary because of the general trend in supercomputing to add more cores to a computer instead of improving the speed of the cores, and because of the general trend in the atmospheric sciences to resolve more (expensive) physics such as advanced microphysics schemes. More fundamentally, the atmosphere is a 4D problem which is currently resolved with a 1D parallelization. If we require at

least 4 grid cells per process (which in general provides an optimal balance between minimal wall clock time and minimal computational cost), a 512-cubed simulation can now be performed on upto 128 processes. Additional parallelization in the z direction allows for 16,384 processes, which should be enough for the upcoming generation of supercomputers. After that, more parallelization can be achieved in the x direction (which could give problems in the Poisson solver, since this is the only homogeneous unparallelized direction left). An entirely different approach is to parallelize the equations that have to be solved. This could be done by parallelizing the computations of the various terms of the resolved equations like advection, diffusion, and so on, although it would be difficult in achieving similar run time for each process. Alternatively, variable space could be parallelized, with a different process assigned to each of the prognostic variables (like u_i , θ_l and q_t). This could yield between 6 and hundreds of processes (in the case of simulations with detailed microphysics). However, such approaches would require recoding of large parts of DALES.

Currently, the only microphysics scheme implemented in DALES is a two-moment bulk-scheme. In the light of the fundamental tool that large-eddy simulations aim to be in the atmospheric sciences, it stands to reason to implement a bin microphysics scheme in DALES. While van Zanten et al. (2008) shows that the spread in results is just as big for the various models using bin microphysics, it should be noted that this may very well be the spread between different models, not necessarily between various microphysical implementations. Thus, reliable testing of such work can only be done within the framework of a single LES model. If nothing else, bin microphysics is necessary for comparison between observed and computed droplet spectra and for testing of hypotheses on the homogeneity of mixing processes.

To move beyond the realm of shallow cumulus clouds toward the (transition to) deep convection, the current Boussinesq approach needs to be abandoned in favor of an anelastic approximation of the Navier-Stokes equations, and incorporate the ice phase in the thermodynamical routines of DALES.

REFERENCES

- ACKERMAN, A., M. C. v. ZANTEN, B. STEVENS, V. SAVIC-JOVICIC, C. S. BRETHERTON, A. CHLOND, J.-C. GOLAZ, H. JIANG, ET AL., 2008: Large-eddy simulations of a drizzling, stratocumulus-topped marine boundary layer. *Mon. Wea. Rev.*, submitted.
- ARAKAWA, A. AND W. H. SCHUBERT, 1974: Interaction of a cumulus cloud ensemble with the large-scale environment, Part I. *J. Atmos. Sci.*, **31**, pp. 674–701, doi:10.1175/1520-0469(1974)031<0674:IOACCE>2.0.CO;2.
- ASAI, T. AND A. KASAHARA, 1967: A theoretical study of compensating downward motions associated with cumulus clouds. *J. Atmos. Sci.*, **24** (5), pp. 487–496, doi:10.1175/1520-0469(1967)024<0487:ATSOTC>2.0.CO;2.
- AUGSTEIN, E., H. RIEHL, F. OSTAPOFF, AND V. WAGNER, 1973: Mass and energy transport in an undisturbed Atlantic trade-wind boundary layer. *Mon. Wea. Rev.*, **101**, pp. 90–98, doi:10.1175/1520-0493(1973)101<0101:MAETIA>2.3.CO;2.
- AUSTIN, P. H., M. B. BAKER, A. M. BLYTH, AND J. B. JENSEN, 1985: Small-scale variability in warm continental cumulus clouds. *J. Atmos. Sci.*, **42** (11), pp. 1123–1138, doi:10.1175/1520-0469(1985)042<1123:SSVIWC>2.0.CO;2.
- BETTS, A. K., 1975: Non-precipitating cumulus convection and its parameterization. *Quart. J. Roy. Meteor. Soc.*, **99**, pp. 178–196, doi:10.1002/qj.49709941915.
- BETTS, A. K., 1982: Saturation point analysis of moist convective overturning. *J. Atmos. Sci.*, **39** (7), pp. 1484–1505, doi:10.1175/1520-0469(1982)039<1484:SPAOMC>2.0.CO;2.
- BJERKNES, J., 1938: Saturation-adiabatic ascent of air through dry-adiabatically descending environment. *Quart. J. Roy. Meteor. Soc.*, **64**, pp. 325–330.
- BLYTH, A. M., 1993: Entrainment in cumulus clouds. *J. Appl. Meteor.*, **32**, pp. 626–641, doi:10.1175/1520-0450(1993)032<0626:EICC>2.0.CO;2.
- BLYTH, A. M., W. A. COOPER, AND J. B. JENSEN, 1988: A study of the source of entrained air in Montana cumuli. *J. Atmos. Sci.*, **45** (24), pp. 3944–3964, doi:10.1175/1520-0469(1988)045<3944:ASOTSO>2.0.CO;2.
- BLYTH, A. M., S. G. LASHER-TRAPP, AND W. A. COOPER, 2005: A study of thermals in cumulus clouds. *Quart. J. Roy. Meteor. Soc.*, **131** (607), pp. 1171–1190, doi:10.1256/qj.03.180.
- BONY, S., R. COLMAN, V. M. KATTSOV, R. P. ALLAN, C. S. BRETHERTON, J.-L. DUFRESNE, A. HALL, S. HALLEGATTE, ET AL., 2006: How Well Do We Understand and Evaluate Climate Change Feedback Processes? *J. Climate*, **19**, pp. 3445–3482, doi:10.1175/JCLI3819.1.

- BRETHERTON, C. S., J. R. McCAA, AND H. GRENIER, 2004: A new parameterization for shallow cumulus convection and its application to marine subtropical cloud-topped boundary layers. Part I: Description and 1D results. *Mon. Wea. Rev.*, **132** (4), pp. 864–882, doi:10.1175/1520-0493(2004)132<0864:ANPFSC>2.0.CO;2.
- BRETHERTON, C. S. AND P. K. SMOLARKIEWICZ, 1989: Gravity waves, compensating subsidence and detrainment around cumulus clouds. *J. Atmos. Sci.*, **46** (6), pp. 740–759, doi:10.1175/1520-0469(1989)046<0740:GWCSAD>2.0.CO;2.
- BROWN, A. R., R. T. CEDERWALL, A. CHLOND, P. G. DUYNKERKE, J. C. GOLAZ, M. KHAIROUTDINOV, D. C. LEWELLEN, A. P. LOCK, ET AL., 2002: Large-eddy simulation of the diurnal cycle of shallow cumulus convection over land. *Quart. J. Roy. Meteor. Soc.*, **128** (582), pp. 1075–1093, doi:10.1256/003590002320373210.
- CARPENTER, R. L., K. K. DROEGEMEIER, AND A. M. BLYTH, 1998a: Entrainment and detrainment in numerically simulated cumulus congestus clouds. Part I: General results. *J. Atmos. Sci.*, **55** (23), pp. 3417–3432, doi:10.1175/1520-0469(1998)055<3417:EADINS>2.0.CO;2.
- CARPENTER, R. L., K. K. DROEGEMEIER, AND A. M. BLYTH, 1998b: Entrainment and detrainment in numerically simulated cumulus congestus clouds. Part III: Parcel analysis. *J. Atmos. Sci.*, **55** (23), pp. 3440–3455, doi:10.1175/1520-0469(1998)055<3440:EADINS>2.0.CO;2.
- CHLOND, A. AND A. WOLKAU, 2000: Large-eddy simulation of a nocturnal stratocumulus-topped marine atmospheric boundary layer: An uncertainty analysis. *Bound.-Layer Meteor.*, **95** (1), pp. 31–55.
- COUVREUX, F. AND C. RIO, 2008: A conditional sampling of boundary layer plumes for validation of mass flux parameterizations. The 18th Symposium on Boundary-Layers and Turbulence.
- CUIJPERS, J. W. M., 1990: Subgrid parameterization in a large-eddy simulation model. Ninth Symp. on Turbulence and Diffusion, pp. 176–179, Amer.Meteor.Soc., Roskilde, Denmark.
- CUIJPERS, J. W. M., 1994: Large-eddy simulation of cumulus convection. Ph.D. thesis, Delft University of Technology, ISBN:90-9006737-X.
- CUIJPERS, J. W. M. AND P. G. DUYNKERKE, 1993: Impact of skewness and nonlocal effects on scalar and buoyancy fluxes in convective boundary layers. *J. Atmos. Sci.*, **55**, pp. 151–162, doi:10.1175/1520-0469(1998)055<0151:IOSANE>2.0.CO;2.
- DAMIANI, R., G. VALI, AND S. HAIMOV, 2006: The structure of thermals in cumulus from airborne dual-Doppler radar observations. *J. Atmos. Sci.*, **63** (5), pp. 1432–1450, doi:10.1175/JAS3701.1.

- DEARDORFF, J. W., 1972: Theoretical expression for the counter-gradient vertical heat flux. *J. Geophys. Res.*, **77**, pp. 5900–5904, doi:10.1029/JC077i030p05900.
- DEARDORFF, J. W., 1973: Three-dimensional numerical modeling of the planetary boundary layer. D. A. Haugen, (ed.) Workshop on Meteorology, pp. 271–311, American Meteorological Society.
- DEARDORFF, J. W., 1980: Stratocumulus-capped mixed layers derived from a three dimensional model. *Bound.-Layer Meteor.*, **18**, pp. 495–527, doi:10.1007/BF00119502.
- VAN DIJK, G., 2007: The implementation of a Lagrangian particle dispersion model in large eddy simulations of the atmospheric boundary layer. Master's thesis, Delft University of Technology.
- DOSIO, A., 2005: Turbulent dispersion in the Atmospheric Convective Boundary Layer. Ph.D. thesis, Wageningen Universiteit, ISBN:90-8504-171-6.
- DOSIO, A., J. VILÀ-GUERAU DE ARELLANO, A. A. M. HOLTSLAG, AND P. J. H. BUILTJES, 2005: Relating Eulerian and Lagrangian statistics for the turbulent dispersion in the atmospheric convective boundary layer. *J. Atmos. Sci.*, **62** (4), pp. 1175–1191, doi:10.1175/JAS3393.1.
- DUFRESNE, J.-L. AND S. BONY, 2008: An assessment of the primary sources of spread of global warming estimates from coupled atmosphere-ocean models. *J. Climate*, doi:10.1175/2008JCLI2239.1, in press.
- DUSSEL, D., 2007: Interactive GPU-based Particle Tracing for Cumulus Cloud Research. Master's thesis, Delft University of Technology.
- EMANUEL, K. A., 1994: Atmospheric Convection. Oxford University Press, New York.
- FRENCH, J. R., G. VALI, AND R. D. KELLY, 1999: Evolution of small cumulus clouds in Florida: observations of pulsating growth. *Atmos. Res.*, **52**, pp. 143–165, doi:10.1016/S0169-8095(99)00024-1.
- GARRATT, J. R., 1992: The atmospheric boundary layer. Cambridge university press, ISBN:978-0-521-46745-2.
- GERBER, H., G. FRICK, J. B. JENSEN, AND J. G. HUDSON, 2008: Entrainment, mixing, and microphysics in trade-wind cumulus, submitted.
- GRABOWSKI, W. W. AND T. L. CLARK, 1991: Cloudenvironment interface instability: Rising thermal calculations in two spatial dimensions. *J. Atmos. Sci.*, **48** (4), pp. 527–546, doi:10.1175/1520-0469(1991)048<0527:CIIRTC>2.0.CO;2.

- GRABOWSKI, W. W. AND T. L. CLARK, 1993a: Cloud-environment interface instability: part ii: Extension to three spatial dimensions. *J. Atmos. Sci.*, **50** (4), pp. 555–573, doi:10.1175/1520-0469(1993)050<0555:CEIPI>2.0.CO;2.
- GRABOWSKI, W. W. AND T. L. CLARK, 1993b: Cloud-environment interface instability. part III: Direct influence of environmental shear. *J. Atmos. Sci.*, **50** (23), pp. 3821–3828, doi:10.1175/1520-0469(1993)050<3821:CEIPI>2.0.CO;2.
- GRIFFITH, E. J., F. H. POST, M. KOUTEK, T. HEUS, AND H. J. J. JONKER, 2005: Feature tracking in VR for cumulus cloud life-cycle studies. E. Kjemns and R. Blach, (eds.) *Virtual Environments 2005*, pp. 121–128.
- GRINNELL, S. A., C. S. BRETHERTON, D. E. STEVENS, AND A. M. FRASER, 1996: Vertical mass flux calculations in Hawaiian trade cumulus clouds from dual-Doppler radar. *J. Atmos. Sci.*, **53** (13), pp. 1870–1886, doi:10.1175/1520-0469(1996)053<1870:VMFCIH>2.0.CO;2.
- HEUS, T., 2008: On the edge of a cloud. Lecture at CNRM, MétéoFrance, Toulouse, France.
- HEUS, T., G. VAN DIJK, H. J. J. JONKER, AND H. E. A. VAN DEN AKKER, 2008a: Mixing in shallow cumulus clouds studied by Lagrangian particle tracking. *J. Atmos. Sci.*, **65** (8), pp. 2581–2597, doi:10.1175/2008JAS2572.1.
- HEUS, T. AND H. J. J. JONKER, 2006: Why do descending shells around cumulus clouds exist? The 17th Symposium on Boundary-Layers and Turbulence.
- HEUS, T. AND H. J. J. JONKER, 2008a: The day after tomorrow – Could this happen to us? Lecture at the Openbare Scholengemeenschap Lek en Linge, Culemborg, The Netherlands.
- HEUS, T. AND H. J. J. JONKER, 2008b: Subsiding shells around shallow cumulus clouds. *J. Atmos. Sci.*, **65** (3), pp. 1003–1018, doi:10.1175/2007JAS2322.1.
- HEUS, T., H. J. J. JONKER, H. E. A. VAN DEN AKKER, E. J. GRIFFITH, M. KOUTEK, AND F. H. POST, 2008b: A statistical approach to the life-cycle analysis of cumulus clouds selected in a Virtual Reality Environment. *J. Geophys. Res.*, submitted.
- HEUS, T., H. J. J. JONKER, H. E. A. VAN DEN AKKER, E. J. GRIFFITH, M. KOUTEK, AND F. H. POST, 2008c: A statistical approach to the life-cycle analysis of cumulus clouds selected in a Virtual Reality Environment. The 18th conference on Boundary-Layers and Turbulence.
- HEUS, T., H. J. J. JONKER, E. J. GRIFFITH, AND F. H. POST, 2006: Lifecycle analysis of cumulus clouds using a 3d virtual reality environment. The 17th conference on Boundary-Layers and Turbulence.

- HEUS, T., C. F. J. POLS, H. J. J. JONKER, H. E. A. VAN DEN AKKER, AND D. H. LENSCHOW, 2008d: Observational validation of the compensating mass ux through the shell around cumulus clouds. *Quart. J. Roy. Meteor. Soc.*, doi:10.1256/qj.08.66, accepted pending minor revisions.
- HEUS, T., C. F. J. POLS, H. J. J. JONKER, H. E. A. V. D. AKKER, AND D. H. LENSCHOW, 2008e: Observational validation of the compensating mass ux through the shell around cumulus clouds. The 18th conference on Boundary-Layers and Turbulence.
- HEUS, T. ET AL., 2008f: An overview of Dutch Atmospheric LES, in preparation.
- HEYMSFIELD, A. J., P. N. JOHNSON, AND J. E. DYE, 1978: Observations of moist adiabatic ascent in northeast Colorado cumulus congestus clouds. *J. Atmos. Sci.*, **35** (9), pp. 1689–1703, doi:10.1175/1520-0469(1978)035<1689:OOMAAI>2.0.CO;2.
- HOLLAND, J. Z. AND E. M. RASMUSSEN, 1973: Measurement of atmospheric mass, energy and momentum budgets over a 500-kilometer square of tropical ocean. *Mon. Wea. Rev.*, **101**, pp. 44–55, doi:10.1175/1520-0493(1973)101<0044:MOTAME>2.3.CO;2.
- HUNSDORFER, W., B. KOREN, M. VANLOON, AND J. G. VERWER, 1995: A positive finite-difference advection scheme. *J. Comput. Phys.*, **117** (1), pp. 35–46, doi:10.1006/jcph.1995.1042.
- HUNT, J. C. R., A. J. VRIELING, F. T. M. NIEUWSTADT, AND H. J. S. FERNANDO, 2003: The influence of the thermal diffusivity of the lower boundary on eddy motion in convection. *J. Fluid Mech.*, **31**, pp. 183–205, doi:10.1017/S0022112003005482.
- IPCC, 2007: Climate change 2007 - The physical science basis: Working group I contribution to the fourth assessment report of the IPCC (climate change 2007). Cambridge University Press.
- JENSEN, J. B., P. H. AUSTIN, M. B. BAKER, AND A. M. BLYTH, 1985: Turbulent mixing, spectral evolution and dynamics in a warm cumulus cloud. *J. Atmos. Sci.*, **42** (2), pp. 173–192, doi:10.1175/1520-0469(1985)042<0173:TMSEAD>2.0.CO;2.
- JONAS, P. R., 1990: Observations of cumulus cloud entrainment. *Atmos. Res.*, **25**, pp. 105–127, doi:10.1016/0169-8095(90)90008-Z.
- JONKER, H., T. HEUS, E. HAGEN, AND H. VAN DOP, 2004: Laboratory experiments of entrainment in dry convective boundary layers. The 16th Symposium on Boundary-Layers and Turbulence.
- JONKER, H., R. VERZIJLBERGH, T. HEUS, AND A. SIEBESMA, 2006: The influence of the sub-cloud moisture field on cloud size distributions and the consequences for entrainment. The 17th Symposium on Boundary-Layers and Turbulence.

- JONKER, H. J. J., T. HEUS, AND P. P. SULLIVAN, 2008: A refined view of vertical transport by cumulus convection. *Geophys. Res. Lett.*, **35**, p. L07810, doi:10.1029/2007GL032606.
- KAIN, J. S. AND J. FRITSCH, 1993: Convective parameterization for mesoscale models. The Kain-Fritsch scheme. *Meteor. Monogr.*, **24**, pp. 165–170.
- KHAIROUTDINOV, M. F. AND D. A. RANDALL, 2002: Similarity of deep continental cumulus convection as revealed by a three-dimensional cloud-resolving model. *J. Atmos. Sci.*, **59** (17), pp. 2550–2566, doi:10.1175/1520-0469(2002)059<2550:SODCCC>2.0.CO;2.
- KNIGHT, C. A. AND L. J. MILLER, 1998: Early radar echoes from small, warm cumulus: Bragg and hydrometeor scattering. *J. Atmos. Sci.*, **55** (18), pp. 2974–2992, doi:10.1175/1520-0469(1998)055<2974:EREFWS>2.0.CO;2.
- KUANG, Z. AND C. S. BRETHERTON, 2006: A mass-flux scheme view of a high-resolution simulation of a transition from shallow to deep cumulus convection. *J. Atmos. Sci.*, **63**, pp. 1895–1909, doi:10.1175/JAS3723.1.
- LAIRD, N. F., 2005: Humidity halos surrounding small cumulus clouds in a tropical environment. *J. Atmos. Sci.*, **62** (9), pp. 3420–3425, doi:10.1175/JAS3538.1.
- LAMONTAGNE, R. G. AND J. W. TELFORD, 1983: Cloud top mixing in small cumuli. *J. Atmos. Sci.*, **40** (9), pp. 2148–2156, doi:10.1175/1520-0469(1983)040<2148:CTMISC>2.0.CO;2.
- LENSCHOW, D. H., M. ZHOU, X. ZENG, L. CHEN, AND X. XU, 2000: Measurements of fine-scale structure at the top of marine stratocumulus. *Bound.-Layer Meteor.*, **97** (97), pp. 331–357, doi:10.1023/A:1002780019748.
- LILLY, D. K., 1967: The representation of small-scale turbulence in numerical simulation experiments. H. Goldstine, (ed.) Proc. IBM Scientific Computing symp. on Environmental Sciences, pp. 195–210.
- LIN, C. C. AND A. ARAKAWA, 1997: The macroscopic entrainment processes of simulated cumulus ensemble .2. Testing the entraining-plume model. *J. Atmos. Sci.*, **54** (8), pp. 1044–1053, doi:10.1175/1520-0469(1997)054<1044:TMEPOS>2.0.CO;2.
- LU, M. L., J. WANG, A. FREEDMAN, H. H. JONSSON, R. C. FLAGAN, R. A. McCLATCHEY, AND J. H. SEINFELD, 2003: Analysis of humidity halos around trade wind cumulus clouds. *J. Atmos. Sci.*, **60** (8), pp. 1041–1059, doi:10.1175/1520-0469(2003)60<1041:AOHHAT>2.0.CO;2.
- MALKUS, J. S., 1952: The slopes of cumulus clouds in relation to external wind shear. *Quart. J. Roy. Meteor. Soc.*, **78** (338), pp. 530–542, doi:10.1002/qj.49707833804.
- MALKUS, J. S. AND R. S. SCORER, 1955: The erosion of cumulus towers. *J. Atmos. Sci.*, **12** (1), pp. 43–57, doi:10.1175/1520-0469(1955)012<0000:TEOCT>2.0.CO;2.

- MALKUS, J. S., R. S. SCORER, F. H. LUDLAM, AND O. BJRGUM, 1953: Bubble theory of penetrative convection. *Quart. J. Roy. Meteor. Soc.*, **79** (340), pp. 288–293, doi:10.1002/qj.49707934011.
- NEGGERS, R. A. J., P. G. DUYNKERKE, AND S. M. A. RODTS, 2003a: Shallow cumulus convection: A validation of large-eddy simulation against aircraft and Landsat observations. *Quart. J. Roy. Meteor. Soc.*, **129** (593), pp. 2671–2696, doi:10.1256/qj.02.93.
- NEGGERS, R. A. J., H. J. J. JONKER, AND A. P. SIEBESMA, 2003b: Size statistics of cumulus cloud populations in large-eddy simulations. *J. Atmos. Sci.*, **60** (8), pp. 1060–1074, doi:10.1175/1520-0469(2003)60<1060:SSOCCP>2.0.CO;2.
- NEGGERS, R. A. J., A. P. SIEBESMA, AND H. J. J. JONKER, 2002: A multiparcel model for shallow cumulus convection. *J. Atmos. Sci.*, **59** (10), pp. 1655–1668, doi:10.1175/1520-0469(2002)059<1655:AMMFSC>2.0.CO;2.
- NIEUWSTADT, F. T. M. AND R. A. BROST, 1986: The decay of convective turbulence. *J. Atmos. Sci.*, **43**, pp. 532–546, doi:10.1175/1520-0469(1986)043<0532:TDOCT>2.0.CO;2.
- PALUCH, I. R., 1979: The entrainment mechanism in Colorado cumuli. *J. Atmos. Sci.*, **36**, p. 2467, doi:10.1175/1520-0469(1979)036<2467:TEMICC>2.0.CO;2.
- PERRY, K. D. AND P. V. HOBBS, 1996: Influences of isolated cumulus clouds on the humidity of their surroundings. *J. Atmos. Sci.*, **53** (1), pp. 159–174, doi:10.1175/1520-0469(1996)053<0159:IOICCO>2.0.CO;2.
- POLS, C. F. J., 2008: Mass-flux distribution of cumulus clouds from aircraft observations. Bachelor's thesis, Delft University of Technology.
- RAUBER, R. M., B. STEVENS, H. T. OCHS, C. A. KNIGHT, B. A. ALBRECHT, A. M. BLYTH, C. W. FAIRALL, J. B. JENSEN, ET AL., 2007a: Rain in (shallow) cumulus over the ocean - The RICO campaign. *Bull. Amer. Meteor. Soc.*, **88** (12), pp. 1912–1928, doi:10.1175/BAMS-88-12-1912.
- RAUBER, R. M., B. STEVENS, H. T. OCHS, C. A. KNIGHT, B. A. ALBRECHT, A. M. BLYTH, C. W. FAIRALL, J. B. JENSEN, ET AL., 2007b: Supplement to: Rain in (shallow) cumulus over the ocean - The RICO campaign. *Bull. Amer. Meteor. Soc.*, **88** (12), pp. S12–S18, doi:10.1175/BAMS-88-12-Rauber.
- RAYMOND, D. J. AND M. H. WILKENING, 1982: Flow and mixing in New-Mexico mountain cumuli. *J. Atmos. Sci.*, **39** (10), pp. 2211–2228, doi:10.1175/1520-0469(1982)039<2211:FAMINM>2.0.CO;2.
- REINTJES, B., 2005: Shallow cumulus clouds: A parameter study of the development and stability of cumulus clouds in the Atmospheric Boundary Layer. Bachelor's thesis, Delft University of Technology.

- REUTER, G. W. AND M. K. YAU, 1987a: Mixing mechanisms in cumulus congestus clouds .1. Observations. *J. Atmos. Sci.*, **44** (5), pp. 781–797, doi:10.1175/1520-0469(1987)044<0781:MMICCC>2.0.CO;2.
- REUTER, G. W. AND M. K. YAU, 1987b: Mixing mechanisms in cumulus congestus clouds .2. Numerical simulations. *J. Atmos. Sci.*, **44** (5), pp. 798–827, doi:10.1175/1520-0469(1987)044<0798:MMICCC>2.0.CO;2.
- RODTS, S. M. A., P. G. DUYNKERKE, AND H. J. J. JONKER, 2003: Size distributions and dynamical properties of shallow cumulus clouds from aircraft observations and satellite data. *J. Atmos. Sci.*, **60** (16), pp. 1895–1912, doi:10.1175/1520-0469(2003)060<1895:SDADPO>2.0.CO;2.
- VON SALZEN, K. AND N. A. MCFARLANE, 2002: Parameterization of the bulk effects of lateral and cloud-top entrainment in transient shallow cumulus clouds. *J. Atmos. Sci.*, **59**, pp. 1405–1430, doi:10.1175/1520-0469(2002)059<1405:POTBEO>2.0.CO;2.
- SANDERS, M. B., 2007: A three-layer model to study the descending shell around shallow cumulus clouds. Bachelor's thesis, Delft University of Technology.
- SCORER, R. S. AND F. H. LUDLAM, 1953: Bubble theory of penetrative convection. *Quart. J. Roy. Meteor. Soc.*, **79** (339), pp. 94–103, doi:10.1002/qj.49707933908.
- SIEBERT, H., K. LEHMANN, M. WENDISCH, AND R. SHAW, 2006: Small-scale turbulence in clouds. 12th Conference on Cloud Physics, 10 - 14 July, Madison, WI, USA.
- SIEBESMA, A. P., C. S. BRETHERTON, A. BROWN, A. CHLOND, J. CUXART, P. G. DUYNKERKE, H. L. JIANG, M. KHAIROUTDINOV, ET AL., 2003: A large eddy simulation intercomparison study of shallow cumulus convection. *J. Atmos. Sci.*, **60** (10), pp. 1201–1219, doi:10.1175/1520-0469(2003)60<1201:ALESIS>2.0.CO;2.
- SIEBESMA, A. P. AND J. W. M. CUIJPERS, 1995: Evaluation of parametric assumptions for shallow cumulus convection. *J. Atmos. Sci.*, **52** (6), pp. 650–666, doi:10.1175/1520-0469(1995)052<0650:EOPAFS>2.0.CO;2.
- SIEBESMA, A. P. AND A. A. M. HOLTSLAG, 1996: Model impacts of entrainment and detrainment rates in shallow cumulus convection. *J. Atmos. Sci.*, **53**, pp. 2354–2364, doi:10.1175/1520-0469(1996)053<2354:MIOEAD>2.0.CO;2.
- SIEBESMA, A. P. AND H. J. J. JONKER, 2000: Anomalous scaling of cumulus cloud boundaries. *Phys. Rev. Lett.*, **85**, pp. 214–217, doi:10.1103/PhysRevLett.85.214.
- SOMMERIA, G., 1976: Three-dimensional simulation of turbulent processes in an undisturbed trade-wind boundary layer. *J. Atmos. Sci.*, **33**, pp. 216–241, doi:10.1175/1520-0469(1976)033<0216:TDSOTP>2.0.CO;2.
- SOMMERIA, G. AND J. W. DEARDORFF, 1977: Subgrid-scale condensation in models of non-precipitating clouds. *J. Atmos. Sci.*, **34**, pp. 344–355, doi:10.1175/1520-0469(1977)034<0344:SSCIMO>2.0.CO;2.

- SQUIRES, P., 1958a: Penetrative downdraughts in cumuli. *Tellus*, **10**, pp. 381–389.
- SQUIRES, P., 1958b: The microstructure and colloidal stability of warm clouds 1. The relation between structure and stability. *Tellus*, **10** (2), pp. 256–261.
- SQUIRES, P., 1958c: The microstructure and colloidal stability of warm clouds 2. The causes of the variations in microstructure. *Tellus*, **10** (2), pp. 262–271.
- STEVENS, B., A. S. ACKERMAN, B. A. ALBRECHT, A. R. BROWN, A. CHLOND, J. CUXART, P. G. DUYNKERKE, D. C. LEWELLEN, ET AL., 2001: Simulations of trade wind cumuli under a strong inversion. *J. Atmos. Sci.*, **58** (14), pp. 1870–1891, doi:10.1175/1520-0469(2001)058<1870:SOTWCU>2.0.CO;2.
- STOMMEL, H., 1947: Entrainment of air into a cumulus cloud. *J. Meteor.*, **4**, pp. 91–94, doi:10.1175/1520-0469(1947)004<0091:EOAIAC>2.0.CO;2.
- TAYLOR, G. R. AND M. B. BAKER, 1991: Entrainment and Detrainment In Cumulus Clouds. *J. Atmos. Sci.*, **48** (1), pp. 112–121, doi:10.1175/1520-0469(1991)048<0112:EADICC>2.0.CO;2.
- TAYLOR, R. M., II, T. C. HUDSON, A. SEEGER, H. WEBER, J. JULIANO, AND A. T. HELSER, 2001: VRPN: a device-independent, network-transparent VR peripheral system. Proceedings of the ACM Symposium on Virtual Reality Software & Technology 2001.
- TELFORD, J. W. AND P. B. WAGNER, 1974: Measurement of horizontal air motion near clouds from aircraft. *J. Atmos. Sci.*, **31** (8), pp. 2066–2080, doi:10.1175/1520-0469(1974)031<2066:TMOHAM>2.0.CO;2.
- TELFORD, J. W. AND P. B. WAGNER, 1980: The dynamical and liquid water structure of the small cumulus as determined from its environment. *Pure Appl. Geophys.*, **118**, pp. 935–952, doi:10.1007/BF01593041.
- THOMSON, D. J., 1987: Criteria for the selection of stochastic models of particle trajectories in turbulent flows. *J. Fluid Mech.*, **180**, pp. 529–556, doi:10.1017/S0022112087001940.
- TIEDTKE, M., 1989: A comprehensive mass flux scheme for cumulus parameterization in large-scale models. *Mon. Wea. Rev.*, **117**, pp. 1779–1800, doi:10.1175/1520-0493(1989)117<1779:ACMFSF>2.0.CO;2.
- VERZIJLBERGH, R. A., 2006: Shallow Cumulus Clouds: A study of relations between sub-cloud length scales, cloud size distributions and entrainment profiles. Bachelor's thesis, Delft University of Technology.
- VERZIJLBERGH, R. A., 2008: Turbulent dispersion in cloudy boundary layers. Master's thesis, Delft University of Technology.

- VERZIJBBERGH, R. A., T. HEUS, AND H. J. J. JONKER, 2008a: Turbulent dispersion in cloudy boundary layers. The 18th conference on Boundary-Layers and Turbulence.
- VERZIJBBERGH, R. A., T. HEUS, H. J. J. JONKER, AND J. VILÀ-GUERAU DE ARELLANO, 2008b: Turbulent dispersion in cloudy boundary layers. *Atmospheric Chemistry And Physics*, submitted.
- WARNER, J. AND P. SQUIRES, 1958: Liquid water content and the adiabatic model of cumulus development. *Tellus*, **10** (3), pp. 390–394.
- WEIL, J. C., P. P. SULLIVAN, AND C. H. MOENG, 2004: The use of large-eddy simulations in Lagrangian particle dispersion models. *J. Atmos. Sci.*, **61** (23), pp. 2877–2887, doi:10.1175/JAS-3302.1.
- WICKER, L. J. AND W. C. SKAMAROCK, 2002: Time-splitting methods for elastic models using forward time schemes. *Mon. Wea. Rev.*, **130**, pp. 2088–2097, doi:10.1175/1520-0493(2002)130<2088:TSMFEM>2.0.CO;2.
- WOITTEZ, E. J. P., H. J. J. JONKER, AND L. M. PORTELA, 2008: On the combined effects of turbulence and gravity on droplet collision in convective clouds: a numerical study, submitted.
- VAN ZANTEN, M. C., 2000: Entrainment processes in stratocumulus. Ph.D. thesis, Institute for marine and atmospheric research Utrecht, Utrecht University, ISBN:90-393-2353-4.
- VAN ZANTEN, M. C. ET AL., 2008: RICO intercomparison, in preparation.
- ZHAO, M. AND P. H. AUSTIN, 2005a: Life cycle of numerically simulated shallow cumulus clouds. Part I: Transport. *J. Atmos. Sci.*, **62**, pp. 1269–1290, doi:10.1175/JAS3414.1.
- ZHAO, M. AND P. H. AUSTIN, 2005b: Life cycle of numerically simulated shallow cumulus clouds. Part II: Mixing dynamics. *J. Atmos. Sci.*, **62**, pp. 1291–1310, doi:10.1175/JAS3415.1.

ACKNOWLEDGMENTS

I know
You might roll your eyes at this
But I'm so
Glad that you exist

THE WEAKERTHANS

And so, this thesis has nearly come to an end, although from my own experience I know that for many of the readers this is one of the very first pages to read, right after the propositions and perhaps the first paragraphs of the summary and the introduction. For those people is the first thank you of this chapter: Thank you for your brave attempt of reading this!

Having said that, it's my pleasure to thank the people who have been most intimately involved in the $14+144=158$ pages you're currently enjoying, and it is definitely my pleasure to start with my promotor, Harry van den Akker. The synergy of industrial and environmental processes that formed the setting of our discussions nearly always ensured a change of perspective which made the end result of our work much more solid and accessible. The overview he had over the project has probably been one of the major reasons why I could finish within a reasonable time limit.

In popular descriptions of the history of the Universe, solar system or the earth, an analogy is often staged where the complete history is condensed to twenty four hours. First it takes hours for stars to form, for our planet to emerge from dust and to cool down a bit, for life to start from the primordial soup (I believe it's already ten or eleven PM by then) for the dinosaurs to come and go until, finally, homo sapiens is arriving in the last couple of minutes of our fictional day. From there, everything suddenly goes really fast, or rather becomes rapidly very personal for us.

If I want to give credit here in measures that does any justice to the way people have been involved in this thesis, I'd be faced with a rather similar problem. From the Big Bang until the Olduvai Gorge, I would have to keep on talking about how Harm Jonker taught me everything I know of science, atmospheric, clouds, discussing (well, at least scientific discussion), writing, presenting, whatever, shrewdly observing the supervision any of his students might need, all to the point where it seems almost irrelevant that he is also a nice guy, which, by the way, it is not. Since a transcript of such a monologue would raise the printing fees of this thesis to absurd levels, I'll just leave it with a heartfelt thank you for lighting the accursed flame of science in me. I feel extremely lucky to have responded as impulsively to an e-mail somewhere in June 2002 in application for a Master's graduation project,

and I feel extremely happy to see the atmospheric sciences blossom so much within Multi-Scale Physics at his hands six years later.

Did I say that Harm taught me scientific discussion? Well, there's at least one person who might have something to say about that. Maarten van Reeuwijks constant stream of questions, explanations and whiteboard sessions for sure kickstarted my PhD, and I immensely enjoyed our endless discussions - as I am sure the rest of the corridor did sometimes. And then there was his annoyingly cool taste in music. Would you believe that I actually sometimes got a bit (just a bit, mind) bored of always having to listen to my own music since he left our department?

Now, let's turn to the other people with whom I've discussed most, whose work is reflected at several points in this thesis: My BSc and MSc graduation students. Bas Reintjes came first, and although his parameter study did not leave much direct fingerprint here, I learned a lot from the way clouds set their own cloud layer, and I enjoyed his enterprising and independent mind. Then we had Gertjan van Dijk, whose hard and loyal work on the implementation of the LPDM led to chapter 5 of this thesis and an article described by the editor as "exactly the type of paper we look for in the Journal of the Atmospheric Sciences". Remco Verzijlbergh started with his Bachelor's project on subcloud-layer length scales and their relations to clouds and entrainment. He grew up to become an extremely eager and interested Master's student who is a joy to discuss with (and makes it impossible *not* to discuss with). His work on dispersion combines the subsiding shell and the Lagrangian particles. Great stuff. Freek Pols is in a sense the odd one out, since his Bachelor's work has been on the real world, instead of our computerized simplicity called LES. He makes the processing of observations look so easy that sometimes I'm tempted to do it myself. It was a pleasure to see a growing understanding of the atmospheric boundary layer in all of them, considering that they had to learn it in an extremely condensed course.

My colleagues at EWI Eric Griffith and Dylan Dussel, Frits Post and Michal Koutek were essential for some parts of our work, even when I acted reluctantly and conservatively. The proudest moments of chapter 6 could not have been done without their virtual reality workbench, the CloudExplorer or the hypercool and insightful Lagrangian particle visualizations. Equally unmissable were the supercomputers at SARA, accompanied by funding from NCF/NWO and -at least as important- accompanied by an excellent helpdesk. They may have only heard from me if Teras/Aster/Huygens happened to be a bit slow, or when they had to solve my mistakes, but I deeply respect the hard work of keeping the clusters up-and-running, and keeping the over-demanding users happy.

In this time of paper-driven research, a PhD thesis may feel more and more like an anachronism, but nevertheless the theses of Hans Cuijpers, Margreet van Zanten, Roel Neggers and Alessandro Dosio, and specifically the parts on the details and quirks of DALES, were often found open on my desk.

For the rest, I immensely enjoyed the rewarding discussion with, amongst many others, Pier Siebesma, Stephan de Roode, Evgeni Fedorovich, Bjorn Stevens, Don Lenschow, Jordi Vilà-Guerau de Arellano, Chiel van Heerwaarden, and Gert-Jan

Steenefeld. To all the others of MSP: Cheers. To the Virtual Dutch Department of Boundary Layer Meteorology, consisting of people from KNMI, Wageningen, Utrecht and Delft: I rank our biannual "BBOS" meetings as extremely fruitful and fun. And I should not forget to thank Frans van Duijnen and his skills in Adobe Photoshop, since without him the cover of this thesis would have been far less beautiful than it is right now.

As for everybody else, the enjoyable many and the precious few who attempt to pull me into the broad daylight outside of academia: I hope you know how much you're loved. If not (and I've been neglecting too many of you lately), I should express it in better deeds, since no mere thesis chapter could convey it anyway.

Thank you.

ABOUT THE AUTHOR

It's all about passion
It's all about perception
Don't call me on my cell phone
'Cause there ain't no reception
When I'm gone
I made friends with the clouds
I made friends with the birds
If you ask a goose a question
He never shuts up.

CLOUD CULT

I was born on August 22nd, 1979 in the center of Utrecht, about 200 meter (as the boy bikes) from my secondary-school-to-be (Christelijk Gymnasium), and about 500 meter (as the cloud drifts) from the original home of the Royal Netherlands Meteorological Institute, the majestic Sonnenborgh Observatory. During a fine youth dominated by the river I was born next to, I commenced my education at August 22nd, 1983 at the Aeneas Mackaay primary school, finished primary education at the Jenaplan School Cleophas before secondary school graduation in June 1997.

The yearning to ask “why?” and to extensively discuss all the possible answers may have distressed my teachers early on, but it was actually nurtured by extracurricular activities at the Cleophas, and further stimulated by my math teacher at the Christelijk Gymnasium. This background made physics an almost inevitable choice of study. I started to study experimental physics at the Utrecht University that August, combining it with meteorology and physical oceanography along the way. After a few years sprinkled with activities in the student swimming and cycling communities, as well as the departmental student board, in the summer of 2002 it was finally time to start a Master's graduation project, supervised by Han van Dop from the Institute of Marine and Atmospheric Research Utrecht. For a good representation of the experimental physics as well as of the meteorology in my project, I went to the department of Multi-Scale Physics of the Delft University of Technology to work with Harm Jonker on a water-tank Laboratory Experiment on the Atmospheric Boundary Layer. I finished in January 2004.

Having stumbled over the stimulating scientific atmosphere in Delft, I was pleased to switch from laboratory to numerics and to do a PhD project with Harm again as supervisor, and Harrie van den Akker as promotor. The work I conducted between April 2004 and May 2008 has been presented in various national and international conferences, and was granted the award for best student presentation at the 17th AMS Symposium on Boundary Layers and Turbulence in San Diego, USA. This thesis is the final result of the PhD project, and will be defended at December 9,

2008, in conclusion of my first quarter century of education.

After finishing this thesis, I revisited my roots to work at the Royal Netherlands Meteorological Institute (KNMI) in June 2008 for post-doctoral research, in an attempt to tie LES more directly to Cabauw measurements.

JOURNAL PUBLICATIONS

6. VERZIJLBERGH, R. A., T. HEUS, H. J. J. JONKER, AND J. VILÀ-GUERAU DE ARELLANO, 2008b: Turbulent dispersion in cloudy boundary layers. *Atmospheric Chemistry And Physics*, submitted
5. HEUS, T., H. J. J. JONKER, H. E. A. VAN DEN AKKER, E. J. GRIFFITH, M. KOUTEK, AND F. H. POST, 2008b: A statistical approach to the life-cycle analysis of cumulus clouds selected in a Virtual Reality Environment. *J. Geophys. Res.*, submitted
4. HEUS, T., C. F. J. POLS, H. J. J. JONKER, H. E. A. VAN DEN AKKER, AND D. H. LENSCHOW, 2008d: Observational validation of the compensating mass ux through the shell around cumulus clouds. *Quart. J. Roy. Meteor. Soc.*, doi:10.1256/qj.08.66, accepted pending minor revisions
3. HEUS, T., G. VAN DIJK, H. J. J. JONKER, AND H. E. A. VAN DEN AKKER, 2008a: Mixing in shallow cumulus clouds studied by Lagrangian particle tracking. *J. Atmos. Sci.*, **65** (8), pp. 2581–2597, doi:10.1175/2008JAS2572.1
2. JONKER, H. J. J., T. HEUS, AND P. P. SULLIVAN, 2008: A refined view of vertical transport by cumulus convection. *Geophys. Res. Lett.*, **35**, p. L07810, doi:10.1029/2007GL032606
1. HEUS, T. AND H. J. J. JONKER, 2008b: Subsiding shells around shallow cumulus clouds. *J. Atmos. Sci.*, **65** (3), pp. 1003–1018, doi:10.1175/2007JAS2322.1

CONFERENCE PROCEEDINGS

8. HEUS, T., H. J. J. JONKER, H. E. A. VAN DEN AKKER, E. J. GRIFFITH, M. KOUTEK, AND F. H. POST, 2008c: A statistical approach to the life-cycle analysis of cumulus clouds selected in a Virtual Reality Environment. The 18th conference on Boundary-Layers and Turbulence
7. HEUS, T., C. F. J. POLS, H. J. J. JONKER, H. E. A. v. D. AKKER, AND D. H. LENSCHOW, 2008e: Observational validation of the compensating mass ux through the shell around cumulus clouds. The 18th conference on Boundary-Layers and Turbulence

-
6. VERZIJLBERGH, R. A., T. HEUS, AND H. J. J. JONKER, 2008a: Turbulent dispersion in cloudy boundary layers. The 18th conference on Boundary-Layers and Turbulence
 5. HEUS, T., H. J. J. JONKER, E. J. GRIFFITH, AND F. H. POST, 2006: Lifecycle analysis of cumulus clouds using a 3d virtual reality environment. The 17th conference on Boundary-Layers and Turbulence
 4. HEUS, T. AND H. J. J. JONKER, 2006: Why do descending shells around cumulus clouds exist? The 17th Symposium on Boundary-Layers and Turbulence
 3. JONKER, H., R. VERZIJLBERGH, T. HEUS, AND A. SIEBESMA, 2006: The influence of the sub-cloud moisture field on cloud size distributions and the consequences for entrainment. The 17th Symposium on Boundary-Layers and Turbulence
 2. GRIFFITH, E. J., F. H. POST, M. KOUTEK, T. HEUS, AND H. J. J. JONKER, 2005: Feature tracking in VR for cumulus cloud life-cycle studies. E. Kjems and R. Blach, (eds.) *Virtual Environments 2005*, pp. 121–128
 1. JONKER, H., T. HEUS, E. HAGEN, AND H. VAN DOP, 2004: Laboratory experiments of entrainment in dry convective boundary layers. The 16th Symposium on Boundary-Layers and Turbulence

SUPERVISED STUDENTS

5. VERZIJLBERGH, R. A., 2008: Turbulent dispersion in cloudy boundary layers. Master's thesis, Delft University of Technology
4. POLS, C. F. J., 2008: Mass-flux distribution of cumulus clouds from aircraft observations. Bachelor's thesis, Delft University of Technology
3. VAN DIJK, G., 2007: The implementation of a Lagrangian particle dispersion model in large eddy simulations of the atmospheric boundary layer. Master's thesis, Delft University of Technology
2. VERZIJLBERGH, R. A., 2006: Shallow Cumulus Clouds: A study of relations between sub-cloud length scales, cloud size distributions and entrainment profiles. Bachelor's thesis, Delft University of Technology
1. REINTJES, B., 2005: Shallow cumulus clouds: A parameter study of the development and stability of cumulus clouds in the Atmospheric Boundary Layer. Bachelor's thesis, Delft University of Technology

INVITED LECTURES

2. HEUS, T., 2008: On the edge of a cloud. Lecture at CNRM, MétéoFrance, Toulouse, France
1. HEUS, T. AND H. J. J. JONKER, 2008a: The day after tomorrow – Could this happen to us? Lecture at the Openbare Scholengemeenschap Lek en Linge, Culemborg, The Netherlands

On the edge of a cloud

Cumulus clouds have since long been one of the greatest challenges in the atmospheric sciences. For a correct representation of clouds in weather and climate models, where they are the largest unknowns, a good understanding of interaction between cloud and environment is of prime importance. In this thesis, this problem is attacked with a combination of detailed numerical simulations and air-plane observations.

While the traditional view states that air inside the cloud goes up, and all the air outside goes down in compensation, it is found here that on average, the air far away from the cloud hardly moves. Most of the compensating downward motion happens in the direct vicinity of the cloud, in a subsiding shell. This shell is shown to be due to cloudy air that evaporates, cools, and therefore sinks. Interaction between cloud and environment only happens through the buffer layer created by the shell. The shell is especially strong due to the horizontal mixing that is dominant in the cloud-environment interaction: processes that happen at the top of the cloud have little or no influence at lower levels. As a function of time, the cloud is not behaving like a continuously upward moving thermal, but consists of several bubble-like pulses. Again, horizontal mixing is important in understanding the physics of these pulses.